The Thesis Committee for Xiangming Yu
certifies that this is the approved version of the following thesis:

Three Dimensional Viscous/Inviscid Interactive Method and Its Application to Propeller Blades

Committee:

_____

Spyros A. Kinnas, Supervisor

_____

Howard Liljestrand

Three Dimensional Viscous/Inviscid Interactive Method and Its Application to Propeller Blades

by

Xiangming Yu, B.E.

THESIS

Presented to the Faculty of the Graduate School of

The University of Texas at Austin

in Partial Fulfillment

of the Requirements

for the Degree of

MASTER OF SCIENCE in ENGINEERING

THE UNIVERSITY OF TEXAS AT AUSTIN

August 2012

Dedicated to my family and friends.

Acknowledgments

I first wish to thank my supervisor, Prof. Kinnas, for his continued guidance and assistance over the last two years. His extraordinary wisdom and unlimited passion for research inspires me to pursue my own academic career. His encouragements and suggestions lead me forward, and help me overcome difficulties in both my research and life. I do and will benefit from him all my life. Also I want to thank Prof. Liljestrand for his reviewing of my thesis.

Then I would like to thank all my friends in the Computational Hydrodynamics Laboratory (CHL) for their selfless help and companionship. I would especially thank Mr. Ye Tian, Shu-Hao Chang, Liwei Han and Dr. Lei He for their significant help not only in my research, but also in many aspects of my life.

I would also thank my friends at Austin: Mr. Wentao Fu, Xudong Xu, Haizhao Yang, Shichao Dai and Miss Xiaoqian Li. My life at Austin becomes more colorful and memorable because of their companionship.

Finally, I want to express my sincere appreciation to my parents, Xiaosheng Yu and Guixia Liu. Without their love and encouragement, I would never finish this work.

Three Dimensional Viscous/Inviscid Interactive Method and Its Application to Propeller Blades

Xiangming Yu, M.S.E.
The University of Texas at Austin, 2012

Supervisor: Spyros A. Kinnas

A three dimensional viscous/inviscid interactive boundary layer method for predicting the effects of fluid viscosity on the performance of fully wetted propellers is presented. This method is developed by coupling a three dimensional low-order potential based panel method and a two dimensional integral boundary layer analysis method. To simplify the solution procedures, this method applies a reasonable assumption that the effects of the boundary layer along the span wise direction (radially outward for propeller blades) could be negligible compared with those along the stream wise direction (constant radius for propeller blades). One significant development of this method, compared with previous work, is to completely consider the effects of the added sources on the whole blades and wakes rather than evaluate the boundary layer effects along each strip, without interaction among strips. This method is applied to Propeller DTMB 4119, Propeller NSRDC 4381 and DTMB Duct II

for validation. The results show good correlation with experimental measurements or RANS (ANSYS/FLUENT) results. The method is further used to develop a viscous image model for the cases of three dimensional wing blades between two parallel slip walls.

An improved method for hydrofoils and propeller blades with non-zero thickness or open trailing edges is presented as well. The method in this thesis follows the idea of Pan (2009, 2011), but applies a new extension scheme, which uses second order polynomials to describe the extension edges. A improved simplified search scheme is also used to find the correct shape of the extension automatically to ensure the two conditions are satisfied.

Table of Contents

List of Tables

List of Figures

xvi

Nomenclature

Latin Symbols

C_τ	shear stress coefficient $C_\tau = \tau_{max}/(\rho U^2)$
C_f	skin-friction coefficient $C_f = \tau_{wall}/(0.5\rho U^2)$
C_p	pressure coefficient, $C_p = (P - P_o)/(0.5\rho n^2 D^2)$
D	propeller diameter, $D = 2R$
$\mathcal{D}$	dissipation or shear work integral, $\mathcal{D} = \int_0^\delta \left(\tau_1 \frac{\partial u}{\partial x_3} + \tau_2 \frac{\partial w}{\partial x_3} \right) dx_3$
f_{max}/C	maximum camber to chord ratio
G	Green's function
H	shape factor, $H = \delta^*/\theta$
H^*	kinetic energy shape factor, θ^*/θ
J	advance ratio based on V_s, $J = V_s/(nD)$
K_Q	torque coefficient, $K_Q = Q/(\rho n^2 D^5)$
K_T	thrust coefficient, $K_T = T/(\rho n^2 D^4)$

$\boldsymbol{q}$ total velocity

Q torque

$\boldsymbol{U}_{in}$ local inflow velocity (in the propeller fixed system)

$\boldsymbol{u}$ Perturbation velocity

q_e Magnitude of edge velocity

R propeller radius

Re Reynolds number

S_P blade surface

S_W wake surface

K thrust

t_{max}/C maximum thickness to chord ratio

u_e boundary layer edge velocity

u_τ wall shear velocity, $u_\tau = \sqrt{\tau_{wall}/\rho}$

x, y, z propeller fixed coordinates

y^+ non-dimensional wall distance, $y^+ = \frac{u_\tau y}{\nu}$

Greek Symbols

α angle of attack

δ^* displacement thickness, $\delta^* = \int (1 - \frac{u}{U_e}) dz$

Δt time step size

ω propeller angular velocity

ν kinematic viscosity of water

ϕ perturbation potential

Φ total potential

ρ fluid density

θ momentum thickness, $\theta = \int \frac{u}{U_e}(1 - \frac{u}{U_e}) dz$

θ^* kinetic energy thickness, $\theta^* = \int \frac{u}{U_e}(1 - \frac{u^2}{U_e^2}) dz$

Uppercase Abbreviations

2D   two dimensional

3D   three dimensional

CPU   central processing unit

MIT   Massachusetts Institute of Technology

NACA   National Advisory Committee for Aeronautics

RANS   Reynolds-averaged Navier Stokes

Computer Program Names

CAV2DBL   cavitating 2-dimensional with boundary layer

Fluent   A commercial RANS solver

PROPCAV   cavitating propeller potential flow solver based on BEM

XFOIL   2D integral boundary layer analysis code

Chapter 1

Introduction

1.1   Background

Panel methods have been extensively used in the design stage of ma-
rine propellers due to the satisfactory prediction of propeller performance with
small computational cost. However, since they are based on the inviscid po-
tential flow theory, classical panel methods cannot predict the effects of fluid
viscosity. For propeller flows, viscosity can not only cause friction but also af-
fect the pressure on propeller blades, resulting in the changes of thrust/torque
forces and propeller efficiency. Some empirical methods can be used with pan-
el methods to take account of the effects of fluid viscosity. Kerwin and Lee
(1978) used an adopted constant as the skin friction coefficient to include the
contribution of the viscous shear stress and an empirical viscous pitch cor-
rection to approximate the influences of the boundary layer. However, such
empirical methods require user adjustable constants, which could be good for
some cases, but inaccurate for some other cases. In order to handle the effect-
s of viscosity for general blade geometries and various flow conditions, more
rational methods are required.

Viscous/inviscid interactive methods in 2D have been highly developed

in the past decades, from which the fully simultaneous coupling scheme developed by Drela (1985, 1987) has been proved to be the most robust and efficient one for 2-D separated flows. Drela (1989) implemented a viscous/inviscid interactive solver, XFOIL, for 2D airfoils. XFOIL uses the stream function to get the inviscid flow field. Then the inviscid solution is coupled with the 2D integral boundary layer equations to solve for the boundary layer variables. The development of the viscous/inviscid interactive methods in 3D is limited because of the complexity of 3D boundary layer. Cousteix and Houdeville (1981) pointed out that the 3D integral boundary layer equations consist of three fully hyperbolic non-linear partial differential equations. Milewski (1997) developed a 3D fully simultaneous viscous/inviscid interactive scheme, by coupling a potential based panel method and the 3D integral boundary layer equations, for 3D wetted hydrofoil and duct flows. However, such a scheme requires a large amount of computer resources and is very difficult to be applied to complicated geometries such as propeller blades. For 3D propeller cases particularly, Jessup (1989) measured the boundary layer variables on the blades of Propeller DTMB 4119 and found that the boundary layer variables on the stream wise direction are much more significant than those on the span wise direction. According to Jessup's measurements, Hufford (1992, 1994) assumed that the effects of the boundary layer on propeller blades should be negligible radially outward compared with those along constant radius. Based on the above assumption, he proposed a method used to predict the 3D boundary layer effects on propeller blades. His method calculates the inviscid solution

2

by a potential based panel method and then applies a 2D viscous/inviscid interactive method to each strip along constant radius of the blades using, however, 3D boundary layer sources over each strip. Sun (2008) coupled a potential based panel method code, PROPCAV, with XFOIL following Hufford's method, but further simplified the method by adding 2D boundary layer sources over the strips. However, Hufford and Sun considered the boundary layer on each strip independently and ignored the boundary layer effects of neighboring strips and other blades, which oversimplified the problem.

1.2   Objective

The main objective of this thesis is to develop a more reasonable and complete 3D viscous/inviscid interactive method by coupling a 3D low-order potential based panel method code, PROPCAV, with Drela's 2D integral boundary layer solver, XFOIL, to investigate the effects of fluid viscosity on the performance of propellers.

1.3   Organization

This thesis is organized into six chapters.

Chapter 1 contains the literature review, the objective and the organization of this study.

Chapter 2 introduces a two-dimensional viscous/inviscid interactive method in details. This method is applied to a 2D hydrofoil case, and the

results are correlated with RANS (ANSYS/FLUENT) results.

Chapter 3 develops a three dimensional viscous/inviscid interactive method for propeller and duct flows. The method follows the assumption of Hufford (1992, 1994) and Sun (2008) that the boundary layer along the span wise direction (radially outward for propeller blades) can be negligible, but further considers the boundary layer effects from neighboring strips and blades. Then this method is validated through two propeller and a bare duct cases.

Chapter 4 extends the three dimensional viscous/inviscid interactive method to an image model used to consider the effects of slip walls. Cases of a straight and a swept wing blade between two parallel walls are carried out to validate the image model.

Chapter 5 improves the scheme proposed by Pan (2009, 2011) for hydrofoils and propeller blades with non-zero thickness trailing edges. The results of sample cases are presented.

Chapter 6 summarizes the work of this thesis and presents the recommendations for future research.

Chapter 2

Two Dimensional Viscous/Inviscid Interactive Method

In this chapter, a 2D viscous/inviscid interactive method is introduced. This method couples a 2D low-order potential based panel method and the 2D integral boundary layer analysis. The chapter starts with the introduction of the 2D wall transpiration model and then derives the expression of the viscous or edge velocity. In the following, the 2D integral boundary layer equations are summarized. The coupling algorithm between the invsicid and viscous solution is presented next. Finally, this method is applied to a 2D hydrofoil case. The results are compared with those predicted by RANS (ANSYS/FLUENT).

2.1 Governing Equations

A lower-order panel method, in which constant sources and dipoles are used, based on perturbation potential is applied in this thesis. The total velocity is decomposed into two components: the inflow velocity and the perturbation velocity.

$$q = U_{in} + u \tag{2.1}$$

where $\boldsymbol{q}$ is the total velocity, $\boldsymbol{U_{in}}$ is the velocity of incoming flow, and $\boldsymbol{u}$ is the perturbation velocity.

$$\boldsymbol{u} = \nabla\phi \tag{2.2}$$

$$\boldsymbol{q} = \nabla\Phi_{total} \tag{2.3}$$

The perturbation potential ϕ satisfies the Laplace Equation:

$$\nabla^2\phi = 0 \tag{2.4}$$

The Laplace Equation can be integrated on the boundaries:

$$\begin{aligned}
\frac{\phi_p}{2} &= \iint_{S_p} \left[-\phi_{p'}\frac{\partial G(p,p')}{\partial \boldsymbol{n}_{p'}} + \frac{\partial \phi_{p'}}{\partial \boldsymbol{n}_{p'}}G(p,p') \right] dS \\
&\quad - \iint_{S_W} \Delta\phi_w(p')\frac{\partial G(p,p')}{\partial \boldsymbol{n}_{p'}} dS
\end{aligned} \tag{2.5}$$

where p and p' correspond to the field point and the variable point; $G(p,p') = -\frac{1}{4\pi r}$ for three dimension or $G(p,p') = \frac{\ln(r)}{2\pi}$ for two dimension, is the Green's function with r being the distance between the field point p and the variable point p'; $\Delta\phi_w$ is the potential jump across the wake; S_P and S_W represent the blade surface and wake sheet, respectively.

2.2 Boundary Conditions

In order to obtain an unique solution of (2.5), appropriate boundary conditions are applied to the flow domain. For fully wetted cases, the kinematic boundary condition states:

$$\frac{\partial \phi}{\partial n} = -\boldsymbol{U}_{in} \cdot \boldsymbol{n} \tag{2.6}$$

6

where $\boldsymbol{n}$ is the normal vector on the blade surface pointing into the flow field. At the trailing edge of the blade, Kutta condition is applied, which implies the finite velocity at the blade trailing edge.

$$\nabla \phi = finite \tag{2.7}$$

At the far field, the perturbation velocity vanishes.

$$\nabla \phi = 0 \tag{2.8}$$

2.3   2D Wall Transpiration Model

A 2D wall transpiration model is introduced in this section to simulate the 2D viscous boundary layer. This model couples the potential and the 2D integral boundary layer equations through the edge velocity. The detailed derivation of the expression of the edge or viscous velocity is presented.

2.3.1   Boundary Layer Simulation

For the potential flow, blowing sources are added on the wall to simulate the boundary layer in the real viscous flow (shown in Fig. 2.1). The blowing sources should be given proper strengthes so that the velocity at the edge of boundary layer, $y = y_e$, is the same with that in the real viscous flow. According to the Bernoulli equation, the same edge velocities in the two flows lead to the same pressures on $y = y_e$. In addition, the boundary layer theory tells that the pressure cross the boundary layer stays constant, which means that the pressures on the point A of the edge of boundary layer and point B

7

of the wall are the same. Thus it is concluded that the pressure on the wall in the equivalent inviscid flow is the same with that in the real viscous flow. So far, the effects of the boundary layer on the pressure have been considered in the equivalent inviscid flow by adding proper blowing sources on the wall. In addition, the friction on the wall can be considered by solving the integral boundary layer equations.

(a) Real viscous flow   (b) Equivalent inviscid flow
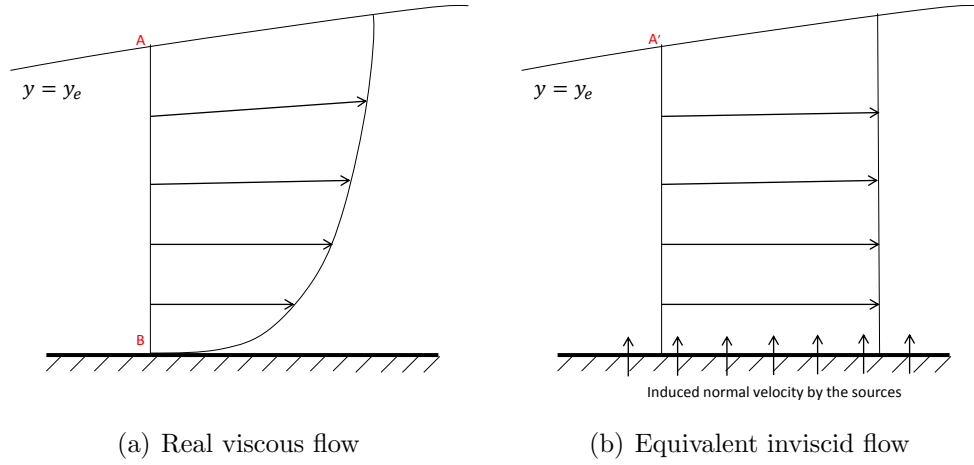
Figure 2.1: Velocity profiles for the real viscous and equivalent inviscid flow

2.3.2 Edge Velocity Expression

The expression of the edge velocity U_e or viscous velocity U_{vis} for 2D hydrofoil cases are derived in this subsection. For 2D hydrofoil cases (shown in Fig. 2.2), (2.5) becomes:

$$\pi\phi_p = \int_{S_p} \left(\frac{\partial \phi}{\partial \boldsymbol{n}} \ln r - \phi \frac{\partial \ln r}{\partial \boldsymbol{n}} \right) ds - \int_{S_W} \left(\Delta\phi_w \frac{\partial \ln r}{\partial \boldsymbol{n}^+} \right) ds \qquad (2.9)$$

8

where ϕ_p is the perturbation potential on the hydrofoil body. The discretized expression of (2.9) is

$$\sum_{j=1}^{N} D_{ij}\phi_j = \sum_{j=1}^{N} S_{ij}\left(\frac{\partial\phi}{\partial n}\right)_j - W_i\Delta\phi_w \qquad (2.10)$$

The Kutta condition can be satisfied using a modified Morino Kutta condition proposed by Kinnas et al. (1990)

$$\Delta\phi = \Phi^N - \Phi^1 + \boldsymbol{U}_{in} \cdot \boldsymbol{r}_t \qquad (2.11)$$

where $\boldsymbol{r}_t$ is the distance between the control points of the upper and lower trailing edge panels (the 1st and the Nth panel). Then (2.10) becomes:

$$\sum_{j=1}^{N} A_{ij}\phi_j = \sum_{j=1}^{N} S_{ij}\left(\frac{\partial\phi}{\partial n}\right)_j - W_i\left(\boldsymbol{U}_{in} \cdot \boldsymbol{r}_t\right) \qquad (2.12)$$

(2.12) can be used to calculate the perturbation potential on the hydrofoil. To consider the effects of fluid viscosity, blowing sources with unknown strength are added on both the body and the wake panels to simulate viscous boundary layer. When the added blowing sources are taken into consideration, (2.12)
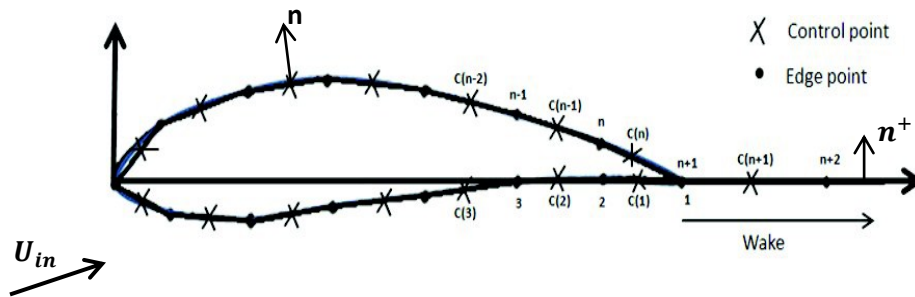
Figure 2.2: The diagram of the paneling on a 2D hydrofoil and its wake

becomes:

$$\sum_{j=1}^{N} A_{ij}\phi_j = \sum_{j=1}^{N} S_{ij}\left(\frac{\partial\phi}{\partial n}\right)_j - W_i\left(\boldsymbol{U}_{in}\cdot\boldsymbol{r}_t\right) + \sum_{j=1}^{N+N_W} B_{ij}\sigma_j \qquad (2.13)$$

where σ_j is the unknown strength of the blowing source added at the panel j; B_{ij} is the source induced influence coefficient analogous to S_{ij}; N and N_W indicate the number of panels on the hydrofoil body and the wake, respectively. Then the perturbation potential on the body panel can be obtained from (2.13):

$$\begin{aligned}
\phi_i &= \sum_{j=1}^{N} A_{ij}^{-1}\left[\sum_{j=1}^{N} S_{jk}\left(\frac{\partial\phi}{\partial n}\right)_k - W_i\left(\boldsymbol{U}_{in}\cdot\boldsymbol{r}_t\right)\right] \\
&\quad + \sum_{j=1}^{N+N_W}\left(\sum_{j=1}^{N} A_{ik}^{-1} B_{kj}\right)\sigma_j
\end{aligned} \qquad (2.14)$$

(2.14) is the expression of the perturbation potential taken the added blowing sources into consideration, or it can be called the viscous perturbation potential. The total potential for viscous cases should be the sum of the viscous perturbation potential and the inflow potential:

$$\begin{aligned}
\Phi_{i,vis} &= \Phi_i^{in} + \phi_{i,vis} \\
&= \Phi_i^{in} + \sum_{j=1}^{N} A_{ij}^{-1}\left[\sum_{j=1}^{N} S_{jk}\left(\frac{\partial\phi}{\partial n}\right)_k - W_i\left(\boldsymbol{U}_{in}\cdot\boldsymbol{r}_{in}\right)\right] + \sum_{j=1}^{N+N_W}\left(\sum_{j=1}^{N} A_{ij}^{-1} B_{kj}\right)\sigma_j \\
&= \Phi_i^{in} + \phi_{i,inv} + \sum_{j=1}^{N+N_W} H_{ij}\sigma_j \\
&= \Phi_{i,inv} + \sum_{j=1}^{N+N_W} H_{ij}\sigma_j
\end{aligned}$$

$$(2.15)$$

where $H_{ij} = \sum_{j=1}^{N} A_{ij}^{-1} B_{kj}$. According to (2.15), the total viscous potential $\Phi_{i,ivs}$ consists of the total inviscid potential $\Phi_{i,inv}$ and the induced potential by the added blowing sources $\sum_{j=1}^{N+N_W} H_{ij}\sigma_j$. The viscous velocity or edge velocity can be obtained by differentiating the total viscous potential along the surface of the hydrofoil:

$$
\begin{aligned}
U_{i,vis} &= \frac{\partial \Phi_{i,ivs}}{\partial s} \\
&= \frac{\partial \Phi_{i,inv}}{\partial s} + \frac{\partial}{\partial s}\left(\sum_{j=1}^{N+N_W} H_{ij}\sigma_j\right) \\
&= U_{i,inv} + \sum_{j=1}^{N+N_W} C_{ij}\sigma_j
\end{aligned}
\tag{2.16}
$$

The viscous velocity on the hydrofoil body can be expressed as (2.16). The derivative of H_{ij} can be achieved by:

$$
C_{ij} = \frac{\partial H_{ij}}{\partial s} = \frac{H_{i,j} - H_{i-1,j}}{\Delta s}
\tag{2.17}
$$

(2.16) states that the viscous velocity $U_{i,vis}$ is the sum of the inviscid velocity $U_{i,inv}$ and the induced velocity by the added blowing sources $\sum_{j=1}^{N+N_W} C_{ij}\sigma_j$. It should be noted that the inflow potential Φ^{in} does not exist in the cases with rotational inflows. Even though the derivation of (2.16) uses the inflow potential Φ^{in}, (2.16) is still general and valid for cases with or without the inflow potential. This is because (2.16) is an expression in terms of velocity instead of potential.

The viscous velocity on the wake sheet can be derived similarly. With the added blowing sources, the perturbation potential (viscous perturbation

11

potential) on the wake can be written as

$$\phi_{wake} = \frac{1}{2\pi} \int_{S_P} \left(\frac{\partial \phi}{\partial \boldsymbol{n}} \ln r - \phi \frac{\partial \ln r}{\partial \boldsymbol{n}} \right) ds + \frac{1}{2\pi} \int_{S_P+S_W} (\ln r) \, \sigma ds \qquad (2.18)$$

Discretizing (2.18) gives:

$$\phi_i^{wake} = \sum_{j=1}^{N} A_{ij}^w \phi_j + \sum_{j=1}^{N} C_{ij}^w \left(\frac{\partial \phi}{\partial n} \right)_j + \sum_{j=1}^{N+N_W} B_{ij}^w \sigma_j \qquad (2.19)$$

where A_{ij}^w, C_{ij}^w and B_{ij}^w are the influence coefficients analogues to those in (2.13) for hydrofoil body. ϕ_j in (2.19) is the viscous perturbation potential on the panel j of the hydrofoil body, which is the sum of the inviscid perturbation potential and the induced potential due to the blowing sources:

$$\phi_j = \phi_{j,inv} + \sum_{j=1}^{N+N_W} H_{jk} \sigma_k \qquad (2.20)$$

Replace ϕ_j in (2.19) with (2.20) and gives:

$$
\begin{aligned}
\phi_i^{wake} &= \sum_{j=1}^{N} A_{ij}^w \left[\phi_j^{inv} + \sum_{j=1}^{N+N_W} H_{jk} \sigma_k \right] + \sum_{j=1}^{N} C_{ij}^w \left(\frac{\partial \phi}{\partial n} \right)_j + \sum_{j=1}^{N+N_W} B_{ij}^w \sigma_j \\
&= \sum_{j=1}^{N} A_{ij}^w \phi_{j,inv} + \sum_{j=1}^{N} C_{ij}^w \left(\frac{\partial \phi}{\partial n} \right)_j + \sum_{j=1}^{N+N_W} \left(\sum_{k=1}^{N} A_{jk}^w H_{kj} + B_{ij}^w \right) \sigma_j \\
&= \phi_{i,inv}^{wake} + \sum_{j=1}^{N+N_W} H_{ij}^w \sigma_j
\end{aligned}
$$

$$(2.21)$$

The viscous total potential should be:

$$
\begin{aligned}
\Phi_{i,vis}^{wake} &= \Phi_i^{in} + \phi_{i,vis}^{wake} \\
&= \Phi_i^{in} + \phi_{i,inv}^{wake} + \sum_{j=1}^{N+N_W} H_{ij}^w \sigma_j \\
&= \Phi_{i,inv}^{wake} + \sum_{j=1}^{N+N_W} H_{ij}^w \sigma_j
\end{aligned}
$$

$$(2.22)$$

12

Then the viscous or edge velocity can be written as:

$$
\begin{aligned}
U_{i,ivs}^{wake} &= \frac{\partial \Phi_{i,vis}^{wake}}{\partial s} \\
&= \frac{\partial \Phi_{i,inv}^{wake}}{\partial s} + \frac{\partial}{\partial s}\left(\sum_{j=1}^{N+N_W} H_{ij}^w \sigma_j \right) \\
&= U_{i,inv}^{wake} + \sum_{j=1}^{N+N_W} C_{ij}^w \sigma_j
\end{aligned}
\tag{2.23}
$$

(2.16) and (2.23) express the viscous velocity on the hydrofoil body and wake using the inviscid velocity, which can be solved by the low-order potential based panel method, and the induced velocity by the added blowing sources. The viscous velocity on the body and wake can be written in a general form:

$$
U_{i,vis} = U_{i,inv} + \sum_{j=1}^{N+N_W} G_{ij} \sigma_j
\tag{2.24}
$$

where $G_{ij} = C_{ij}$ on the hydrofoil body and $G_{ij} = C_{ij}^w$ on the wake. i is from 1 to $N + N_W$. The unknown strength of the blowing source is directly related to the boundary layer values by:

$$
\sigma = \frac{\partial (U_{vis}\delta^*)}{\partial s} = \frac{\partial m}{\partial s}
\tag{2.25}
$$

where δ^* is the displacement thickness of boundary layer, and $m = U_{vis}\delta^*$ is defined as the mass defect. (2.25) can be calculated numerically

$$
\sigma_j = \frac{m_{j+1} - m_j}{\Delta s}
\tag{2.26}
$$

By replacing the blowing source strength σ_j in (2.24) with (2.26), the final expression for viscous velocity is obtained:

$$
U_{i,vis} = U_{i,inv} + \sum_{j=1}^{N+N_W} D_{ij} m_j
\tag{2.27}
$$

13

where

$$D_{i,j} = \frac{G_{i,j-1}}{s_j - s_{j-1}} - \frac{G_{i,j}}{s_{j+1} - s_j} \tag{2.28}$$

2.4 The Viscous/Inviscid Flow Coupling

(2.27) needs to be combined with the 2D integral boundary layer equations. Then the combined equations can be solved together.

2.4.1 2D Integral Boundary Layer Equations

The 2D integral boundary layer equations include the standard integral momentum and the kinetic energy equation. A closure equation is used to close the system. For incompressible flow, the 2D integral boundary layer equations can be expressed as the followings:

- **Momentum equation**

$$\frac{\partial \theta}{\partial s} + (2 + H)\frac{\theta}{U_e}\frac{dU_e}{ds} = \frac{C_f}{2} \tag{2.29}$$

- **Kinetic energy equation**

$$\theta\frac{dH^*}{ds} + H^*(1 - H)\frac{\theta}{U_e}\frac{dU_e}{ds} = 2C_D - H^*\frac{C_f}{2} \tag{2.30}$$

- **Closure**

Closure for turbulent flows

$$\frac{\delta}{C_\tau} \frac{dC_\tau}{ds} = 5.6 \left[C_{\tau EQ}^{\frac{1}{2}} - C_\tau'^{\frac{1}{2}} \right]$$
$$+ 2\delta \left\{ \frac{4}{3\delta^*} \left[\frac{C_f}{2} - \left(\frac{H_k - 1}{6.7 H_k} \right)^2 \right] - \frac{1}{U_e} \frac{dU_e}{ds} \right\} \qquad (2.31)$$

Closure for laminar flows

$$\frac{d\tilde{n}}{ds} = \frac{d\tilde{n}(H_k)}{dR_{e\theta}} \frac{R_{e\theta}(H_k, \theta)}{ds} \qquad (2.32)$$

2.4.2   Coupling Algorithm

The brief solution procedures of this viscous/inviscid interactive method includes the following steps (as shown in Fig. 2.3): First, the inviscid velocity U_{inv} is calculated by the low-order potential based panel method. Then the viscous or the edge velocity U_{vis} is given as the inviscid velocity. The 2D integral boundary layer equations and the closure can be solved to obtain the boundary layer variables. Next, the viscous velocity is updated using (2.24). Repeat this process until a converged result is obtained.

2.5   2D Viscous Hydrofoil Case

A 2D hydrofoil case is carried out in order to validate the 2D viscous/inviscid interactive method and test how this method can capture the boundary layer characteristics. The hydrofoil is generated based on the NACA00 thickness form with $t_{max}/c = 0.1$. A camber with $f_{max}/c = 0.02$ is added. It

15
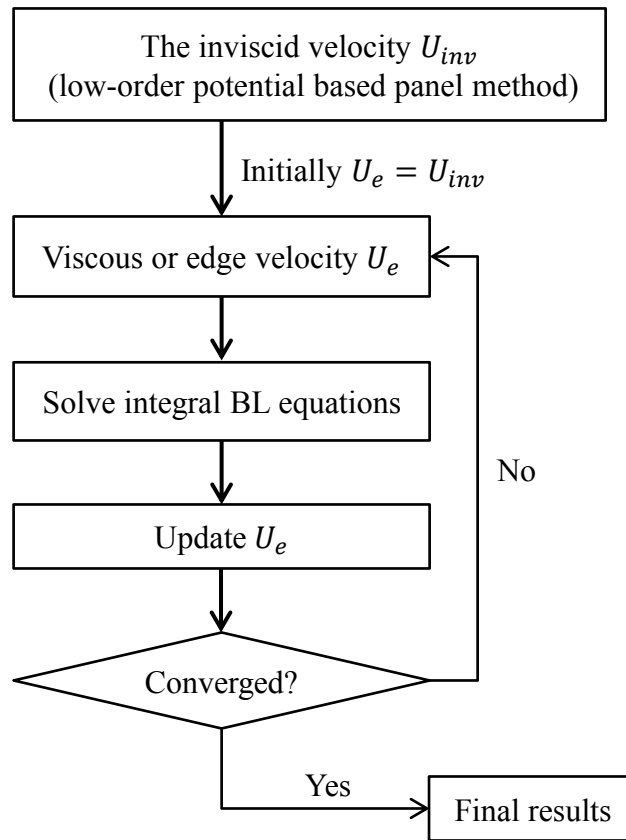
Figure 2.3: Flowchart of the 2D viscous/inviscid boundary layer method

is subject to a uniform inflow with zero angle of attack. The transition points on both pressure and suction side of the hydrofoil used in the present method are fixed close to the leading edge. The turbulence level is given as 1%. The Reynolds number is selected to be 5,000,000. The results predicted by the 2D viscous/inviscid interactive method and RANS (ANSYS/FLUENT) are compared.

2.5.1   Method Validation

A grid dependency study of the present viscous/inviscid interactive method is conducted first. The pressure distributions along the hydrofoil predicted by the present method using different numbers of panels are plotted in Fig. 2.4. The plots in Fig. 2.4 collapse into the same line, indicating that the changes of the number of panels on the hydrofoil do not affect the final results.

Another case of a reversed hydrofoil is conducted to validate the present method. The same NACA hydrofoil is reversed up and down as shown in Fig. 2.5. Subject to the same inflow, the pressure on the reversed hydrofoil is expected the same with that on the original hydrofoil. Fig. 2.6 plots the pressure distributions on the two hydrofoils predicted by the present method. The practically identical curves shown in Fig. 2.6 provide a good verification test of the present method.
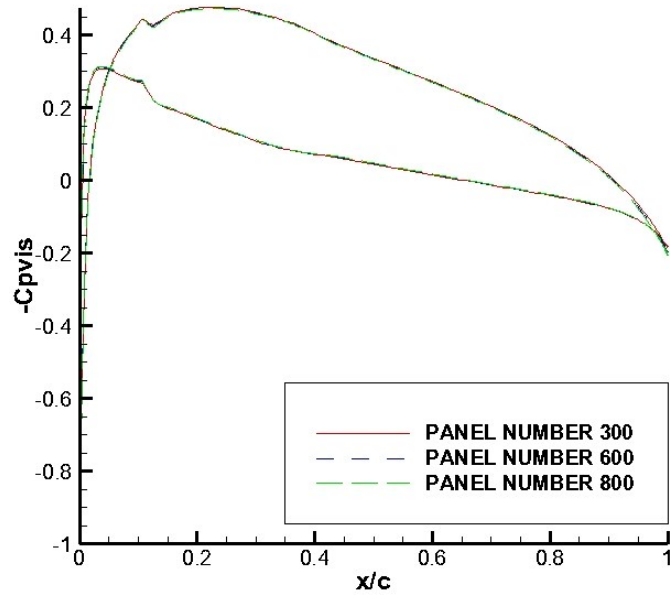
Figure 2.4: Pressure distributions along the hydrofoil subject to a uniform inflow with zero angle of attack, predicted by the present method with increasing number of panels, $R_e = \frac{U_\infty c}{v} = 5,000,000$, fixed transition points at 0.1 chord length on both pressure and suction sides, 1% turbulence level.

2.5.2 Result Comparison with RANS (ANSYS/FLUENT)

A grid dependence study of the RANS case is conducted first. The RANS simulations are carried out in a rectangular domain. A free stream condition with a specified velocity is imposed on the left, top and bottom boundaries. The outflow condition is set at the right boundary as the outlet of the domain. The grid details around the leading and trailing edge of the hydrofoil are shown in Fig. 2.7. The grid is refined and the three grids used in the grid dependency study are listed in Table 2.1. The plots of the pressure coefficient along the hydrofoil predicted by RANS using these three grids collapse into a same line (shown in Fig. 2.8), indicating that the grids work fine for this case.
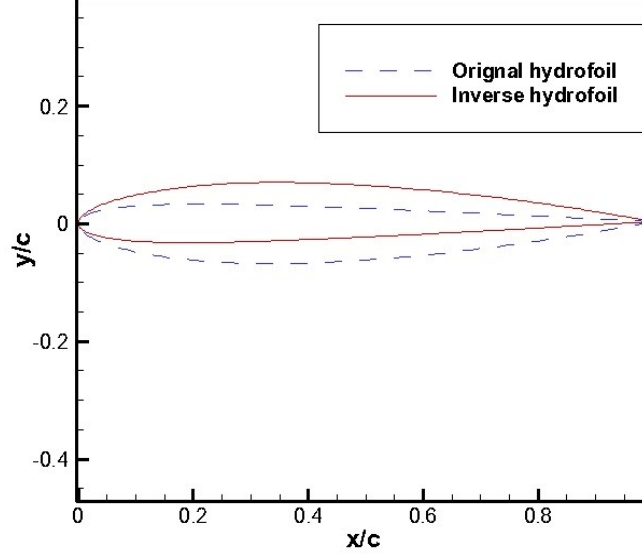
Figure 2.5: Diagram of the original hydrofoil and the reversed one ($t_{max}/c = 0.1$, $f_{max}/c = 0.02$).

19
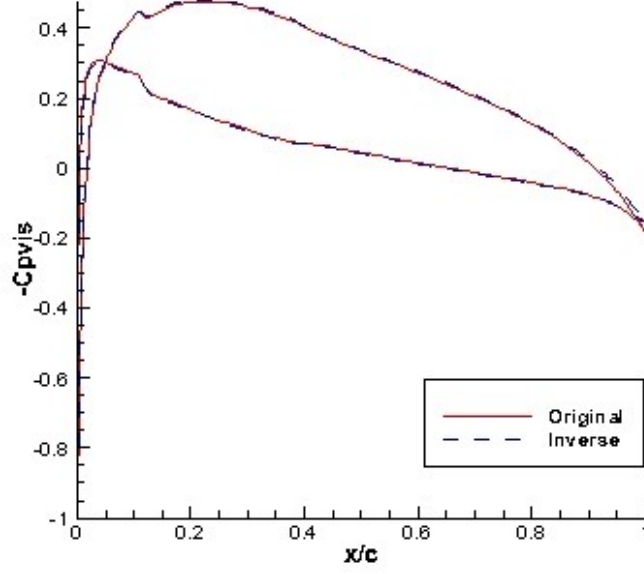
Figure 2.6: Pressure distributions along the two reversed hydrofoils subject to a uniform inflow with zero angle of attack, predicted by the present method, $R_e = \frac{U_\infty c}{v} = 5,000,000$, fixed transition points at 0.1 chord length on both the pressure and suction sides, 1% turbulence level.

(a) Leading edge
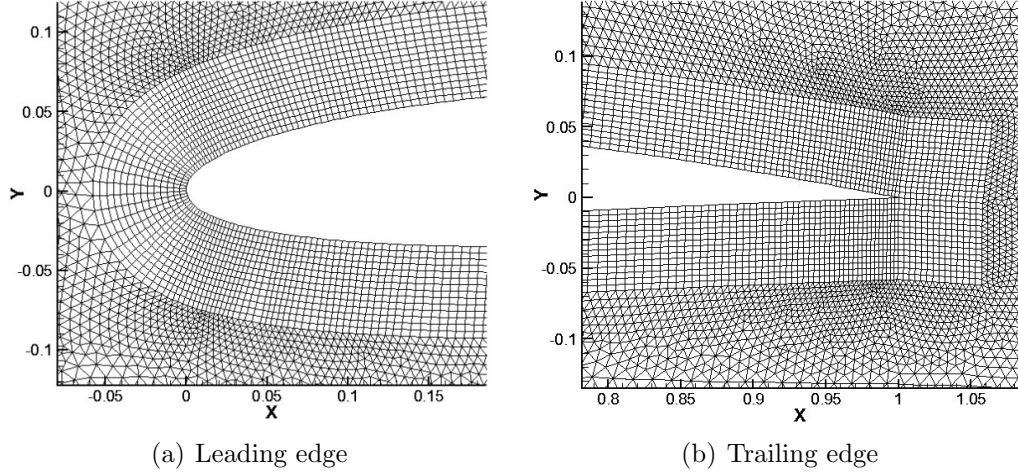
(b) Trailing edge

Figure 2.7: Grid details near the leading and trailing edge of the hydrofoil used in RANS (ANSYS/FLUENT) simulations.

20
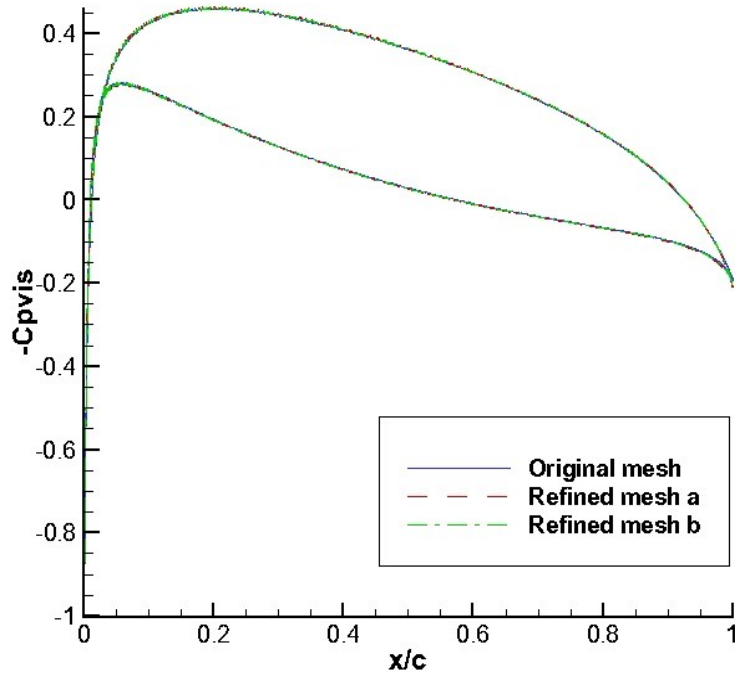
Figure 2.8: Pressure coefficients along the hydrofoil subject to a uniform inflow with zero angle of attack, predicted by RANS (ANSYS/FLUENT) using different grids, $R_e = \frac{U_\infty c}{v} = 5,000,000$.

Table 2.1: Three grids used for the grid dependency study of the RANS (ANSYS/FLUENT) case for 2D hydrofoil

Grid	Original	Refined a	Refined b
Cell number	45,878	473,822	1,259,924

To ensure sufficient resolution to capture the boundary layer characteristics, the value of y^+ on the hydrofoil surface should be limited to be less than 5. Fig. 2.9 plots $y+$ on the hydrofoil using the two refined meshes. Either one of the two meshes is proven to have sufficient resolution. The refined mesh b is used for the following study. The information for the RANS case is listed in Table. 2.2.

(a) Refined grid a   (b) Refined grid b
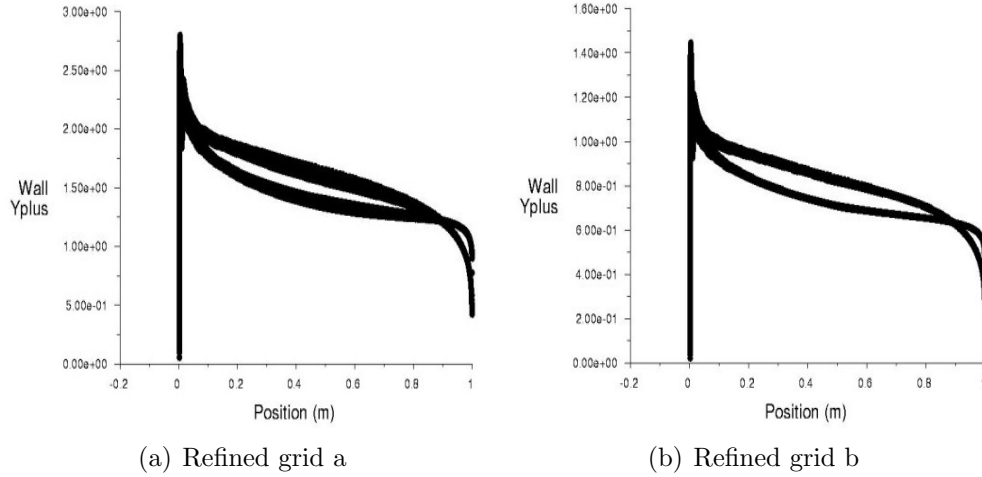
Figure 2.9: y^+ along the hydrofoil body subject to a uniform inflow with zero angle of attack, predicted by RANS (ANSYS/FLUENT) using the refined grid a and b, $R_e = \frac{U_\infty c}{v} = 5,000,000$.

The velocity vectors in the flow domain close to the hydrofoil trailing edge predicted by RANS are shown in Fig. 2.10. No separation happens in

Table 2.2: Information of the RANS (ANSYS/FLUENT) case for 2D hydrofoil

Reynolds number	$5,000,000$
Turbulence model	k-ω SST
Pressure correction scheme	SIMPLEC
Spatial discretization	Second order upwind
Total time for calculate (8 CPUs)	4,386 seconds

this case. Obvious effects of the boundary layer can be observed in the figure. To analyze the boundary layer quantitatively, the displacement thickness δ^* is introduced, which is defined as

$$\delta^* = \int_0^\infty \left(1 - \frac{u}{U_e}\right) dy \tag{2.33}$$

Eight points (shown in Fig. 2.11) are selected on the surface of the hydrofoil. Along the normal direction of each point, the velocity profile can be exported from the RANS case, and the displacement thickness at this point can be calculated by (2.33). The velocity profiles at point 2 and point 4 exported from RANS are plotted in Fig. 2.12. It is reasonable that the thicker boundary layer is observed at point 2, closer to the trailing edge, than 4. The comparison of the displacement thickness δ^* predicted by RANS and the 2D viscous/inviscid interactive method (shown in Fig. 2.13) shows considerable consistency. Fig. 2.14 plots the pressure distributions along the hydrofoil body predicted by different methods. The pressure predicted by the 2D viscous/inviscid interactive method shows a better correlation with RANS than the panel method only, which indicates that the present method can effectively predict the influences of the boundary layer on pressure. The skin friction coefficient $C_f = \frac{\tau_w}{\frac{1}{2}\rho U_\infty^2}$ is also compared in Fig. 2.15. The results from RANS (ANSYS/FLUENT) and

the present method show similar behavior. Although some differences can still be noticed in the comparison, the skin friction coefficient C_f predicted by the present method should be more reasonable C_f than any empirical constant.
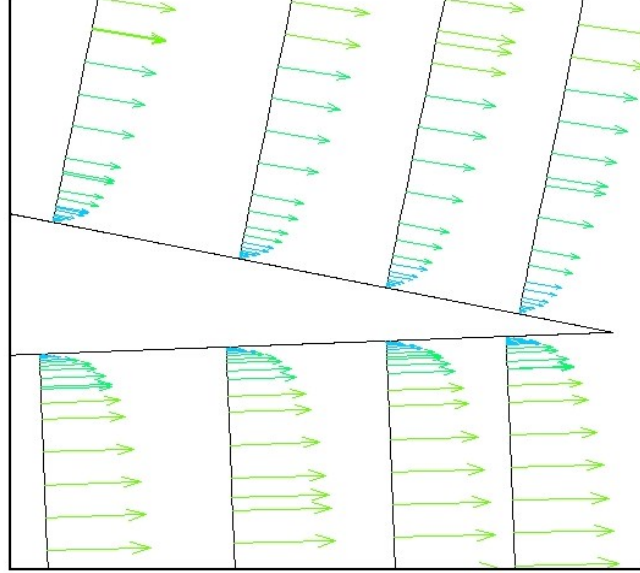
Figure 2.10: Velocity vectors close to the hydrofoil trailing edge in a uniform inflow with zero angle of attack, predicted by RANS (ANSYS/FLUENT), $R_e = \frac{U_\infty c}{v} = 5,000,000$.
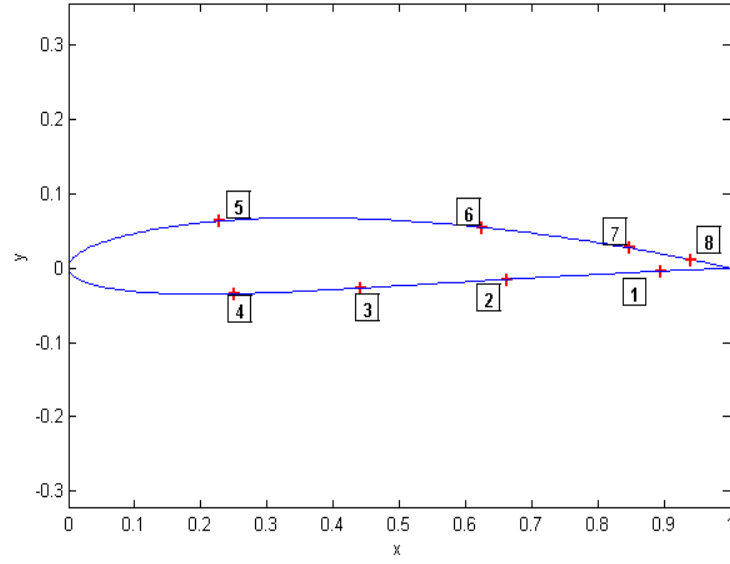
Figure 2.11: Diagram of the eight selected eight points
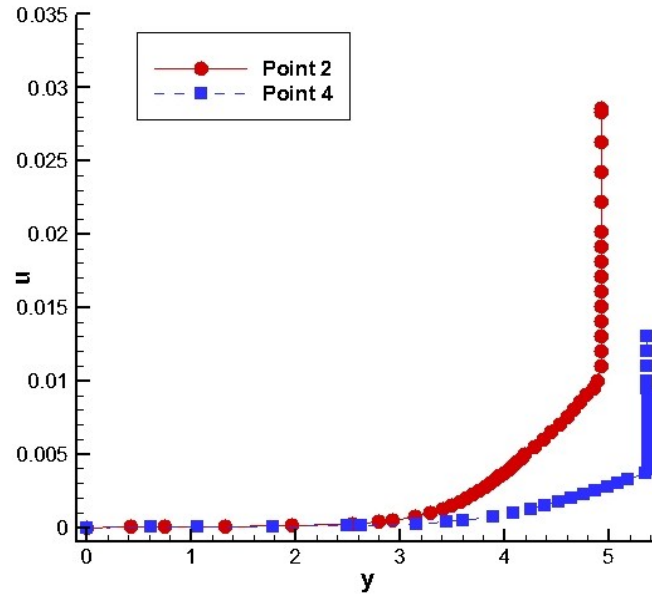
Figure 2.12: Velocity profiles at point 2 and 4 on the hydrofoil surface in a uniform inflow with zero angle of attack, predicted by RANS (ANSYS/FLUENT), $R_e = \frac{U_\infty c}{v} = 5,000,000$.

25

(a) Pressure side   (b) Suction side
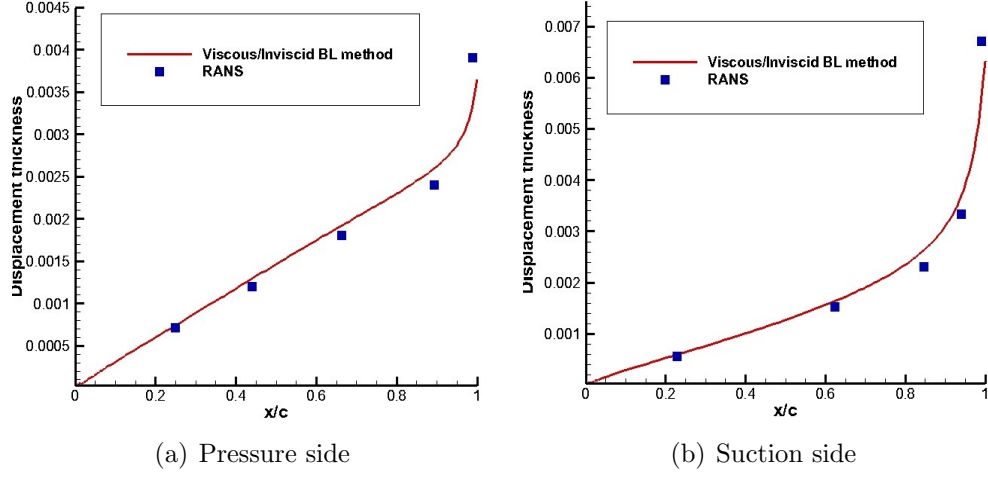
Figure 2.13: Comparison of δ^* on the surface of the hydrofoil subject to a uniform inflow with zero angle of attack, between RANS (ANSYS/FLUENT) and the present method, $R_e = \frac{U_\infty c}{v} = 5,000,000$.

(a) RANS vs. Panel method   (b) RANS vs. present method
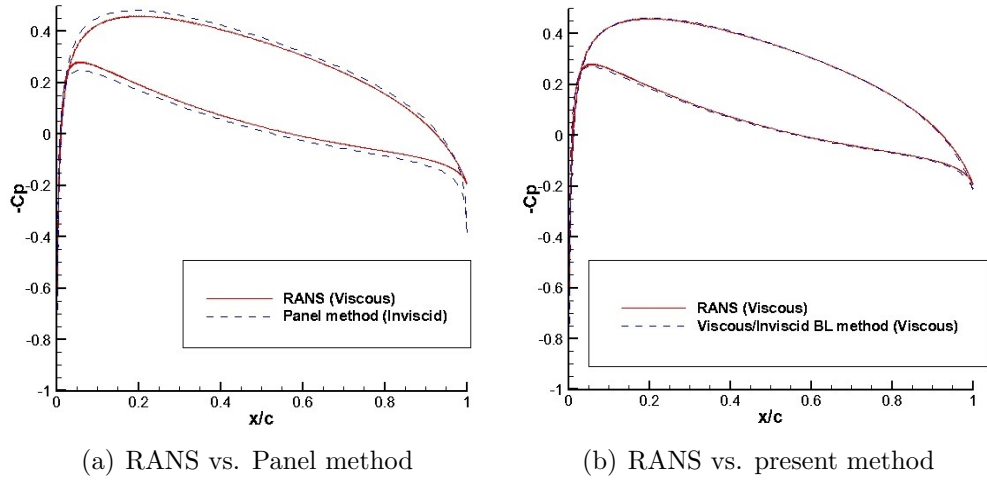
Figure 2.14: Comparison of C_p on the surface of the hydrofoil subject to a uniform inflow with zero angle of attack, between RANS (ANSYS/FLUENT) and the present method, $R_e = \frac{U_\infty c}{v} = 5,000,000$.

26
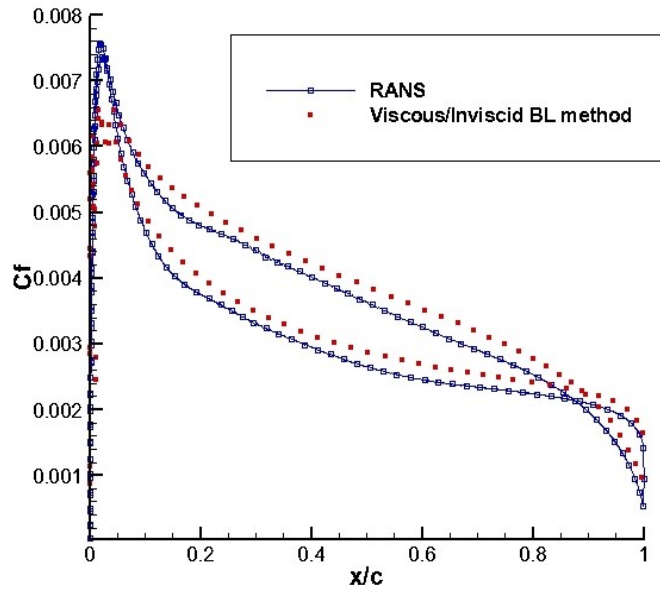
Figure 2.15: Comparison of C_f on the surface of the hydrofoil subject to a uniform inflow with zero angle of attack, between RANS (ANSYS/FLUENT) and the present method, $R_e = \frac{U_\infty c}{v} = 5,000,000$.

Chapter 3

Three Dimensional Viscous/Inviscid Interactive Method

In this chapter, the author follows the assumption of Hufford (1992, 1994) that the effects of the boundary layer on the span wise direction is negligible compared with those on the stream wise direction. For the boundary layer on propeller blades, it is assumed that the boundary layer radially outward could be ignored, while the boundary layer along the constant radius needs to be considered. Based on the above assumption, a more reasonable and complete 3D viscous/inviscid interactive method is developed by coupling a low-order potential based panel method and the 2D integral boundary layer analysis. A significant improvement of this method, as compared with the work of Hufford (1992, 1994) and Sun (2008), is that the viscous effects of neighboring strips and blades are considered. The present method is introduced in details at first. Then two propellers and a bare duct cases are carried out. The results predicted by the 3D viscous/inviscid boundary layer method are presented and correlated with those of RANS cases or experimental measurements.

3.1 Assumption

Milewski (1997) developed a 3D fully simultaneous viscous/inviscid interactive scheme, by coupling a potential based panel method and the 3D integral boundary layer equations. His scheme is totally three dimensional and involves a large number of unknowns. He solved the whole system using Newton's method, which needs to calculate many sensitivities. Thus solving this scheme requires large amounts of computational resources. This scheme was only applied to some cases with simple geometries such as hydrofoils or axis-symmetric ducts. For more complicated geometries such as propellers, this scheme may have more difficulties. For propeller flows particularly, to avoid solving the 3D integral boundary layer equations, it can be assumed that the effects of the boundary layer variables radially outward are much smaller than those along the constant radius. Thus radial effects could be negligible. In fact, this assumption is reasonable according to the measurements of Jessup (1989). In addition, the RANS results of Propeller NSRDC4381 (more information and results of this propeller will be presented in later sections) in this thesis also verify the assumption. Fig. 3.1 shows one blade of the propeller. Define the direction along the constant radius as s and the direction radially outward as t. The two velocity components in s and t directions along the normal vector of the blade surface $s \times t$ are checked at two strips $r/R = 0.6$ and $r/R = 0.95$, so that the effects of the boundary layer in the two directions could be investigated. Fig. 3.2 and Fig. 3.3 show the velocity profiles at the middle and end chord (close to trailing edge) of the strip $r/R = 0.6$ at design

J. Close to the tip of the blade $r/R = 0.95$, the velocity profiles are plotted in Fig. 3.4 and Fig. 3.5. Fig. 3.6, Fig. 3.7, Fig. 3.8 and Fig. 3.9 plot similar results at $J = 0.5$. For the case of $J = 0.5$, the boundary layer effects along $\boldsymbol{t}$ direction are very limited and localized compared with those along $\boldsymbol{s}$ direction, as the assumption states. In the case of design J, the assumption is valid on the most parts of the blade. However, very close to the blade tip, the effects of the boundary layer along $\boldsymbol{t}$ are as significant as those of the boundary layer along $\boldsymbol{s}$, as shown in Fig. 3.4(b) and Fig. 3.5(b).
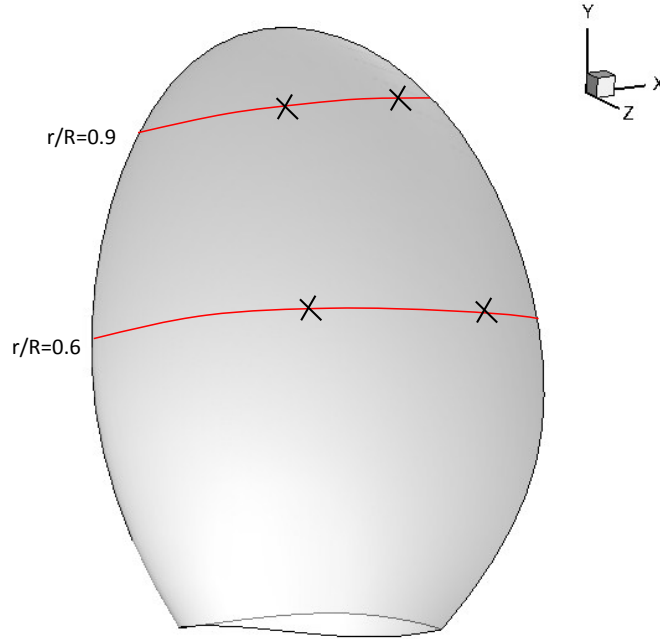
Figure 3.1: Blade geometry of Propeller NSRDC4381

(a) Pressure side   (b) Suction side
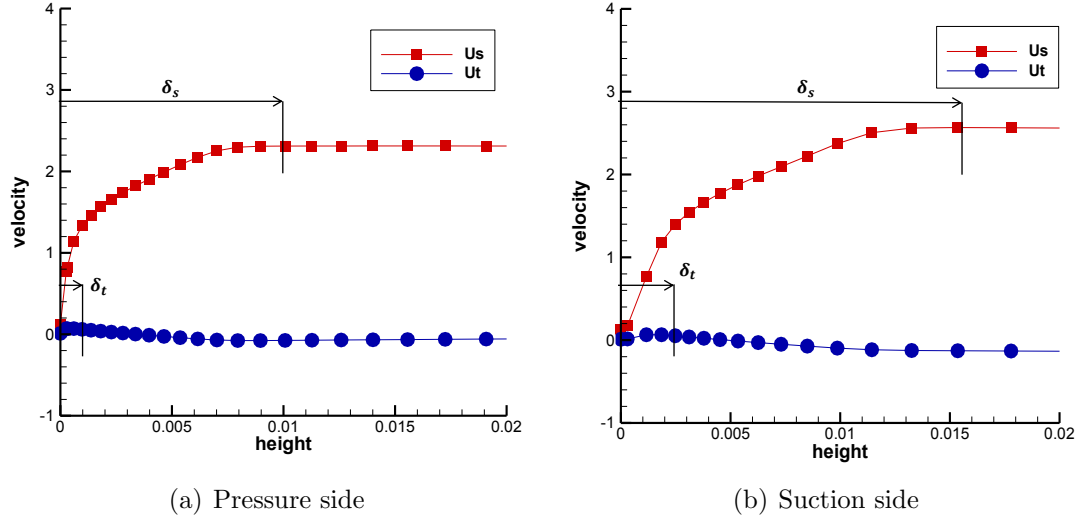
Figure 3.2: Velocity components in $\boldsymbol{t}$ and $\boldsymbol{s}$ directions at the middle chord of the strip $r/R = 0.6$, of propeller 4381, predicted by RANS (ANSYS/FLUENT), $J_s = 0.889$.

(a) Pressure side   (b) Suction side
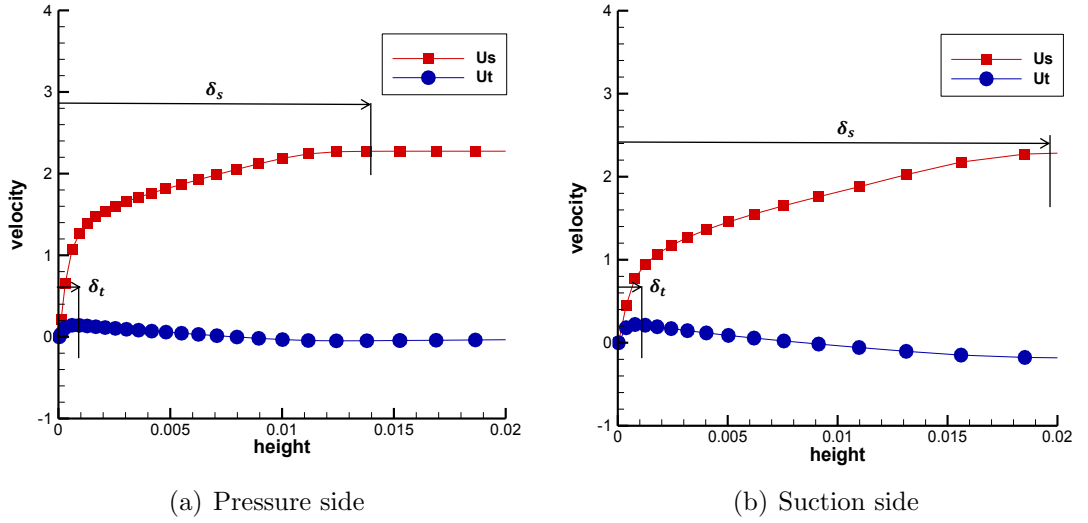
Figure 3.3: Velocity components in $\boldsymbol{t}$ and $\boldsymbol{s}$ directions at the end chord (close to trailing edge) of the strip $r/R = 0.6$, of propeller 4381, predicted by RANS (ANSYS/FLUENT), $J_s = 0.889$.

31
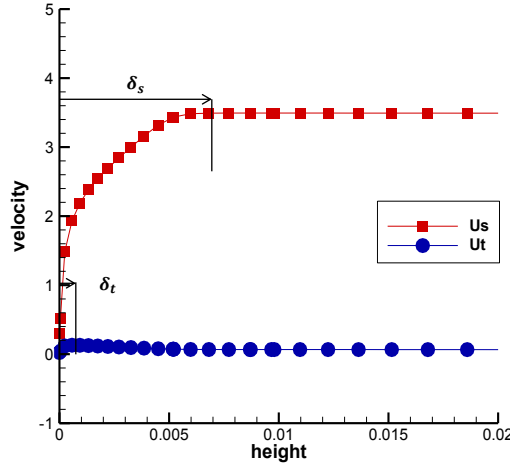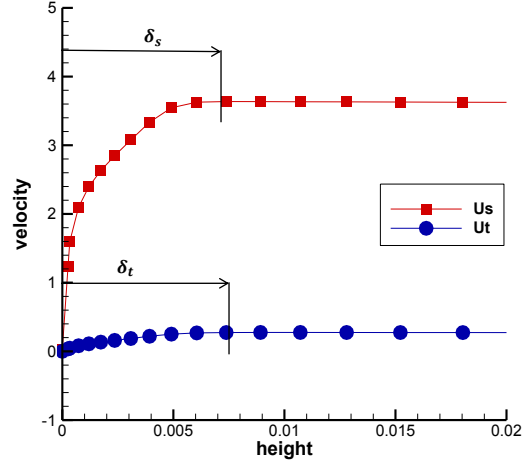
(a) Pressure side

(b) Suction side

Figure 3.4: Velocity components in t and s directions at the middle chord of the strip $r/R = 0.95$, of propeller 4381, predicted by RANS (ANSYS/FLUENT), $J_s = 0.889$.
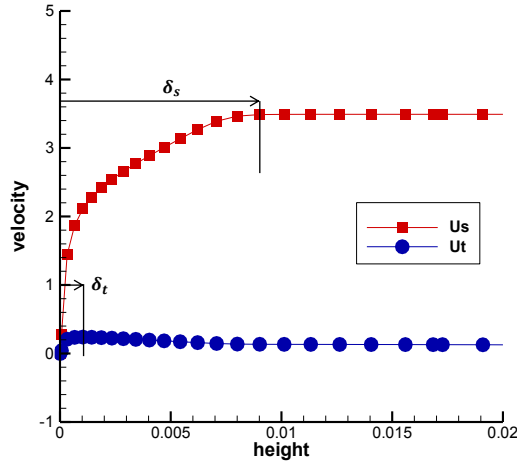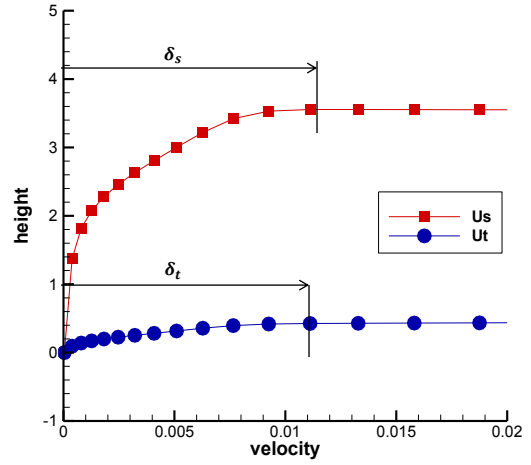
(a) Pressure side

(b) Suction side

Figure 3.5: Velocity components in t and s directions at the end chord (close to trailing edge) of the strip $r/R = 0.95$, of propeller 4381, predicted by RANS (ANSYS/FLUENT), $J_s = 0.889$.
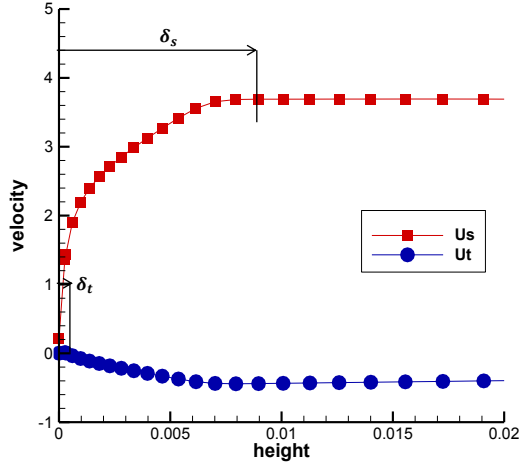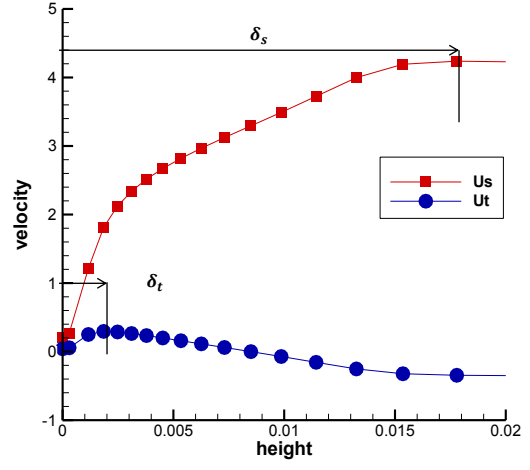
(a) Pressure side (b) Suction side

Figure 3.6: Velocity components in $\boldsymbol{t}$ and $\boldsymbol{s}$ directions at the middle chord of the strip $r/R = 0.6$, of propeller 4381, predicted by RANS (ANSYS/FLUENT), $J_s = 0.5$.
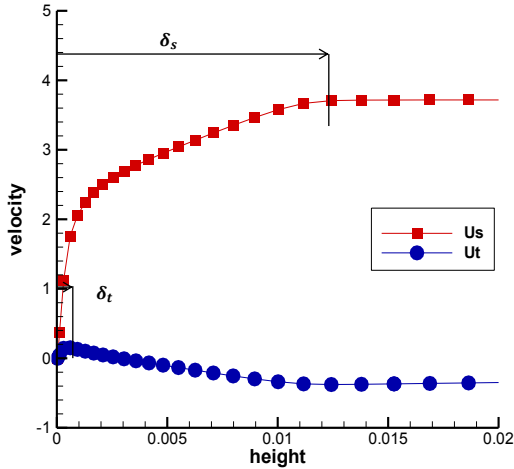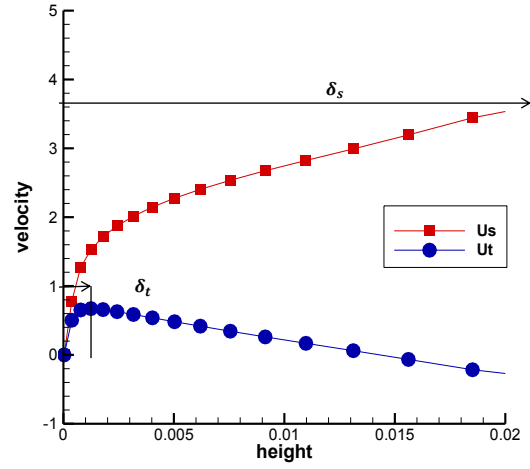
(a) Pressure side (b) Suction side

Figure 3.7: Velocity components in $\boldsymbol{t}$ and $\boldsymbol{s}$ directions at the end chord (close to trailing edge) of the strip $r/R = 0.6$, of propeller 4381, predicted by RANS (ANSYS/FLUENT), $J_s = 0.5$.
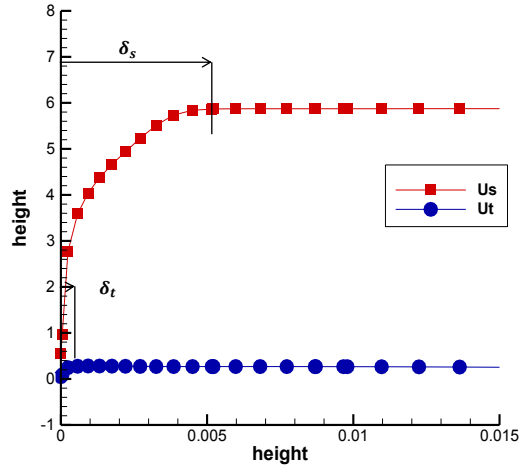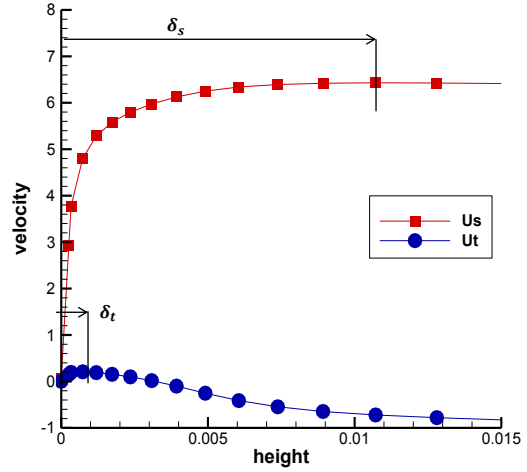
(a) Pressure side   (b) Suction side

Figure 3.8: Velocity components in $\boldsymbol{t}$ and $\boldsymbol{s}$ directions at the middle chord of the strip $r/R = 0.95$, of propeller 4381, predicted by RANS (ANSYS/FLUENT), $J_s = 0.5$.
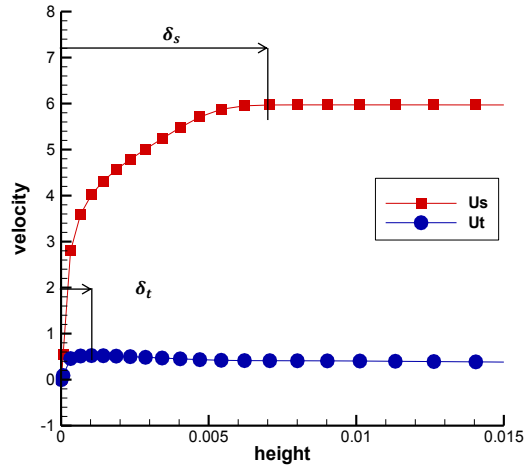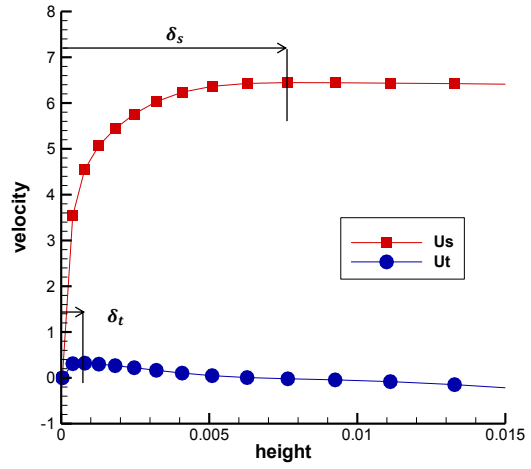
(a) Pressure side   (b) Suction side

Figure 3.9: Velocity components in $\boldsymbol{t}$ and $\boldsymbol{s}$ directions at the end chord (close to trailing edge) of the strip $r/R = 0.95$, of propeller 4381, predicted by RANS (ANSYS/FLUENT), $J_s = 0.5$.

34

3.2　3D Wall Transpiration Model

Following the assumption mentioned in the above section, a 3D propeller blade is divided into several strips along the constant radius as shown in Fig. 3.10. The boundary layer along each strip is considered. Similar with the 2D model, this 3D model also expresses the edge or viscous velocity as the sum of the inviscid velocity and the induced velocity by blowing sources added on blades and wakes. Detailed derivation of the expression of the edge velocity is presented. The equation of the edge velocity should be resolved with the 2D integral boundary layer equations on the strips. Compared with the 2D case, the expression of the edge velocity for 3D case contains more unknowns, so the combined equations cannot be solved directly. Therefore, this 3D model applies an iterative scheme to solve for the extra unknowns. The procedures of this scheme is introduced in details.

3.2.1　One Blade

Similar with the 2D case, blowing sources with unknown strengths are added on the blade and wake panels when the effects of fluid viscosity are considered. Analogous to (2.24), the viscous or edge velocity on the 3D blade and the wake has two components: the inviscid velocity and the induced velocity by the blowing sources. Considering a control point i on a strip m, the viscous velocity should be written as:

$$U_{i,m}^e = \frac{\partial \Phi_{i,m}}{\partial s} = U_{i,m}^{inv} + \sum_{j=1}^{N+N_W} D_{i,j,m} m_{j,m} + \sum_{k=1,k\neq m}^{mr} \sum_{j=1}^{N+N_W} D_{i,j,k} m_{j,k} \qquad (3.1)$$

where mr is the number of strips. Compared with (2.24), the extra term in (3.1) represents the induced velocity by the sources on other strips (except strip m). It should be noticed that the influence coefficient $D_{i,j,k}$ in (3.1) is different than that in (2.24). In this case, the influence coefficients should be calculated using the 3D formulations (see appendix), since the panels of each strip are three dimensional. In (2.24), however, the influence coefficients are calculated using the formulations for 2D panels (see appendix).
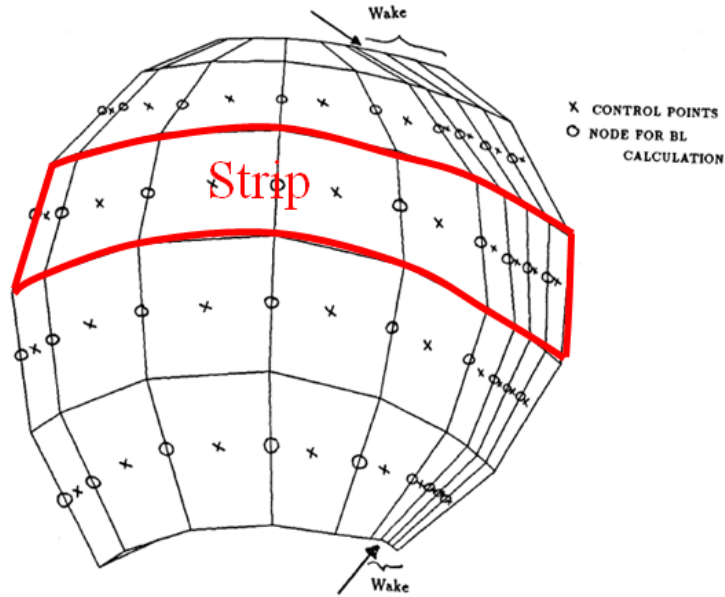
Figure 3.10: Sketch of 3D blade paneling

The unknown mass defects $m_{j,k}$ in (3.1) should be resolved with the integral boundary layer equations from (2.29) to (2.32). However, the term $\sum_{k=1,k\neq m}^{mr} \sum_{j=1}^{N+N_W} D_{i,j,k} m_{j,k}$ in (3.1) introduces extra unknowns, so that the combined equations cannot be solved directly. An iterative scheme is intro-

duced to solve for all the unknowns. First, the inviscid velocity is calculated by the 3D low-order potential based panel method. Then the unknown mass defects in the term $\sum_{k=1,k\neq m}^{mr} \sum_{j=1}^{N+N_W} D_{i,j,k} m_{j,k}$ are initially given as zero to reduce the number of unknowns. Next, (3.1) can be resolved by the 2D integral boundary layer solver used in XFOIL on each strip independently. Based on the solved mass defects, the term $\sum_{k=1,k\neq m}^{mr} \sum_{j=1}^{N+N_W} D_{i,j,k} m_{j,k}$ is updated and added into the inviscid velocity term $U_{i,m}^{inv}$. Solve for the mass defects on each strip again. Repeat the above procedures until a converged result is obtained. The brief solution procedures of this scheme are shown in Fig. 3.11.

3.2.2 Multiple Blades

When multiple blades are considered, (3.1) becomes:

$$
\begin{aligned}
U_{i,m,1}^e &= \frac{\partial \Phi_{i,m,1}}{\partial s} \\
&= U_{i,m,1}^{inv} + \sum_{j=1}^{N+N_W} D_{i,j,m,1} m_{j,m,1} + \sum_{k=1,k\neq m}^{mr} \sum_{j=1}^{N+N_W} D_{i,j,k,1} m_{j,k,1} \\
&\quad + \sum_{kk=2}^{NB} \sum_{k=1}^{mr} \sum_{j=1}^{N+N_W} D_{i,j,k,kk} m_{j,k,kk}
\end{aligned}
\tag{3.2}
$$

where NB is the number of blades. The blade $kk = 1$ is the key blade. The term $\sum_{kk=2}^{NB} \sum_{k=1}^{mr} \sum_{j=1}^{N+N_W} D_{i,j,k,kk} m_{j,k,kk}$ represents the induced velocity by the sources added on other blades (except the key blade). For steady cases, the boundary layer variables on other blades are the same with those on the key blade, for instance, $m_{j,m,kk} = m_{j,m,1}$. Thus (3.2) can be rewritten as the

The inviscid velocity U_{inv}
(low-order potential based panel method)

Initially $D_{i,j,k} = 0$

Update the induced velocity
from other strips
$\sum_{k=1,k\neq m}^{mr} \sum_{j=1}^{N+Nw} D_{i,j,k} m_{j,k}$

Update the inviscid velocity
U_{inv}

Solve for mass defects $m_{j,k}$
on each strip

Converged?

No

Yes

Final results
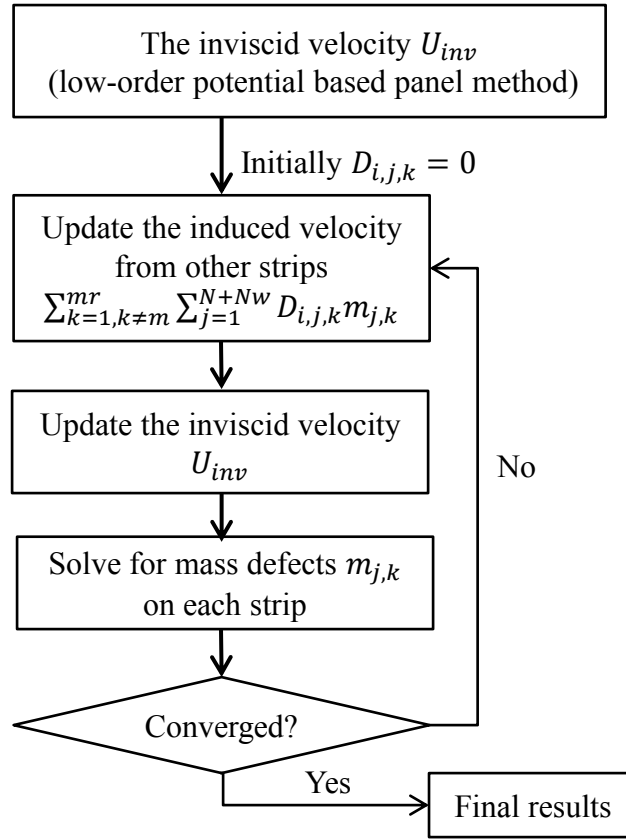
Figure 3.11: Flowchart of the iterative scheme for 3D viscous/inviscid boundary layer method

following:

$$U_{i,m,1}^e = U_{i,m,1}^{inv} + \sum_{j=1}^{N+N_W} D_{i,j,m,1} m_{j,m,1} + \sum_{kk=2}^{NB} \sum_{j=1}^{N+N_W} D_{i,j,m,kk} m_{j,m,kk}$$
$$+ \sum_{k=1,k\neq m}^{mr} \sum_{j=1}^{N+N_W} \left(D_{i,j,k,1} + \sum_{kk=2}^{NB} D_{i,j,k,kk} \right) m_{j,k,1} \tag{3.3}$$

(3.3) is very useful for the simplification of coding. Using the similar proce-
dures shown in Fig. 3.11, all the unknowns in (3.3) can be resolved. In fact,
the effects from other blades are very limited. Fig. 3.12 compares the pressure
along two different strips, $r/R = 0.6$ and $r/R = 0.9$, on the key blade with
and without the effects of other blades of Propeller NSTDC 4381 at design
condition $J_s = 0.889$. The comparisons prove the above statement about the
limited effects of other blades.

3.3 Propeller DTMB4119

Propeller DTMB4119 is a 3 bladed propeller (shown in Fig. 3.13). The
design advance ratio of this propeller J_s is 0.833. Jessup (1989) investigated
the pressure and the boundary layer characteristics on the propeller blades
experimentally. The 3D viscous/inviscid interactive method described above
is applied to this propeller, and the results are correlated with the experimental
data from Jessup (1989). Before any further investigation, a grid dependency
study is conducted to validate the present method. Both the numbers of panels
along the chord wise and span wise directions are changed. Fig. 3.14 plots
the pressure distributions along the strip at $r/R = 0.62$. Despite the changes

(a) r/R=0.6   (b) r/R=0.9
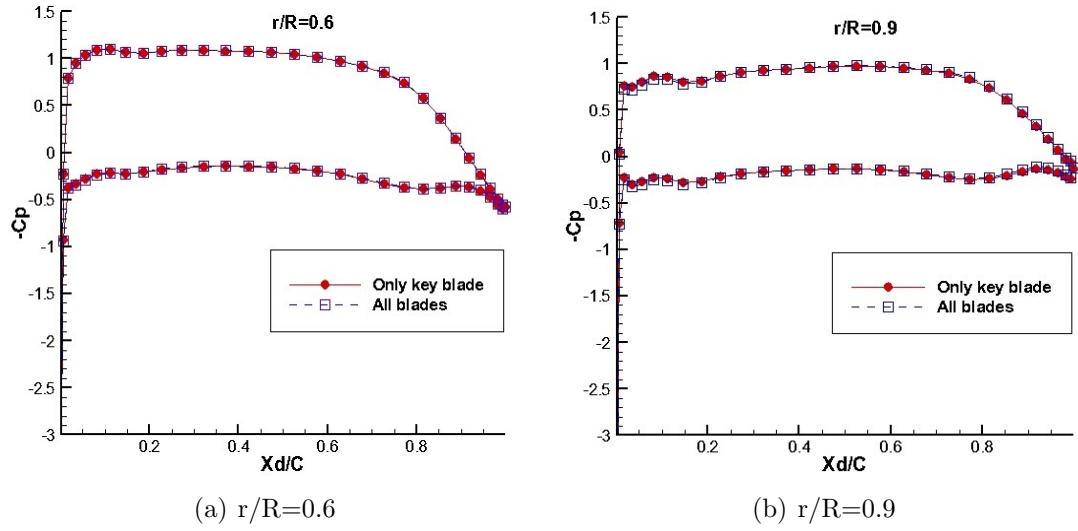
Figure 3.12: Pressure distributions along two different strips, r/R=0.6 and r/R=0.9, of Propeller NSTDC 4381, predicted by the present method with and without the effects of blowing sources added on neighboring blades, $J_s = 0.889$, $R_e = \frac{U_\infty D}{v} = 7.42e5$, 1% turbulence level, fixed transition points at 0.1 chord length on both the pressure and suction sides of each strip.

of the panel numbers, the plots of the pressure distribution predicted by the present method collapse into the same line, indicating that the method and the code work fine.

The iterative scheme (shown in Fig. 3.11) is applied to solve for all the unknowns. Fig. 3.15 shows the pressure distributions at different iterations along the strip at $r/R = 0.62$. The plots of the pressure at the 4th and 5th iteration collapse with each other, indicating that a converged result is already obtained at the 5th iteration. It should be mentioned that the result of the first iteration is the one (Hufford's result) that does not consider the effects of blowing sources on neighboring strips and blades.

Fig. 3.16 and Fig. 3.17 compare the displacement thickness δ^* along
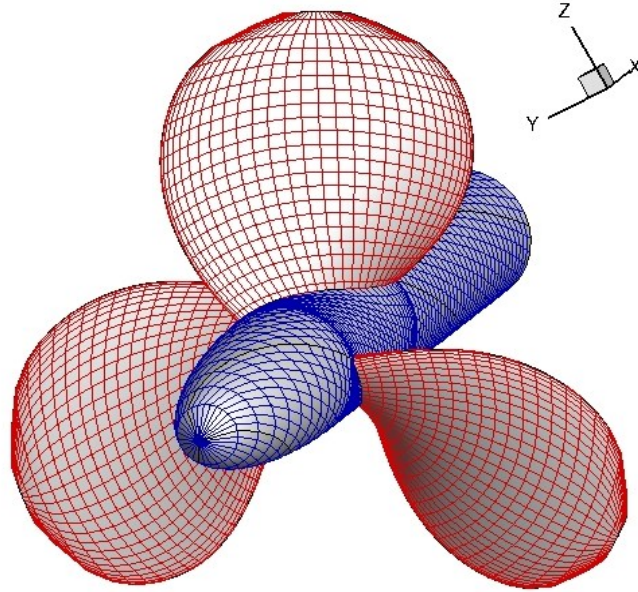
Figure 3.13: Paneled geometry of Propeller DTMB4119

Figure 3.14: Pressure distributions predicted by the present method using different numbers of panels along the strip $r/R = 0.62$ of Propeller DTMB4119, $J_s = 0.833$, $R_e = \frac{U_\infty D}{v} = 766,395$, 1% turbulence level, fixed transition points at 0.1 chord length on both the pressure and suction sides of each strip.

(a) Full view

(b) Details close to the trailing edge
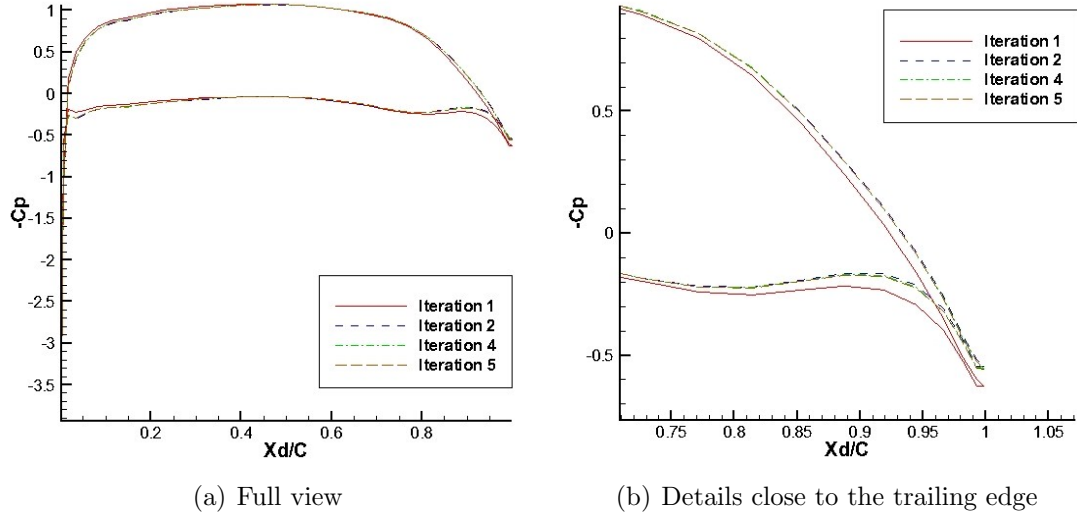
Figure 3.15: Pressure distributions at different iterations on the strip $r/R = 0.62$ of Propeller DTMB4119, predicted by the present method, $J_s = 0.833$, $R_e = \frac{U_\infty D}{v} = 766,395$, 1% turbulence level, fixed transition points at 0.1 chord length on both the pressure and suction sides of each strip.

the strip at $r/R = 0.7$ predicted by the present method with the experimental measurements. The comparison on the suction side shows considerable consistency. On the pressure side, even though the experimental data is insufficient for detailed comparison, the results predicted by the present method and the experimental measurements show a same trend. The comparisons of the pressures along different strips between the experiment and the present method are shown from Fig. 3.18 to Fig. 3.20. Considering the difficulties and the errors of the experimental measurements, the comparisons shown in the figures are acceptable.

For 3D propeller blade cases, the prediction of the thrust/torque forces at various operating conditions is a main concern. The forces consist of two

43
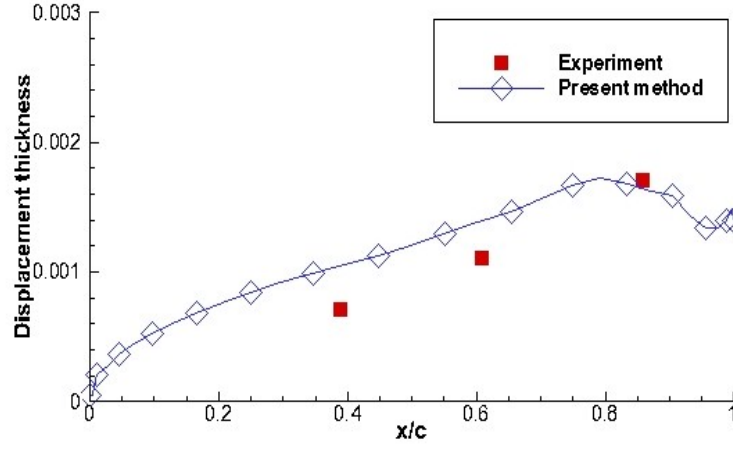
Figure 3.16: Comparison of displacement thickness on the pressure side of the strip $r/R = 0.7$ of Propeller DTMB4119 between experiments and the present method (free transition point on the pressure side of each strip, 1% turbulence level), $J_s = 0.833$, $R_e = \frac{U_\infty D}{v} = 766,395$.
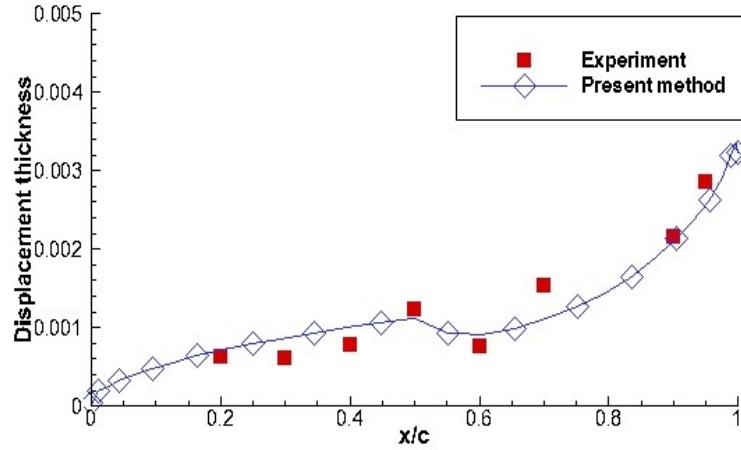
Figure 3.17: Comparison of displacement thickness on the suction side of the strip $r/R = 0.7$ of Propeller DTMB4119 between experiments and the present method (fixed transition point at 0.5 chord length on the suction side of each strip, 1% turbulence level), $J_s = 0.833$, $R_e = \frac{U_\infty D}{v} = 766,395$.
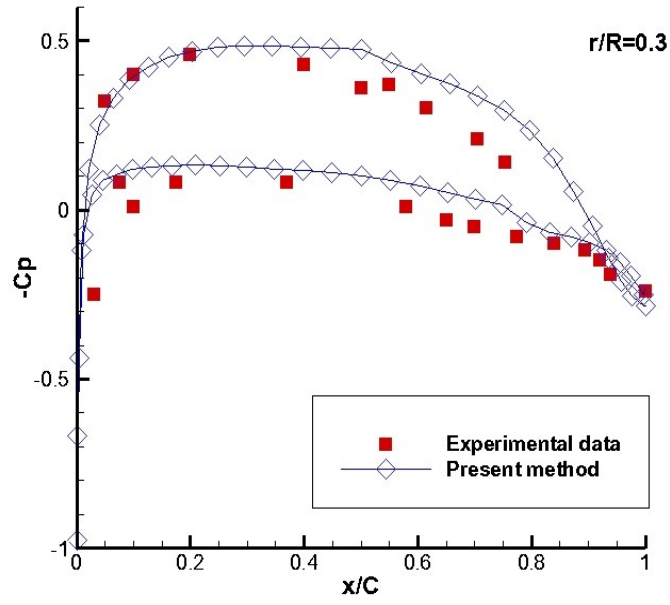
Figure 3.18: Comparison of pressure coefficients on the strip, $r/R = 0.3$ of, of Propeller DTMB4119 between experiments and the present method (fixed transition point at 0.5 chord length on the suction side and free transition point on the pressure side of each strip, 1% turbulence level), $J_s = 0.833$, $R_e = \frac{U_\infty D}{v} = 766,395$.
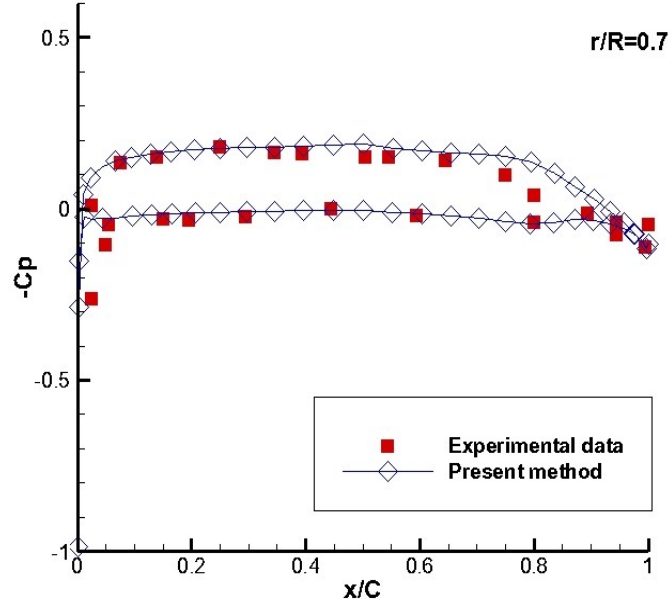
Figure 3.19: Comparison of pressure coefficients on the strip, $r/R = 0.7$ of, of Propeller DTMB4119 between experiments and the present method (fixed transition point at 0.5 chord length on the suction side and free transition point on the pressure side of each strip, 1% turbulence level), $J_s = 0.833$, $R_e = \frac{U_\infty D}{v} = 766,395$.
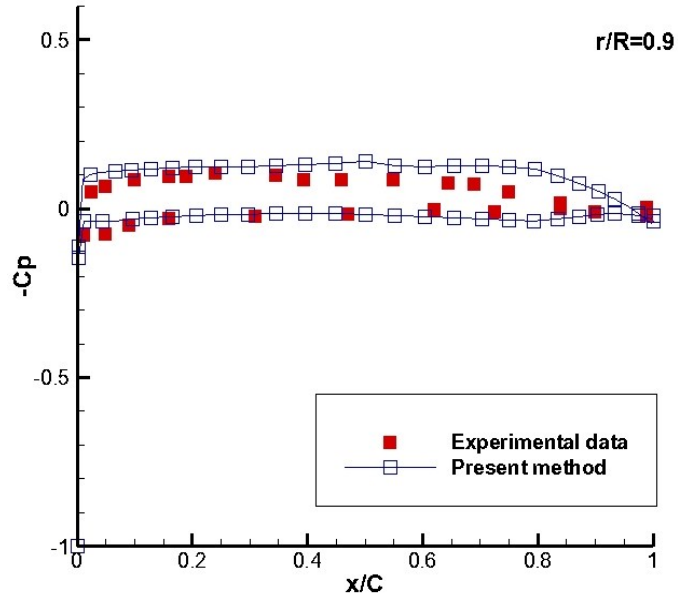
Figure 3.20: Comparison of pressure coefficients on the strip, $r/R = 0.9$ of, of Propeller DTMB4119 between experiments and the present method (fixed transition point at 0.5 chord length on the suction side and free transition point on the pressure side of each strip, 1% turbulence level), $J_s = 0.833$, $R_e = \frac{U_\infty D}{v} = 766,395$.

parts: one part is due to the friction on propeller blades and the other part is due to the pressure. Panel methods ignore the effects of fluid viscosity, thus cannot take the friction into consideration and cannot predict the influences of boundary layer on pressure. An easy solution of this dilemma is to apply empirical methods to consider the effects of fluid viscosity. However, such method requires user adjustable corrections that are not general for all cases. It has been proved that the viscous/inviscid interactive method can precisely predict the changes of pressure on the wall due to boundary layer. For the friction part, instead of using the empirical constants, the 3D viscous/inviscid interactive method can predict more reasonable skin friction coefficient C_f on propeller blades. Then the forces due to the friction are calculated by integrating the shear stress $\tau_w = C_f \cdot \frac{1}{2}\rho U_\infty^2$ over the blade surfaces. Fig. 3.21 shows the comparisons of K_T and K_Q between the experimental measurements and the present method. The results predicted by the present method exhibit considerable agreement with the experimental data.

3.4   Propeller NSRDC4381

The 3D viscous/inviscid interactive method is also applied to Propeller NSRDC4381, which is a five-bladed propeller (shown in Fig. 3.22). The design advance ratio J_s of this propeller is 0.889. The results predicted by the present method and RANS (ANSYS/FLUENT) simulations conducted by Tian and Kinnas (2011) are compared. Fig. 3.23 shows the domain and boundary conditions for RANS (ANSYS/FLUENT) simulations. The grid details are shown
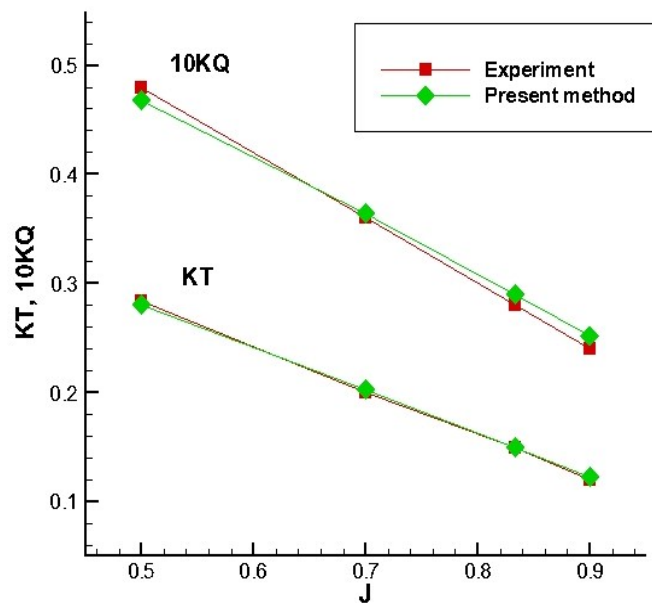
Figure 3.21: Comparisons of K_T and K_Q of Propeller DTMB4119 at different advance ratios, between experiments and the present method.

in Fig. 3.24. Some important information of the RANS (ANSYS/FLUENT) cases is listed in Table. 3.1.
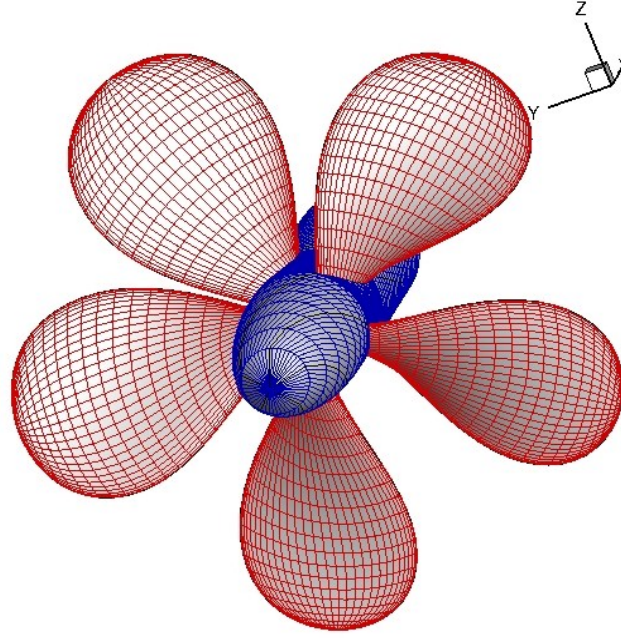
Figure 3.22: Paneled geometry of Propeller NSRDC4381.

For the present 3D viscous/inviscid interactive method, it is necessary to conduct a grid dependency study at first. The pressure distributions with different numbers of panels along two strips on the propeller blade are compared in Fig. 3.25. The great consistency shown in Fig. 3.25 indicates that the changes of the number of panels on both chord and span wise directions do not affect the final results. The pressure distributions at different iterations are checked as well (shown in Fig. 3.26) to ensure the convergence of the results.

The 3D viscous/inviscid interactive method is applied to predict the pressure on the blades of propeller 4381. Fig. 3.27 to Fig. 3.30 shows detailed

comparisons of pressure at two different operating conditions: the design condition ($J_s = 0.889$) and an off-design condition ($J_s = 0.5$). The pressures predicted by the present method show better correlation with the RANS results than those predicted by the panel method only, especially at the region close to the blade trailing edge. Closer to the trailing edge, the effects of fluid viscosity become more significant and the boundary layer becomes thicker. Thus more clear improvements of the results are observed in this region with the boundary layer correction.

The thrust/torque forces due to the fluid viscosity is calculated by integrating the shear stress τ over the blade surfaces. Fig. 3.31 shows the comparison of C_f predicted by the present method and RANS at the design
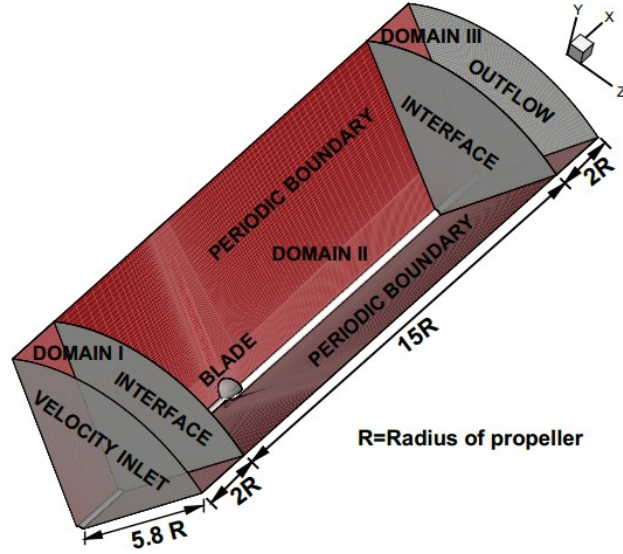
Figure 3.23: Domain and boundary conditions of the RANS (ANSYS/FLUENT) case for Propeller NSRDC4381 (from Sharma 2011).
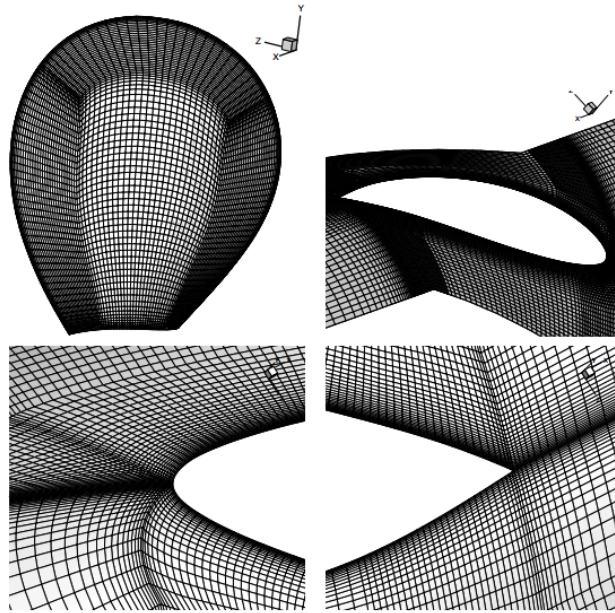
Figure 3.24: Grid details used in the RANS (ANSYS/FLUENT) case for Propeller NSRDC4381. Top left: O type grid on the propeller blade. Top right: grid details on the hub around the root section of the propeller blade. Bottom left: Grid details on the hub near the leading edge of the root section of propeller blade. Bottom right: grid details on the hub near the trailing edge of the root section of the propeller blade. (from Sharma 2011).

(a) r/R=0.6   (b) r/R=0.9
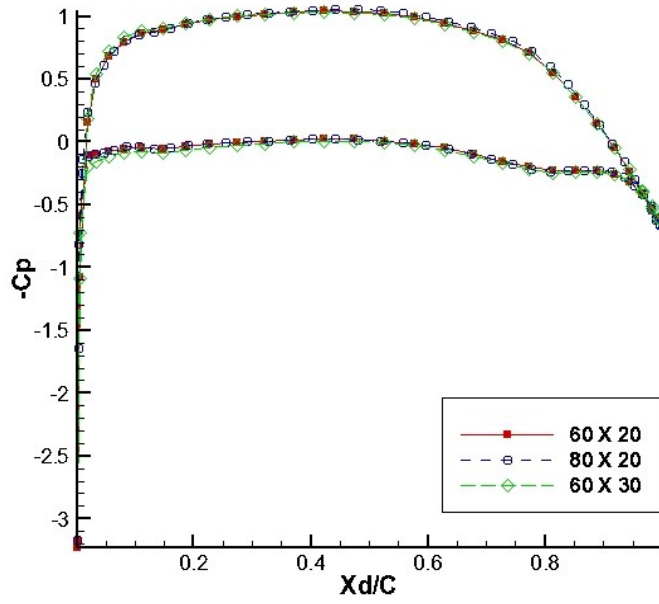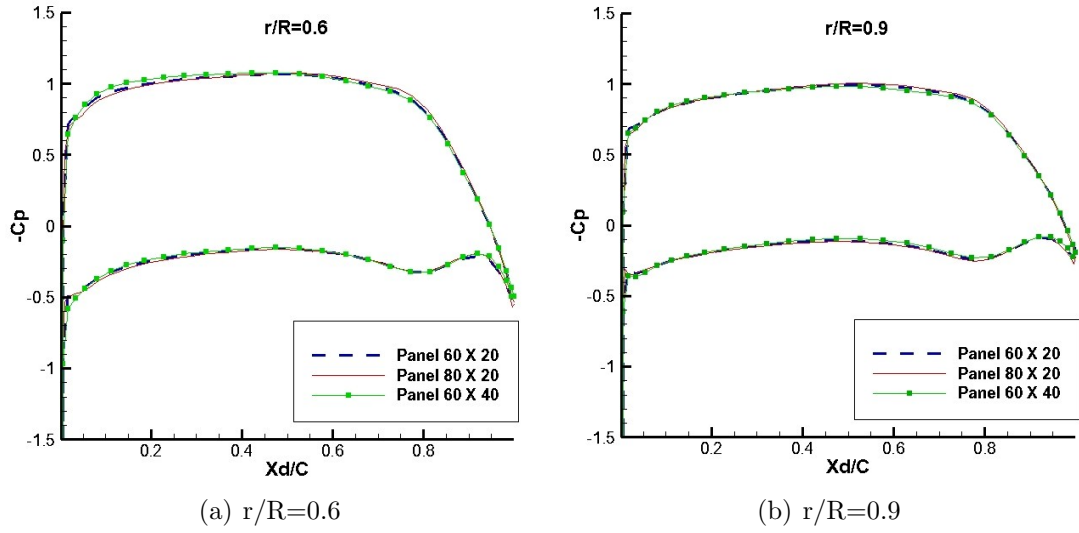
Figure 3.25: Pressure distributions predicted by the present method using different numbers of panels at strips, $r/R = 0.6$ and $r/R = 0.9$, of Propeller NSRDC4381, $J_s = 0.889$, $R_e = \frac{U_\infty D}{v} = 7.42e5$, 1% turbulence level, fixed transition points at 0.1 chord length on both the pressure and suction sides of each strip.

Table 3.1: Information of the RANS (ANSYS/FLUENT) case for Propeller NSRDC4381

Cell number	$1,476,540$
Reynolds number (J=0.889)	$6.22e5$
Reynolds number (J=0.5)	$4.15e5$
Turbulence model	k-ω SST
Pressure correction scheme	SIMPLEC
Spatial discretization	QUICK
Total time for calculate (32 CPUs)	4,386 seconds

condition $J_s = 0.889$. The comparison exhibits an acceptable agreement, indicating that the present method could predict the friction on the propeller blades. The plots of K_T and K_Q of this propeller at different operating conditions are shown in Fig. 3.32. Compared with the experimental measurements,

(a) r/R=0.6

(b) r/R=0.9
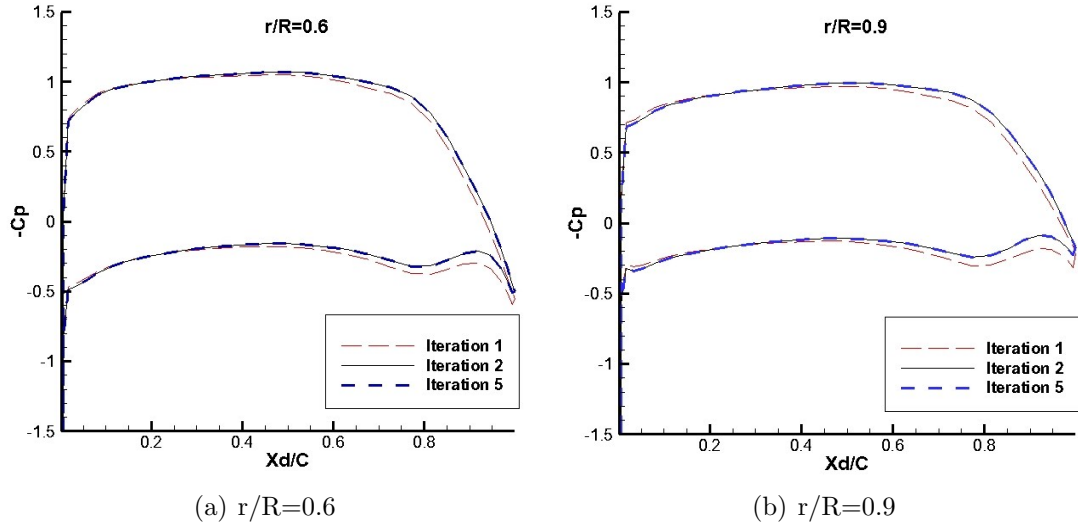
Figure 3.26: Pressure distributions at different iterations at strips $r/R = 0.6$ and $r/R = 0.9$ of Propeller NSRDC4381, predicted by the present method, $J_s = 0.889$, $R_e = \frac{U_\infty D}{v} = 7.42e5$, 1% turbulence level, fixed transition points at 0.1 chord length on both the pressure and suction sides of each strip.

(a) Full view

(b) Detailed view close to trailing edge
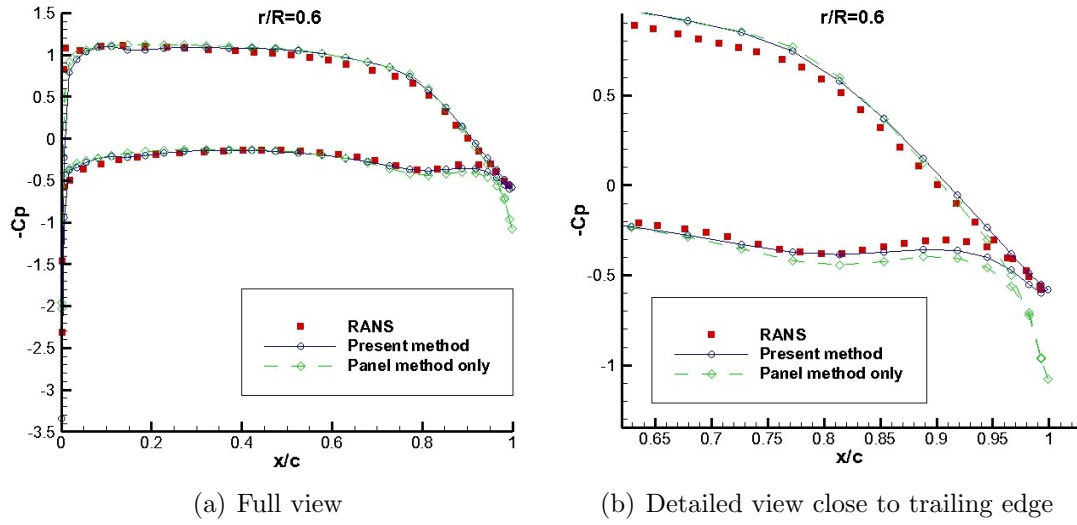
Figure 3.27: Comparison of pressure distributions along the strip, $r/R = 0.6$, of Propeller NSRDC4381, predicted by RANS (ANSYS/FLUENT), panel method and the present method (fixed transition points at 0.1 chord length on both the pressure and suction sides of each strip, 1% turbulence level), $J_s = 0.889$, $R_e = \frac{U_\infty D}{v} = 7.42e5$ for viscous cases.

55

(a) Full view

(b) Detailed view close to trailing edge
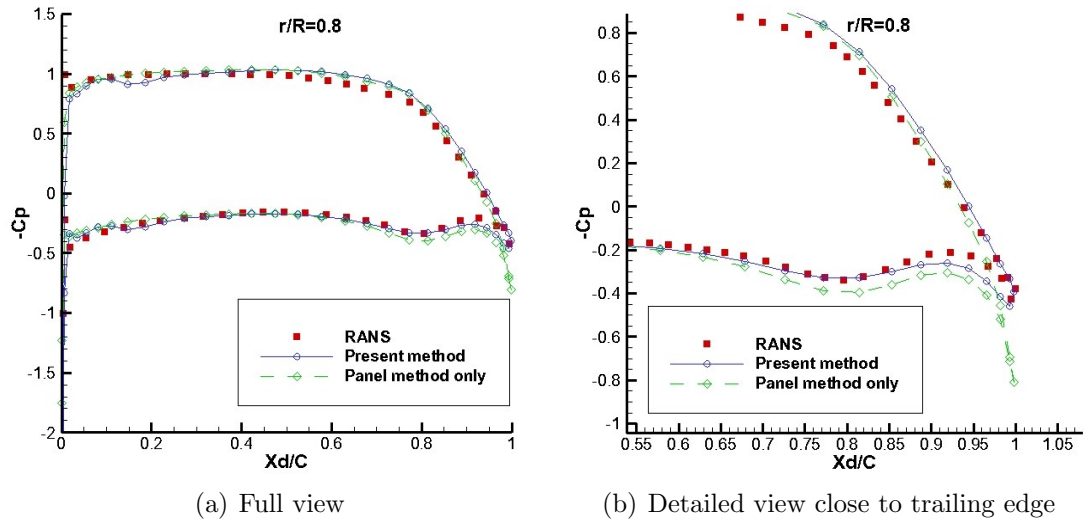
Figure 3.28: Comparison of pressure distributions along the strip, $r/R = 0.8$, of Propeller NSRDC4381, predicted by RANS (ANSYS/FLUENT), panel method and the present method (fixed transition points at 0.1 chord length on both the pressure and suction sides of each strip, 1% turbulence level), $J_s = 0.889$, $R_e = \frac{U_\infty D}{v} = 7.42e5$ for viscous cases.

(a) Full view

(b) Detailed view close to trailing edge
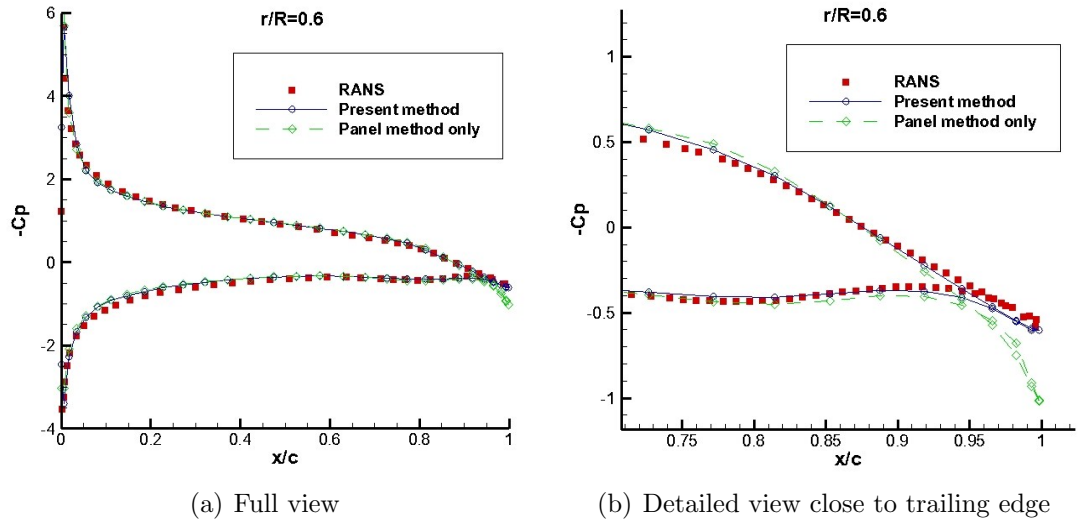
Figure 3.29: Comparison of pressure distributions along the strip, $r/R = 0.6$, of Propeller NSRDC4381, predicted by RANS (ANSYS/FLUENT), panel method and the present method (fixed transition points at 0.1 chord length on both the pressure and suction sides of each strip, 1% turbulence level), $J_s = 0.5$, $R_e = \frac{U_\infty D}{\upsilon} = 4.15e5$ for viscous cases.

(a) Full view

(b) Detailed view close to trailing edge
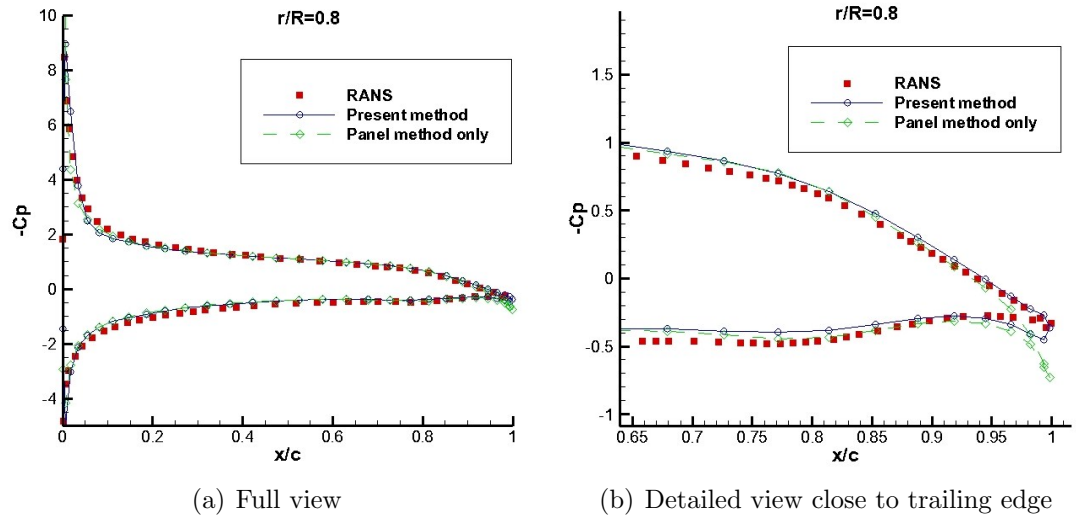
Figure 3.30: Comparison of pressure distributions along the strip, $r/R = 0.8$, of Propeller NSRDC4381, predicted by RANS (ANSYS/FLUENT), panel method and the present method (fixed transition points at 0.1 chord length on both the pressure and suction sides of each strip, 1% turbulence level), $J_s = 0.5$, $R_e = \frac{U_\infty D}{v} = 4.15e5$ for viscous cases.

the results predicted by the present method behave well near the design condition, but under-estimate the K_T and K_Q at low J_s (blow $J_s = 0.5$). In fact, at low J conditions, the effects of the wake become more significant. Thus more accurate wake alignment schemes are needed. The results shown in Fig. 3.32 are obtained by the present method combined with PSF2 wake alignment. Kinnas et al. (2012) developed a new full wake alignment scheme FWA. The results predicted by the present method with the full wake alignment scheme are shown in Fig. 3.33, from which obvious improvements at low J are observed.

(a) r/R=0.6   (b) r/R=0.74
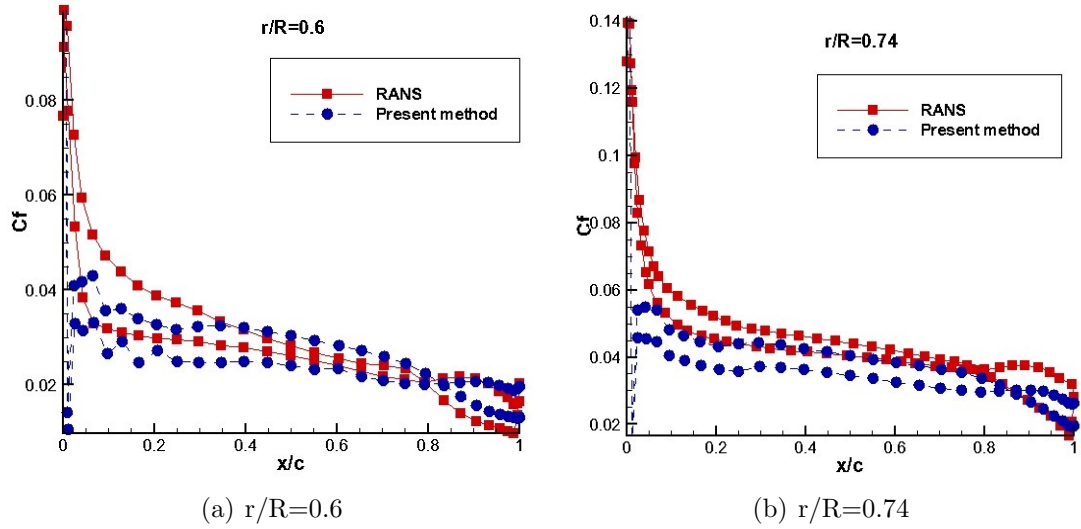
Figure 3.31: Comparison of C_f at strips, $r/R = 0.6$ and $r/R = 0.6$, of Propeller NSRDC4381, between RANS (ANSYS/FLUENT) and the present method (fixed transition points at 0.1 chord length on both the pressure and suction sides of each strip, 1% turbulence level), $J_s = 0.889$, $R_e = \frac{U_\infty D}{v} = 7.42e5$.
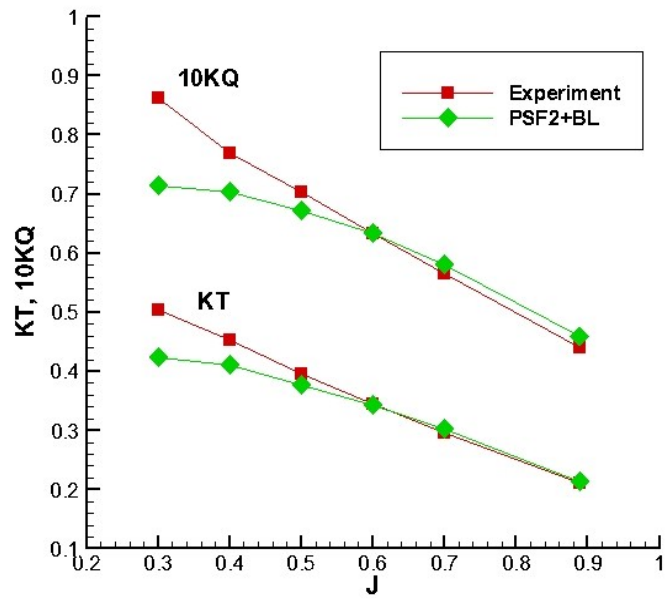
Figure 3.32: Comparisons of K_T and K_Q of Propeller NSRDC4381 at different advance ratios, between the present method combined with PSF2 wake alignment and experiments.
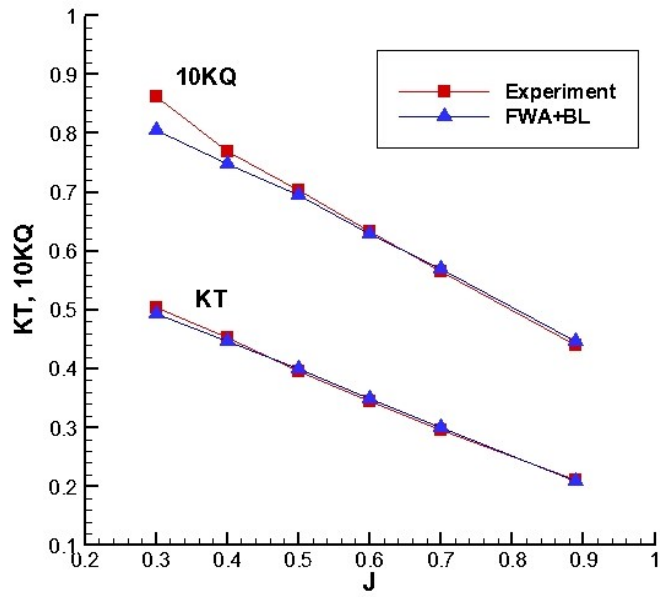
Figure 3.33: Comparisons of K_T and K_Q of Propeller NSRDC4381 at different advance ratios, between the present method combined with full wake alignment and experiments.

3.5   DTMB Duct II

The 3D viscous/inviscid interactive method is applied to a bare duct case. DTMB Duct II is an axis-symmetric duct, which has a NACA66 thickness form, with a maximum thickness-chord ratio $t_{max}/C = 0.1$. The camber has a NACA $a = 0.8$ mean distribution and the maximum camber-chord ratio is $f_{max}/C = 0.04$. Fig. 3.34 shows the paneled geometry of this duct. The duct is placed at zero angle of attack. The Reynolds number $R_e = \frac{U_\infty D}{\nu}$ is 2.06×10^6. The pressure on the duct predicted by the present method is compared with the measurements by Morgan and Caster (1965).
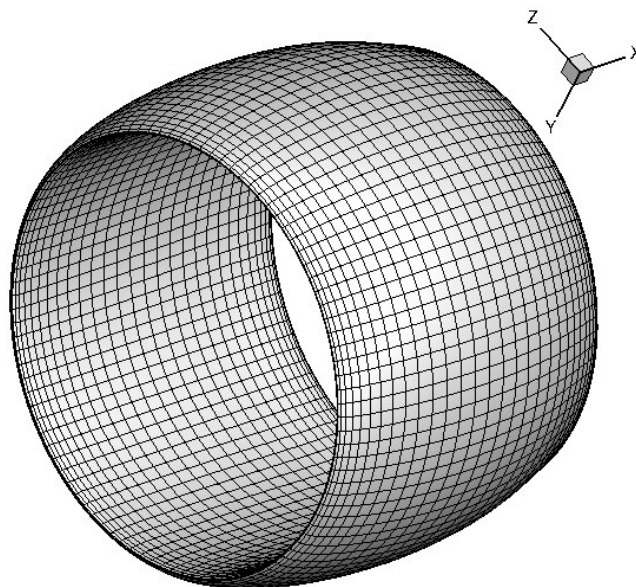
Figure 3.34: Paneled geometry of the DTMB Duct II.

The result (pressure) of a grid dependency study is shown in Fig. 3.35. Using different numbers of panels on the chord and span wise directions, the

plots of the pressures predicted by the current method collapse into the same line. Fig. 3.36 shows the convergence process of the pressure. At the 5th iteration, converged results are obtained. Since DTMB Duct II is an axis-symmetric duct and the angle of attack is zero, it is expected that the pressure or the boundary layer variables be the same at different sections along the chord wise direction. The pressure and the displacement thickness of boundary layer at three selected strips along chord wise direction are checked and shown in Fig. 3.37 and Fig. 3.38, respectively.
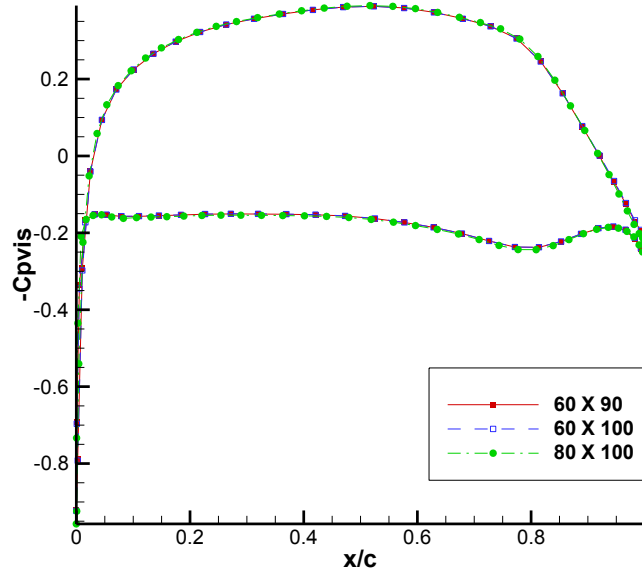
Figure 3.35: Pressure distributions on DTMB Duct II predicted by the present method using different numbers of panels on both the chord and span wise directions, $R_e = \frac{U_\infty D}{v} = 2.06e6$, fixed transition points at 0.05 chord length on both the pressure and suction sides of each strip, 1% turbulence level.

Fig. 3.39 shows the predicted invsicid (panel method only) and viscous
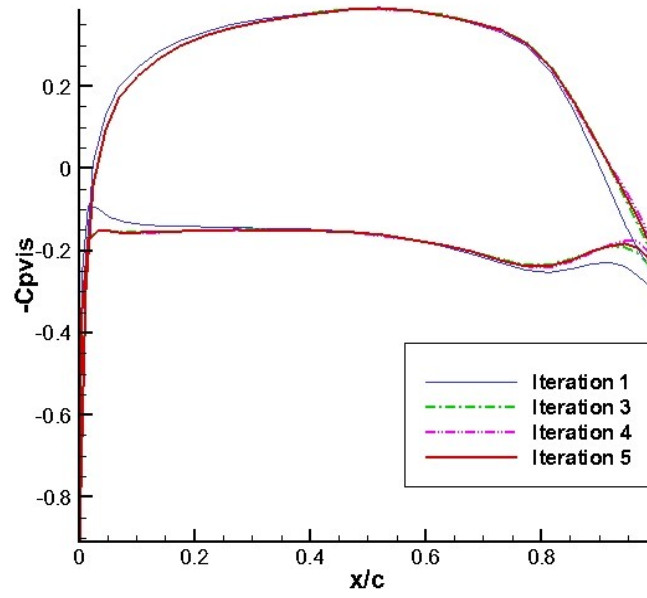
Figure 3.36: Pressure distributions at different iterations on DTMB Duct II, predicted by the present method, $R_e = \frac{U_\infty D}{v} = 2.06e6$, fixed transition points at 0.05 chord length on both the pressure and suction sides of each strip, 1% turbulence level.
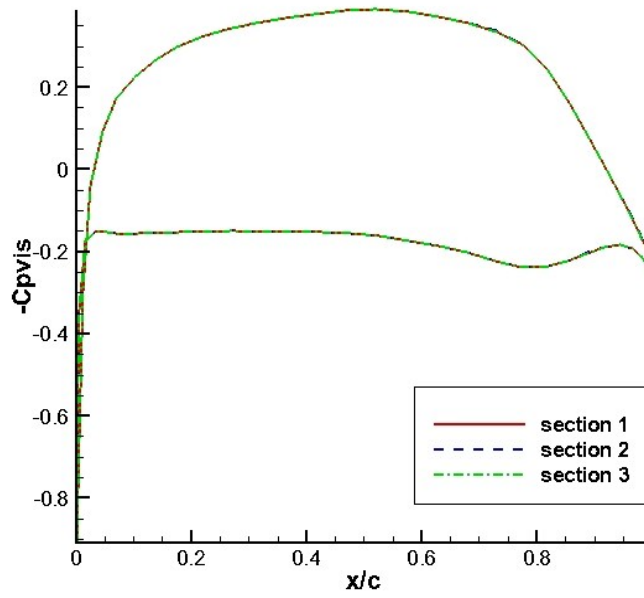
Figure 3.37: Pressure distributions along three different sections of DTMB Duct II, predicted by the present method, $R_e = \frac{U_\infty D}{v} = 2.06e6$, fixed transition points at 0.05 chord length on both the pressure and suction sides of each strip, 1% turbulence level.
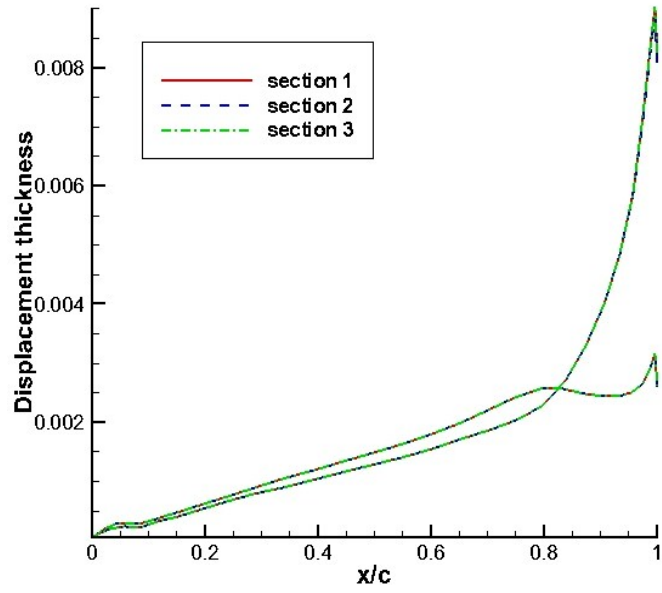
Figure 3.38: Displacement thickness of boundary layer along three different sections of DTMB Duct II, predicted by the present method, $R_e = \frac{U_\infty D}{v} = 2.06e6$, fixed transition points at 0.05 chord length on both the pressure and suction sides of each strip, 1% turbulence level.

(present method) pressure on the duct strip compared with the experimental measurements from Morgan and Caster (1965). Both the viscous and inviscid solution show good correlations with the experiment data.
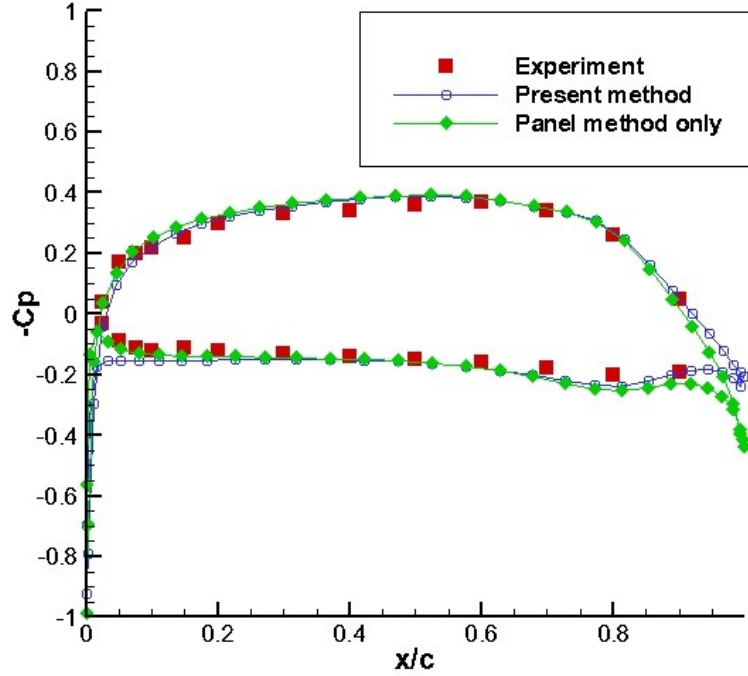
Figure 3.39: Viscous and inviscid pressure distributions on the DTMB Duct II predicted by the present method (fixed transition points at 0.05 chord length on both the pressure and suction sides of each strip, 1% turbulence level), compared with the experimental measurements by Morgan and Caster (1965), $R_e = \frac{U_\infty D}{v} = 2.06e6$.

Chapter 4

Viscous Image Model

In this chapter, the image model used to simulate the effects of slip walls developed by Singh (2009) is introduced. The author further improves this model for viscous cases. A case of a straight wing blade between two slip walls is carried out, and the results are compared with those of a RANS case. Next, the results of a case of a swept wing blade between two slip ways are presented and analyzed. The slip walls exclude the effects of the blade tip, so that the 3D viscous/inviscid interactive is more easy to be applied. In addtion, the case of the straight wing between two parallel slip walls is expected equivalent with a 2D case, which is a good test to validate the 3D viscous/inviscid interactive method.

4.1 Image Model with Panel Method Only

Singh (2009) introduced an image model to simulate the effects of slip walls. For instance, the system of a wing blade adjacent to a slip wall shown in Fig. 4.1 is equivalent to the one shown in Fig. 4.2. In Fig. 4.2, the effects of the slip wall are considered by mirroring the wing blade about the wall, so that the derivative of any variable cross the red line is zero as the effects of

the slip wall in Fig. 4.1.
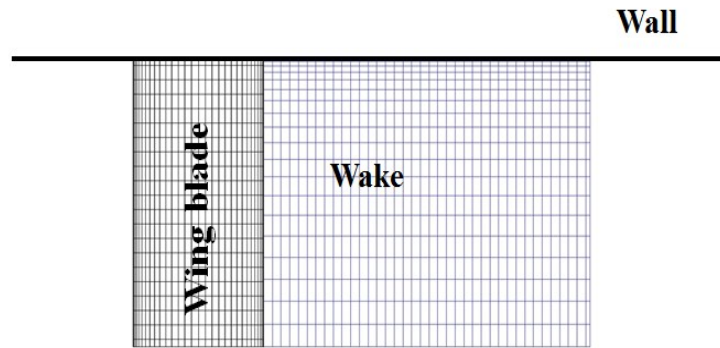
Figure 4.1: Diagram of a straight wing blade adjacent to a slip wall
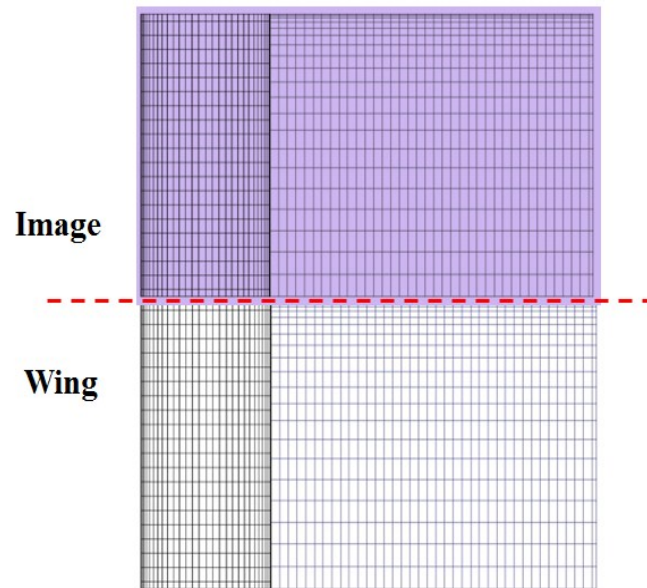
Figure 4.2: Diagram of a straight wing blade and its images, symmetric about the red line

Since the wing blade and its image shown in Fig. 4.2 are symmetric about the wall, the potential on a panel of the wing blade should be the same

with that on the corresponding image panel symmetric about the wall. With this statement, the inviscid solution of this case can be obtained by solving (2.12), but with new influence coefficients to consider the effects of the image. The new influence coefficients are expressed as:

$$A_{ij}^{new} = A_{ij} + A_{ij'} \tag{4.1}$$

$$S_{ij}^{new} = S_{ij} + S_{ij'} \tag{4.2}$$

where j' is the image panel corresponding to the original panel j on the wing blade. One useful fact is that the source or dipole influence coefficient due to an image panel at a particular control point is the same as the one due to the original panel at the image control point (shown in Fig. 4.3). According to this fact, the influence coefficients can be rewritten as:

$$A_{ij}^{new} = A_{ij} + A_{i'j} \tag{4.3}$$

$$S_{ij}^{new} = S_{ij} + S_{i'j} \tag{4.4}$$

The new expressions are very useful for the simplification of coding. When multiple images are considered, the influence coefficients become:

$$A_{ij}^{new} = A_{ij} + \sum_{i'}^{Image} A_{i'j} \tag{4.5}$$

$$S_{ij}^{new} = S_{ij} + \sum_{i'}^{Image} S_{i'j} \tag{4.6}$$

where $Image$ is the number of images. With the new influence coefficients, the inviscid solution can be obtained by solving (2.12).
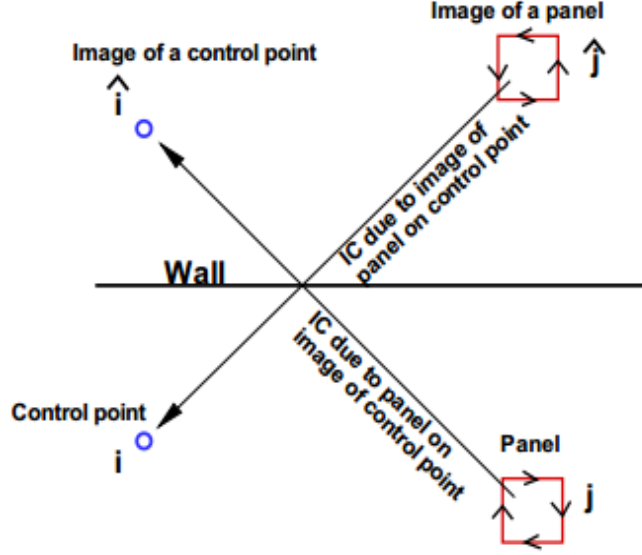
Figure 4.3: Diagram of the equivalence of the influence coefficients, from Singh (2009)

4.2 Image Model with 3D Viscous/Inviscid Interactive Method

Once the inviscid solution is obtained, blowing sources with unknown strengths are added on the panels of the original wing blade, the wake and their images to consider the effects of fluid viscosity. Analogous to (3.1), the viscous velocity becomes:

$$
\begin{aligned}
U_{i,m}^e &= \frac{\partial \Phi_i, m}{\partial s} \\
&= U_{i,m}^{inv} + \sum_{j=1}^{N+N_W} D_{i,j,m} m_{j,m} + \sum_{k=1, k\neq m}^{mr} \sum_{j=1}^{N+N_W} D_{i,j,k} m_{j,k} \\
&\quad + \sum_{im=1}^{Imag} \sum_{k=1}^{mr} \sum_{j=1}^{N+N_W} D_{i,j,k,im} m_{j,k,im}
\end{aligned}
\tag{4.7}
$$

71

where *Image* is the number of images. Using the same iterative scheme described in Fig. 3.11, The unknown mass defects in (4.7) can be resolved. In this case, the last two terms on the right hand side of (4.7) should be updated each iteration and added to the inviscid velocity term.

4.3   Straight Wing between Two Parallel Slip Walls

A case of a 3D straight wing blade between two parallel walls (shown in Fig. 4.4) subject to a uniform inflow with a 2 degree angle of attack is carried out. For this case, infinite images are required on both sides to simulate the effects of the two parallel walls. Practically, a reasonable number of images can be determined through convergence studies to obtained fairly accurate numerical results.
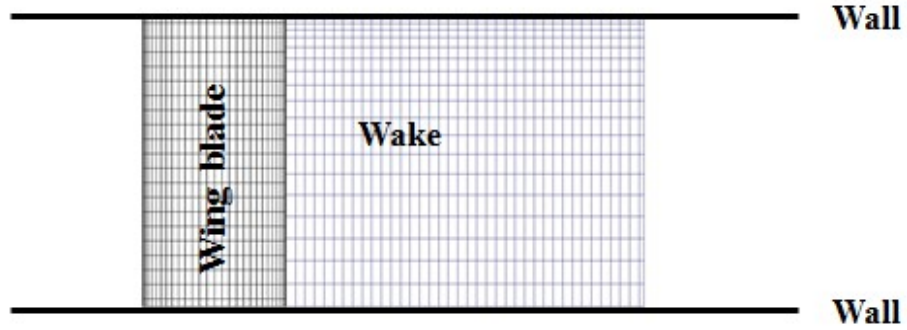
Figure 4.4: Diagram of a wing blade between two parallel walls

The result (pressure) of a grid dependence study is presented in Fig. 4.5. The plots of the pressure coefficients along the strip at $r/R = 0.75$ obtained using different numbers of panels on both span wise and chord wise

directions collapse into the same line. In other words, the changes of the number of panels do not affect the final result, indicating a good convergence character of the present method and the code.
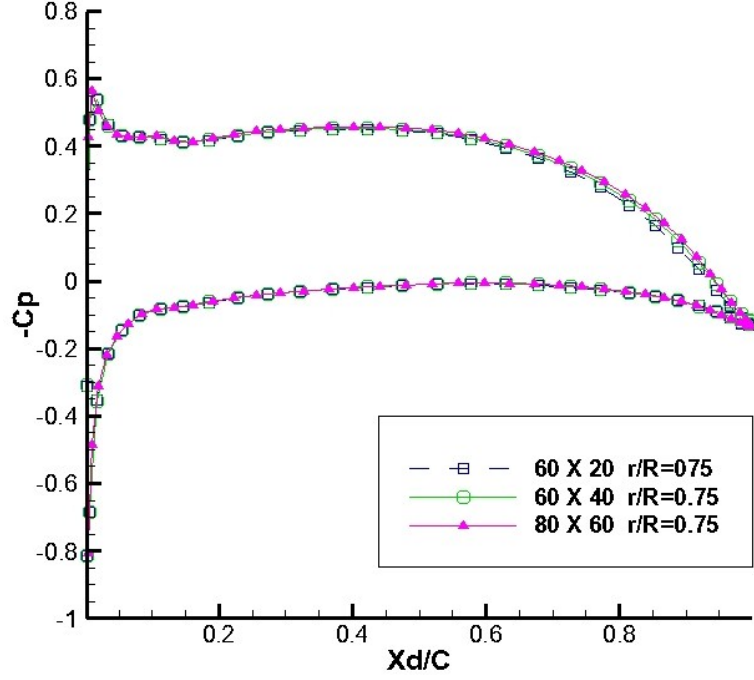
Figure 4.5: Pressure distributions along the strip at $r/R = 0.75$, predicted by the present method using different numbers of panels on span and chord wise directions, $R_e = \frac{U_\infty c}{v} = 1.0e6$, fixed transition points at 0.1 chord length on both the pressure and suction sides of each strip, 1% turbulence level.

A convergence study is conducted to determine a reasonable number of images to simulate the effects of the two parallel slip walls. Different numbers of images on each side are selected, and the predicted circulations are plotted in Fig. 4.6, from which the circulation is converging with the increase of the image number. The viscous and invscid pressure distributions along the strip

73

at $r/R = 0.6$ on the wing blade are plotted in Fig. 4.7. For the convergence of pressure, 10 images each side are sufficient.
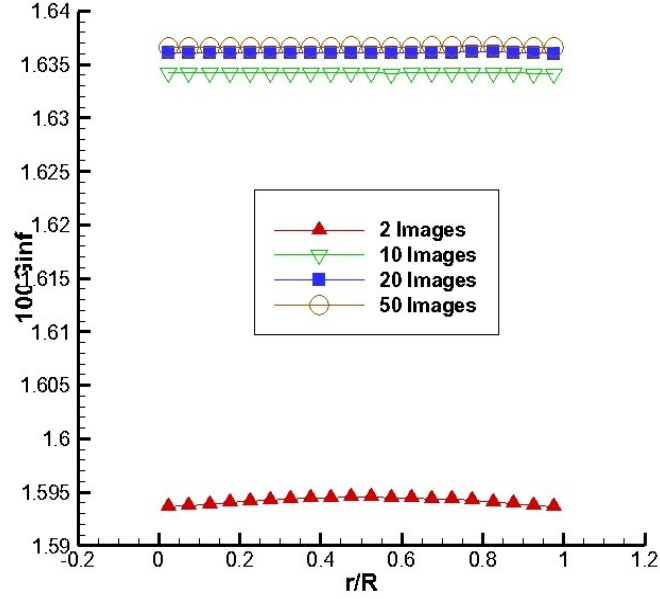
Figure 4.6: Circulations on the straight wing blade predicted by the original image model of Singh (2009) using different numbers of images.

A case of a 3D straight wing between two parallel walls subject to a uniform inflow with a particular angle of attack is expected equivalent to a 2D wing strip subject to the same inflow. In other words, the flow around the 3D wing blade could be reduced to a 2D flow around a 2D strip extracted from the wing blade along the chord wise direction. Thus it is expected that the pressure distributions at different strips of the straight wing blade should be the same. Using 10 images each side, the pressure distributions along three different strips are plotted in Fig. 4.8 for both viscous (a) and invscid (b)

74

(a) Viscous

(b) Inviscid
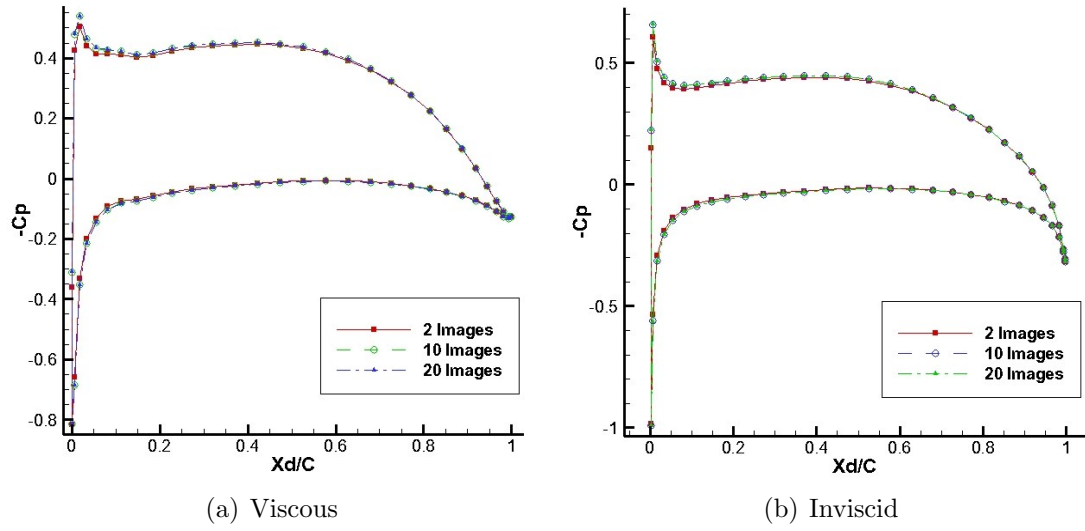
Figure 4.7: Pressure distributions along the strip at $r/R = 0.6$ of the straight wing blase, predicted by the original and the present image model, using different numbers of images. For the viscous case, $R_e = \frac{U_\infty c}{v} = 1.0e6$, fixed transition points at 0.1 chord length on both the pressure and suction sides of each strip, 1% turbulence level.

cases. The plots of the pressure distributions collapse into the same line, as expected.

(a) Viscous   (b) Inviscid
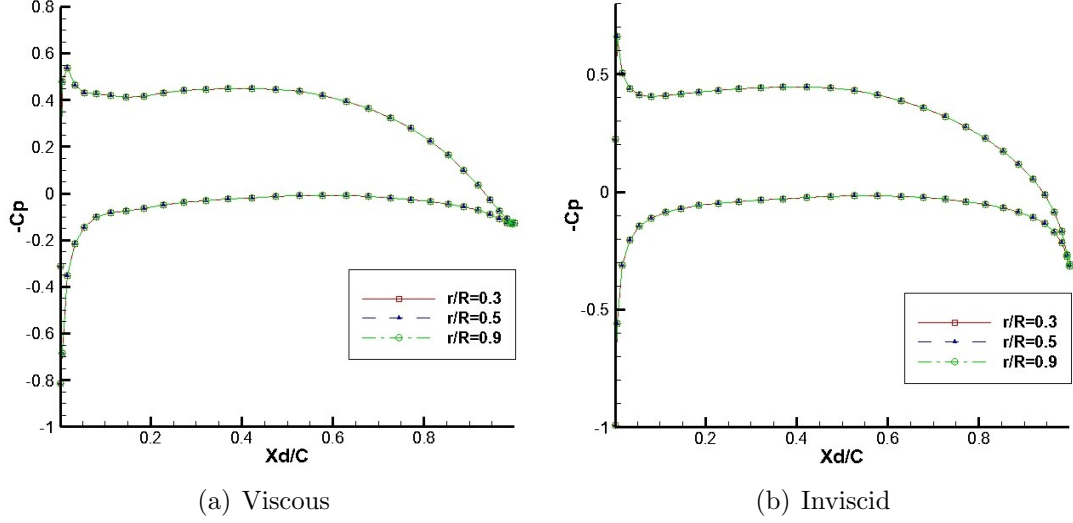
Figure 4.8: Pressure distributions on the strips at $r/R = 0.3$, $r/R = 0.5$ and $r/R = 0.9$ of the straight wing blade, predicted by the original and the present image model, using different numbers of images. For the viscous case, $R_e = \frac{U_\infty c}{v} = 1.0e6$, fixed transition points at 0.1 chord length on both the pressure and suction sides of each strip, 1% turbulence level.

A 2D and a 3D RANS case are carried out as references. The domain for the 3D RANS case is shown in Fig. 4.9. H type grid topology is used around the wing blade as shown in Fig. 4.10. The symmetry boundary condition is applied to the side boundaries ABC and DEF to simulate the parallel slip walls. The outlet ABFD is set as the outflow. The rest boundaries are set as the velocity inflow with the a specified velocity. The value of y^+ on the wing surface is ranged between 30 and 50. Some related information about the 3D RANS case is listed in Table 4.1. A section along the chord wise

direction is extracted from the wing blade. The 2D RANS case for the section uses the similar mesh and schemes of the 3D case. The pressures at different strips of the 3D RANS case are compared with the pressure on the 2D section (shown in Fig. 4.11). The comparison shows great consistency, which proves the previous statement about the equivalence of the 2D and 3D cases. Fig. 4.12 compares the pressure distributions on the wing blade, predicted by the RANS, the present method and the panel method only. Both the present method and the panel method can predict acceptable results, but the pressure predicted by the present method has better correlation with the RANS result, especially at the region close to the blade trailing edge.
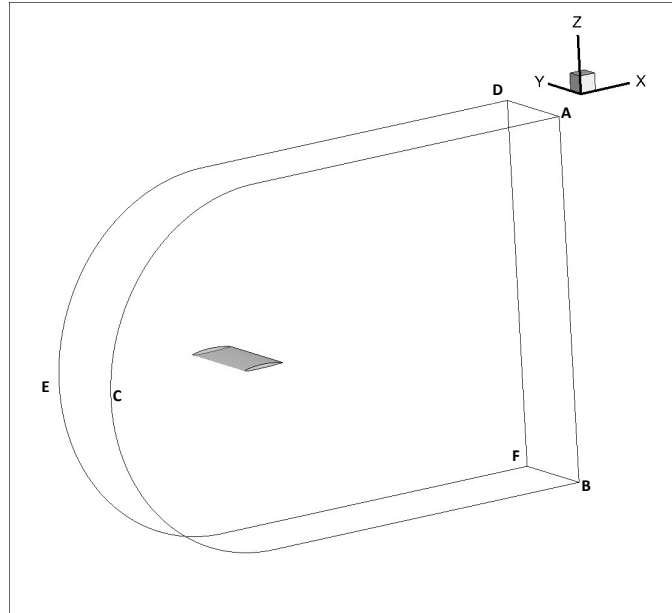
Figure 4.9: Diagram of the domain of the straight wing blade between two parallel slip walls for 3D RANS (ANSYS/FLUENT) simulations.
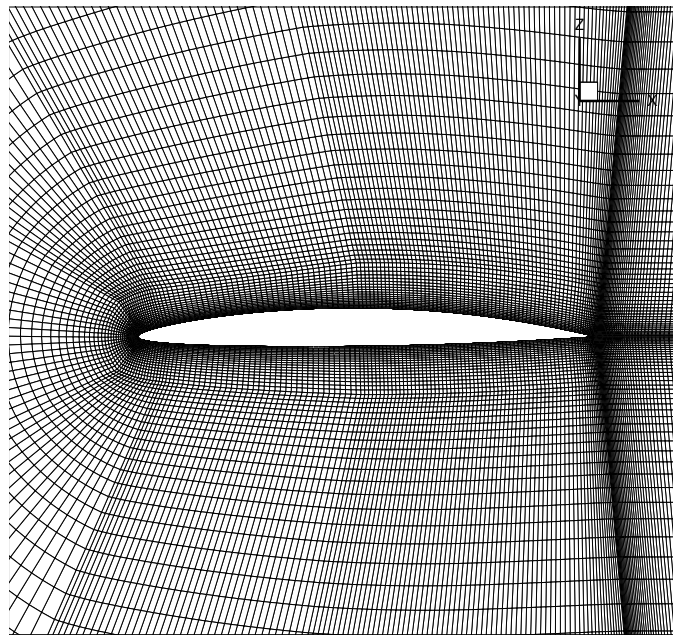
Figure 4.10: Grid details around the straight wing blade used in 3D RANS (ANSYS/FLUENT) simulations.
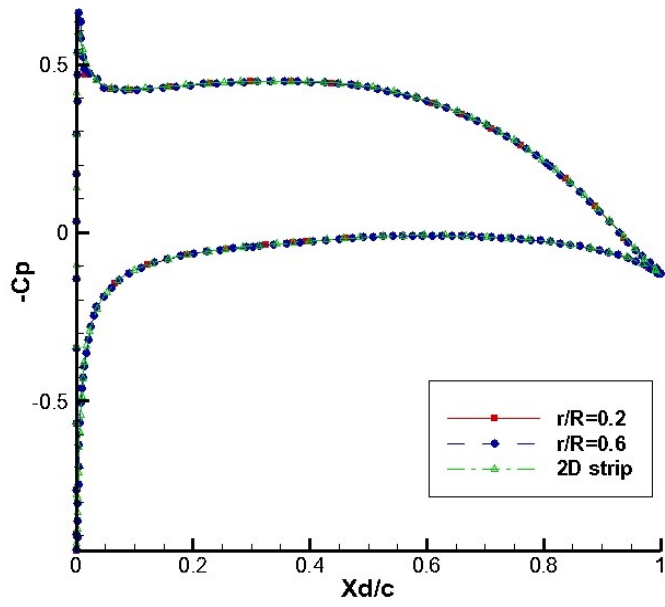
Figure 4.11: Pressure coefficients on the strips at r/R=0.2 and r/R=0.6 of the 3D straight wing predicted by the 3D RANS (ANSYS/FLUENT) case, and on the 2D strip predicted by the 2D RANS (ANSYS/FLUENT) case, $R_e = \frac{U_\infty c}{v} = 1.0e6$.
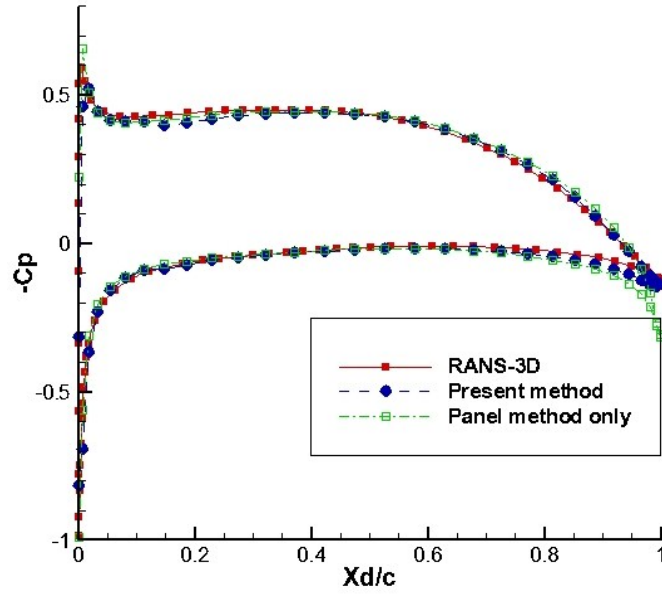
Figure 4.12: Pressure coefficients along the strip at r/R=0.5 of the 3D straight wing predicted by RANS (ANSYS/FLUENT), the present method (fixed transition points at 0.1 chord length on both the pressure and suction sides of each strip, 1% turbulence level) and the panel method. For the viscous case, $R_e = \frac{U_\infty c}{v} = 1.0e6$.

Table 4.1: Information of the RANS (ANSYS/FLUENT) case for a straight wing blade between two parallel slip walls.

Cell number	$537,080$
Reynolds number	$1e6$
Turbulence model	k-ω SST
Pressure correction scheme	SIMPLEC
Spatial discretization	Second order upwind
Total time for calculate (32 CPUs)	20 mins

4.4   Swept Wing between Two Parallel Slip Walls

A case of a 3D swept wing blade between two parallel walls shown in Fig. 4.13 subject to a uniform flow with a 2 degree angle of attack is carried out. The pressures along different strips are plotted in Fig. 4.14. The differences among the plots imply that the case is not equivalent to a simple 2D strip case. The pressures predicted by the present method are also correlated with RANS results in Fig. 4.15, Fig. 4.16 and Fig. 4.17. The comparisons show great agreements.
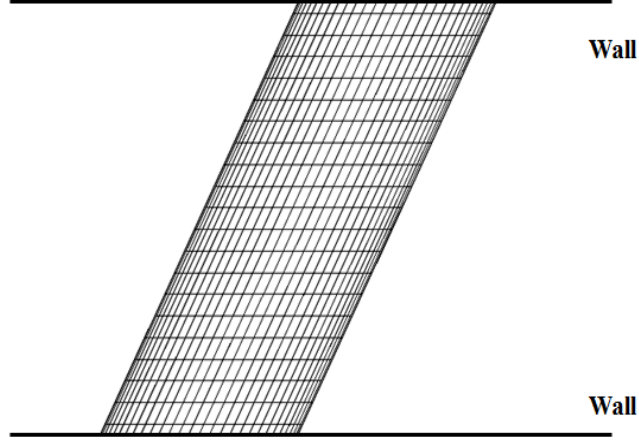
Figure 4.13: Diagram of a swept wing between two parallel slip walls.

(a) Viscous

(b) Inviscid
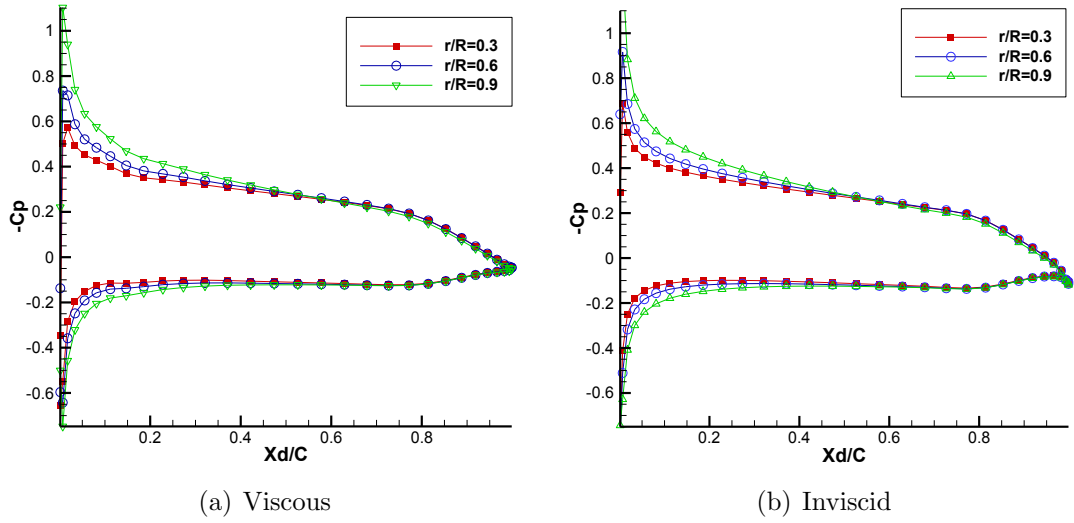
Figure 4.14: Pressure distributions on the strips at $r/R = 0.3$, $r/R = 0.5$ and $r/R = 0.9$ of the wing blade, predicted by the present method, $R_e = \frac{U_\infty c}{v} = 1.0e6$, fixed transition points at 0.1 chord length on both the pressure and suction sides of each strip, 1% turbulence level.
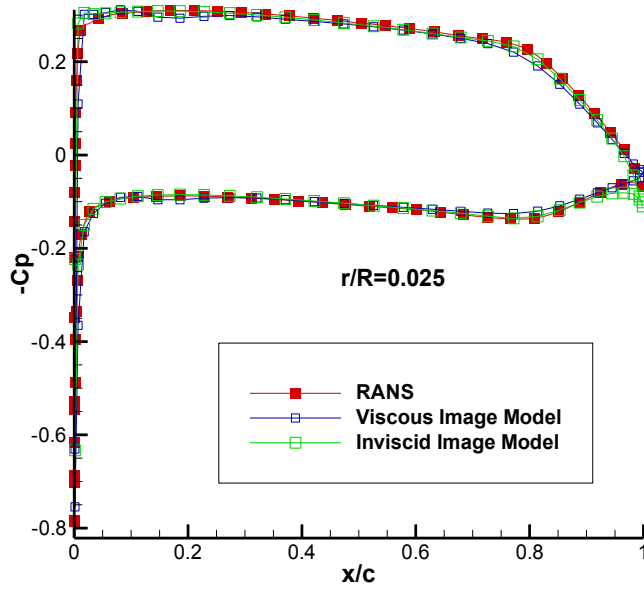
Figure 4.15: Pressure coefficients on the strip at r/R=0.025 of the 3D swept wing, predicted by the 3D RANS (ANSYS/FLUENT) case, the present method (fixed transition points at 0.1 chord length on both the pressure and suction sides of each strip, 1% turbulence level) and the panel method. For the viscous case, $R_e = \frac{U_\infty c}{v} = 1.0e6$.
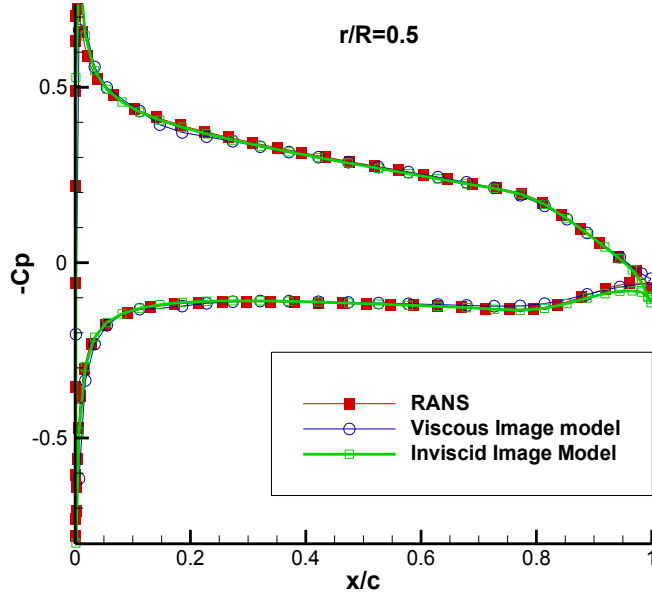
Figure 4.16: Pressure coefficients on the strip at r/R=0.5 of the 3D swept wing, predicted by the 3D RANS (ANSYS/FLUENT) case, the present method (fixed transition points at 0.1 chord length on both the pressure and suction sides of each strip, 1% turbulence level) and the panel method. For the viscous case, $R_e = \frac{U_\infty c}{v} = 1.0e6$.
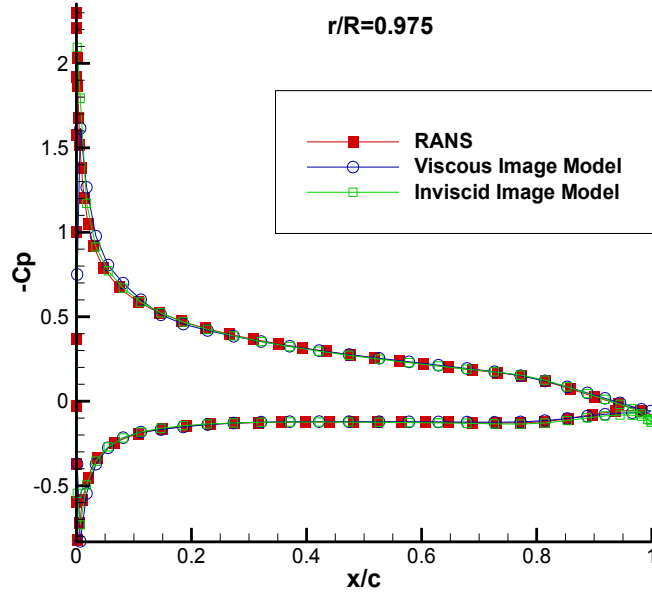
Figure 4.17: Pressure coefficients on the strip at r/R=0.975 of the 3D swep-t wing, predicted by the 3D RANS (ANSYS/FLUENT) case, the present method (fixed transition points at 0.1 chord length on both the pressure and suction sides of each strip, 1% turbulence level) and the panel method. For the viscous case, $R_e = \frac{U_\infty c}{v} = 1.0e6$.

Chapter 5

Hydrofoils and Propellers with Non-Zero Trailing Edge Thickness

In this chapter, the extension scheme for 2D hydrofoils with non-zero thickness trailing edges or open trailing edges proposed by Pan (2009, 2011) is further improved. First, a new extension and search scheme in 2D are introduced in details. Then results of two sample cases are presented and correlated with those of RANS cases. A similar method for 3D blades with non-zero trailing edge thickness is introduced next. The method is applied to a 3D propeller as a sample case and some preliminary inviscid (panel method only) results are presented.

5.1 2D Hydrofoils with Non-Zero Trailing Edge Thickness

5.1.1 Open Trailing Edge Extension Scheme

Panel methods have difficulties dealing with hydrofoils or propeller blades with non-zero thickness trailing edges. In one instance, Fig. 5.1 shows the trailing edge of a strip extracted from the ONR-AxWj-2 rotor blade. Generally, such a trailing edge with finite thickness needs to be closed (shown in Fig. 5.2) for panel methods. However, for the trailing edge with large thick-

ness, this method may change the original geometry too much. Pan (2009, 2011) proposed a scheme that extends the trailing edge with non-zero thickness to form a sharp one (shown in Fig. 5.3).

Finite thickness
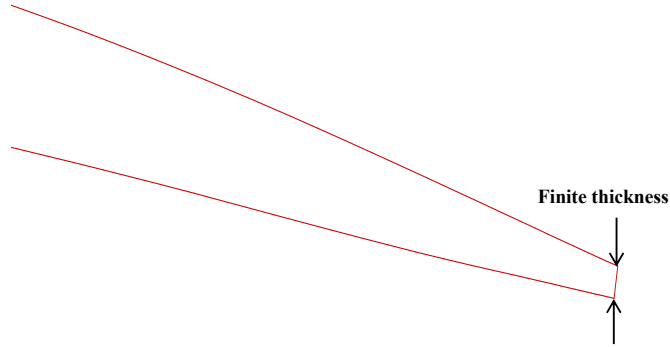
Figure 5.1: Section with a non-zero thickness trailing edge, extracted from the ONR-AxWj-2 rotor blade

Given the last camber point, the method by Pan (2009, 2011) generates a new camber and thickness distributions by interpolation of the original foil and the last camber point. One flaw of this scheme is that the original geometry may be changed once an inappropriate last camber point is given. A new extension scheme that uses second order polynomials to describe the extension edges (as shown in Fig. 5.4) is introduced to overcome the problem of Pan (2009, 2011). Define the two end points of the upper and lower side of the open trailing edge as the cut points as shown in Fig. 5.4. The new scheme estimates the last camber point based on the slopes of the two cut points, so that inappropriate input point can be avoided. Then two second

87
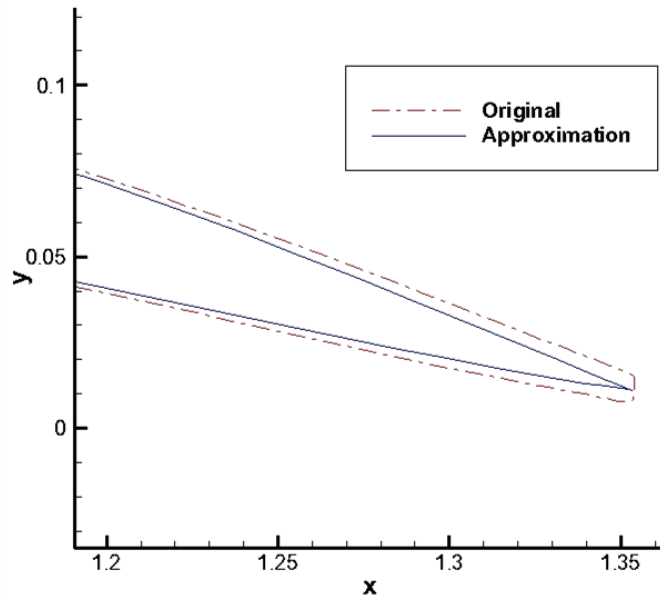
Figure 5.2: Diagram of the modification of the trailing edge with non-zero thickness
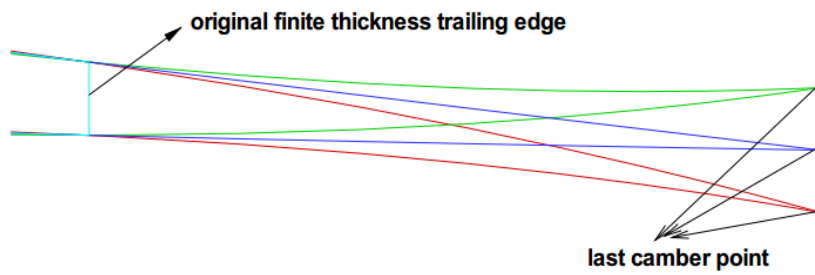
Figure 5.3: Diagram of the extension after the open trailing edge, from Pan (2009)

order polynomials are determined to describe the upper and lower edges of the extension. Suppose the lower side BC of the extension (shown in Fig. 5.4) can be described as:

$$y = ax^2 + bx + c \qquad (5.1)$$

where a, b and c are constant unknowns. The three constants should satisfy the following conditions:

$$y_B = ax_B^2 + bx_B + c$$
$$y_C = ax_C^2 + bx_C + c \qquad (5.2)$$
$$\left(\frac{dy}{dx}\right)_B = 2ax_B + b$$

where the third equation ensures the continuity at point B. The expression of the lower side BC of the extension can be determined by solving (5.2). The upper side can be determined similarly.

5.1.2 Search Scheme for Extension

Since the extension after the open trailing edge is an artificial part, it should satisfy the two following conditions:

- **No-lift condition**

  The lift of the extension part should be zero.

- **Pressure equivalence condition**

  The pressures of the cut points should be same.

In fact, the second condition is the primary one to be satisfied. The first condition is always satisfied with the second one. To satisfy the second condition,

the estimated last camber point is moved vertically to search the correct position. Assume that the pressure difference Δp between the two cut points is a function of the vertical position of the last camber point y_C.

$$\Delta p = f(y_C)$$
$$d(\Delta p) = \frac{df(y_C)}{dy_C} dy_C \tag{5.3}$$

where the derivative $\frac{df(y_C)}{dy_C}$ can be calculated numerically. The search scheme is shown in Fig. 5.5. First, the last camber point based on the slopes of the cut points is estimated. Then extend the trailing edge with the new scheme to form a sharp one and calculate the pressure difference Δp between the cut points. Next, update the vertical position of the last camber point y_C by (5.3) and extend the trailing edge again. Repeat this process until Δp becomes zero.
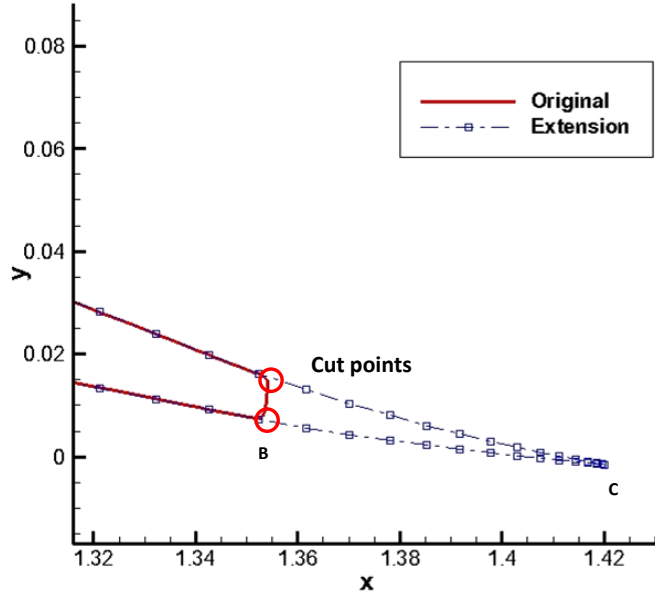
Figure 5.4: Diagram of extension of the trailing edge with non-zero thickness
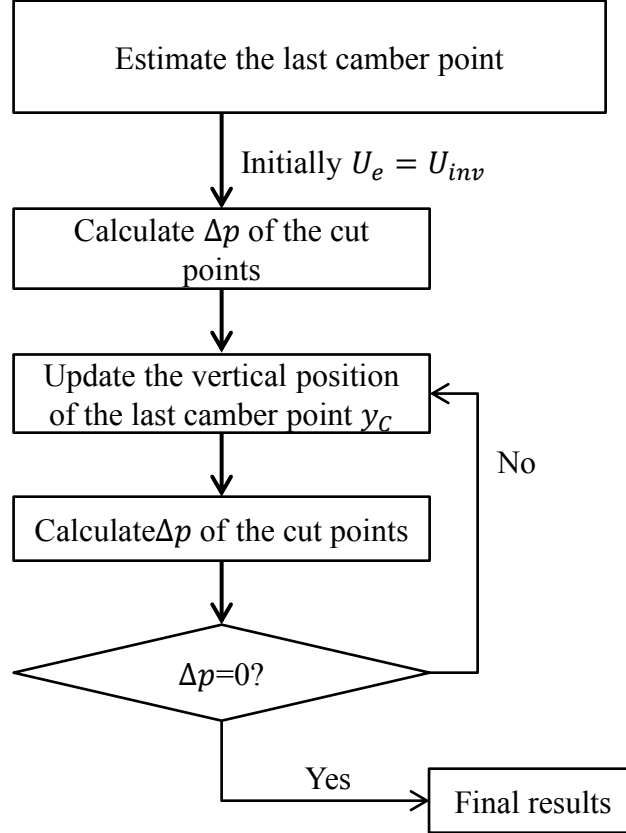
Figure 5.5: Diagram of the procedure of the search scheme for extension

5.2 Sample Cases of 2D Hydrofoils

5.2.1 Strip of ONR-AxWj-2 Rotor Blade

The method described above is applied to a 2D strip extracted from the ONR-AxWj-2 rotor blade at $r/R = 0.7$. The pressure predicted by the

present method has a great correlation with RANS results, shown in Fig. 5.6.

The final pressure difference of the two cut points Δp is $1.95e - 3$, and the

lift on the extension part is less than 0.3 percent of the total lift on the strip,

which satisfies both the zero lift and the pressure equivalence conditions. The

final extension of the trailing edge is shown in Fig. 5.7. The recorded pressure

difference Δp of the two cut points and the vertical position of the last camber

point y_C shows a linear relationship in Fig. 5.8.
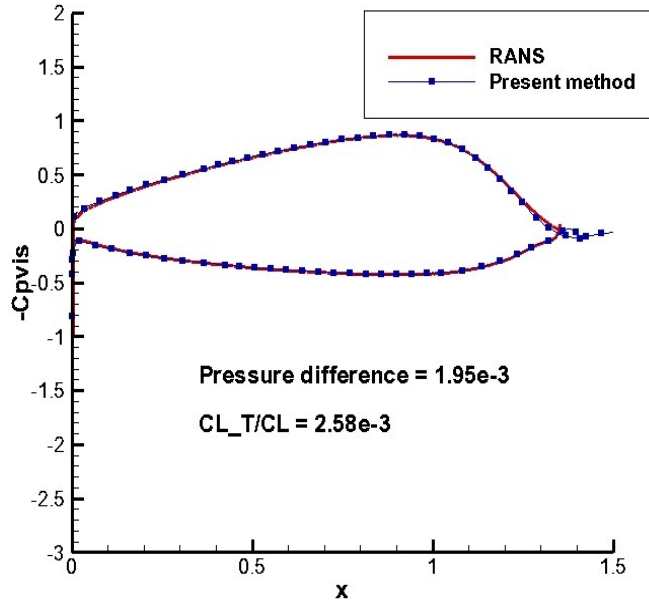
Figure 5.6: Comparison of pressure distributions on the strip extracted from the ONR-AxWJ-2 rotor blade at $r/R = 0.7$, between RANS (AN-SYS/FLUENT) and the present method (fixed transition points at 0.01 chord length on both the pressure and suction sides, 1% turbulence level), $R_e = \frac{U_\infty c}{v} = 5.0e6$.
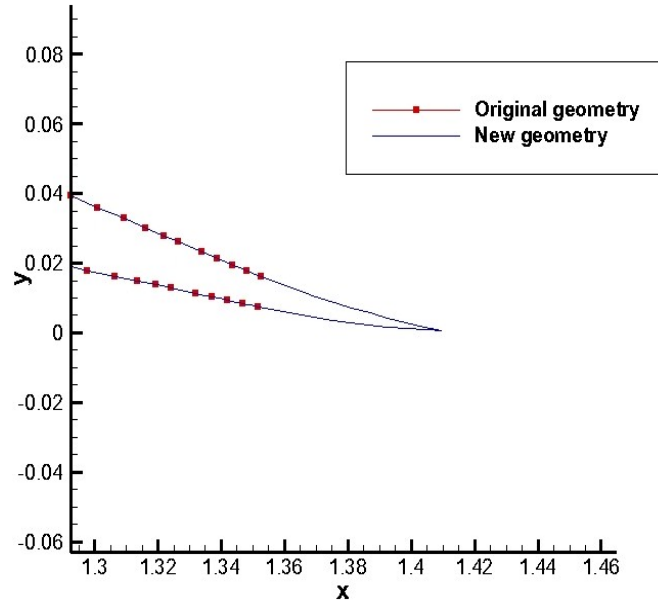
Figure 5.7: Final extension behind the the strip extracted from the ONR-AxWJ-2 rotor blade at $r/R = 0.7$, predicted by the present method, $R_e = \frac{U_\infty c}{v} = 5.0e6$, fixed transition points at 0.01 chord length on both the pressure and suction sides, 1% turbulence level.
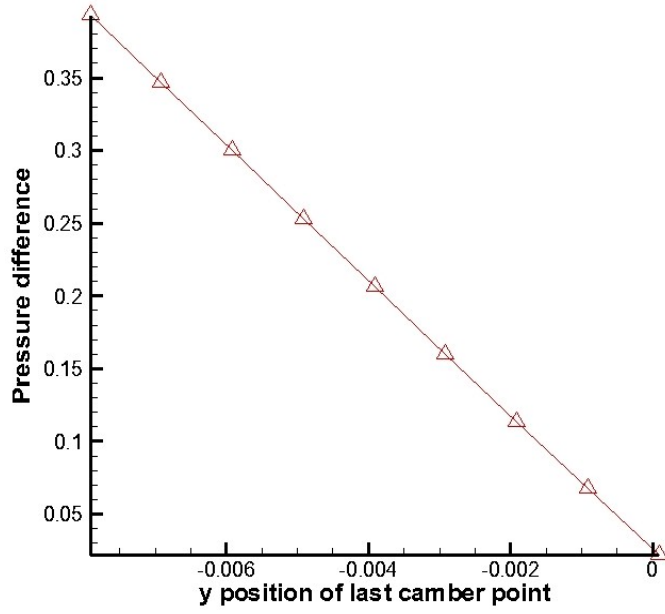
Figure 5.8: Pressure difference Δp of the cut points vs. vertical position of the last camber point y_C, of the ONR-AxWJ-2 rotor blade at $r/R = 0.7$, from the present method, $R_e = \frac{U_\infty c}{v} = 5.0e6$, fixed transition points at 0.01 chord length on both the pressure and suction sides, 1% turbulence level.

5.2.2 NACA Hydrofoil

Another sample case is a 2D NACA hydrofoil ($f_{max}/c = 0.02$, $t_{max}/c = 0.04$) with a vertical cut at the 90 percent chord length treated as a trailing edge with non-zero thickness. The pressure difference Δp of the final result is $3.19e-4$. The lift of the extension part is around 0.5 percent of the total lift. Fig. 5.9 compares the pressure along the section predicted by the present method and RANS. The great agreement of the comparison validates the present method. The final extension behind the open trailing edge is shown in Fig. 5.10, and the linear relationship between Δp and y_C is shown in Fig. 5.11.
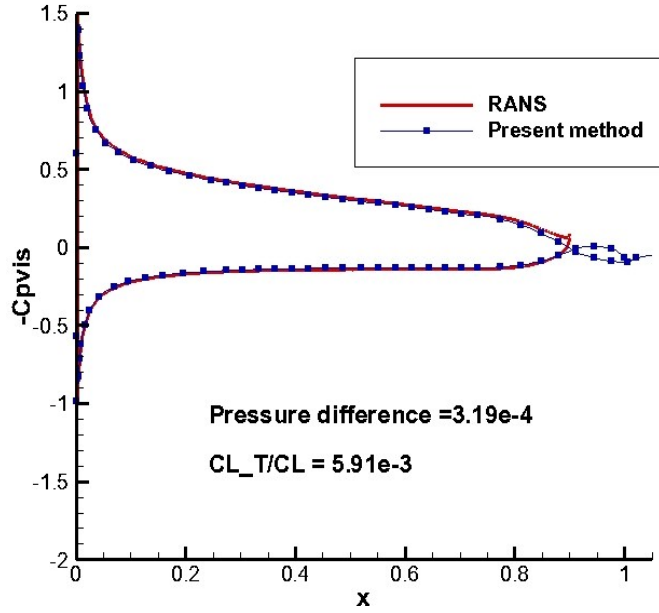
Figure 5.9: Comparison of pressure distributions along the NACA hydrofoil with a non-zero thickness trailing edge, between RANS (ANSYS/FLUENT) and the present method (fixed transition points at 0.01 chord length on both the pressure and suction sides, 1% turbulence level), $R_e = \frac{U_\infty c}{v} = 9.0e6$.
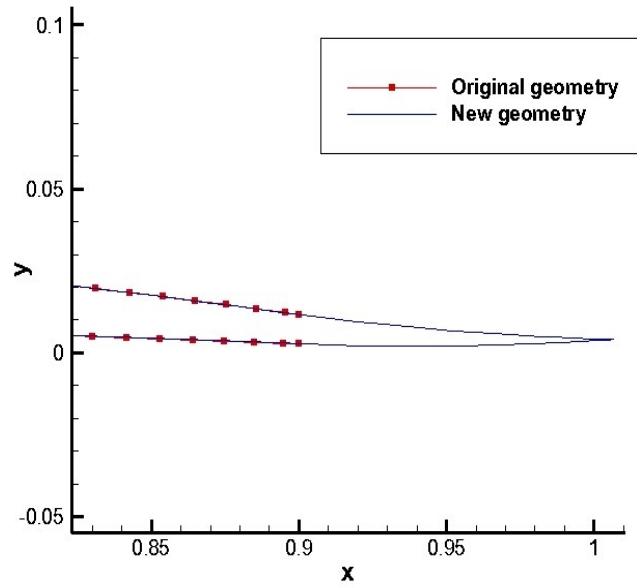
Figure 5.10: Final extension behind the NACA hydrofoil with a non-zero thickness trailing edge, predicted by the present method, $R_e = \frac{U_\infty c}{v} = 5.0e6$, fixed transition points at 0.01 chord length on both the pressure and suction sides, 1% turbulence level.
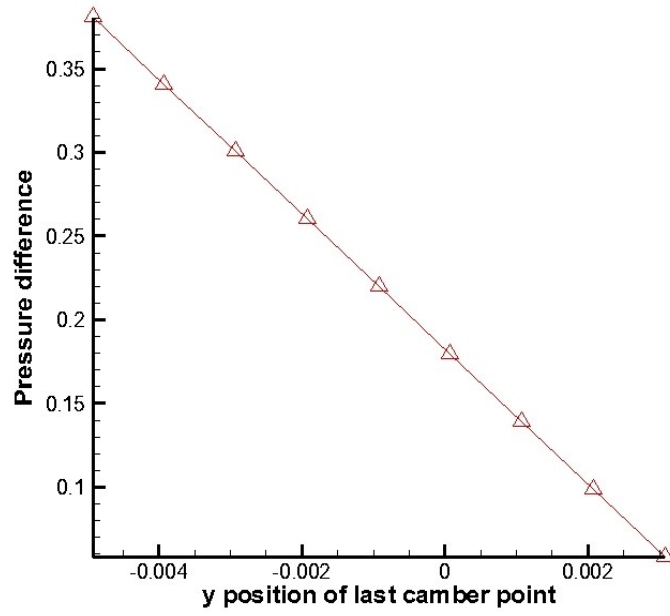
Figure 5.11: Pressure difference Δp of the cut points vs. vertical position of the last camber point y_C, of the NACA hydrofoil with a non-zero thickness trailing edge, from the present method, $R_e = \frac{U_\infty c}{v} = 5.0e6$, fixed transition points at 0.01 chord length on both the pressure and suction sides, 1% turbulence level.

5.3 Propeller Blades with Non-zero Trailing Edge Thickness

For 3D propeller blades with non-zero thickness trailing edges, each blade is divided into several strips along the constant radius. The trailing edge of each strip is extended using the extension scheme used in 2D hydrofoil cases. Next, the Newton's method is used to search the correct positions of the last camber points of the extensions so that the no-lift and the pressure equivalence (primary one) conditions are satisfied. In 3D cases, the pressure difference Δp between the cut points of one section is a function of the vertical positions of the last camber points of all the sections $(y_{c,1}, y_{c,2} \ldots y_{c,mr})$.

$$\Delta p_1 = f_1 (y_{c,1}, y_{c,2} \ldots y_{c,mr})$$

$$\Delta p_2 = f_2 (y_{c,1}, y_{c,2} \ldots y_{c,mr})$$

$$\ldots \tag{5.4}$$

$$\Delta p_{mr} = f_{mr} (y_{c,1}, y_{c,2} \ldots y_{c,mr})$$

where mr is the number of strips on a blade. (5.4) leads to the following relationship:

$$d \begin{bmatrix} \Delta p_1 \\ \Delta p_1 \\ \ldots \\ \Delta p_{mr} \end{bmatrix} = \begin{bmatrix} \frac{\partial f_1}{\partial y_{c,1}} & \frac{\partial f_1}{\partial y_{c,2}} & \cdots & \frac{\partial f_1}{\partial y_{c,mr}} \\ \frac{\partial f_2}{\partial y_{c,1}} & \frac{\partial f_2}{\partial y_{c,2}} & \cdots & \frac{\partial f_2}{\partial y_{c,mr}} \\ \ldots & \ldots & \ldots & \ldots \\ \frac{\partial f_{mr}}{\partial y_{c,1}} & \frac{\partial f_{mr}}{\partial y_{c,2}} & \cdots & \frac{\partial f_{mr}}{\partial y_{c,mr}} \end{bmatrix} d \begin{bmatrix} y_{c,1} \\ y_{c,2} \\ \ldots \\ y_{c,mr} \end{bmatrix} \tag{5.5}$$

The Jacobin matrix in (5.5) could be calculated numerically. The last camber points of the strips are moved vertically a small amount one by one. Each time, the pressure difference between the cut points of each strip is evaluated. The derivatives in the matrix are calculated by dividing the corresponding pressure

differences by the small movement. Once the initial positions of the last camber points of the strips are estimated, the pressure difference Δp between the cut points of each strip could be evaluated. Then the positions of the last camber points of all the strips are updated following (5.5). Repeat the process until the pressure equivalence condition is satisfied on all the strips.

A five-bladed propeller with non-zero thickness trailing edge (studied in Pan 2009) is used in this study. The details of the propeller geometry are restricted to show in this thesis. A global view of this propeller is shown in Fig. 5.12. The extension scheme described in the 2D case is applied to each strip of the propeller blade. The initial modified geometry is shown in Fig. 5.13.
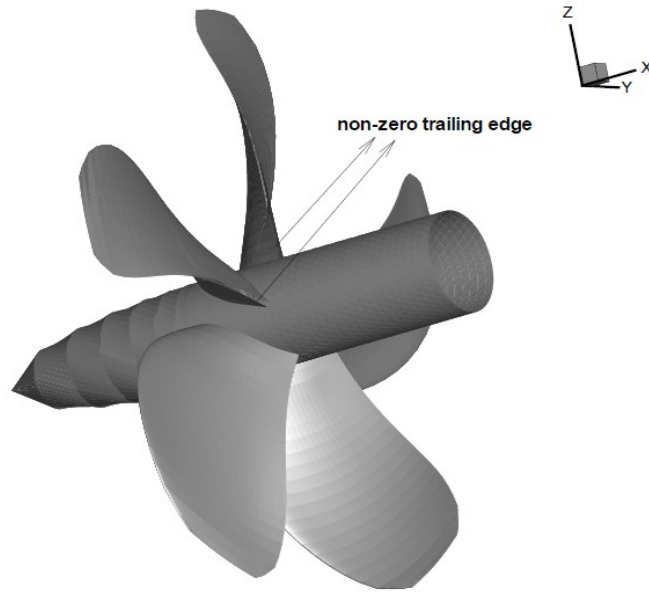
Figure 5.12: Propeller with non-zero trailing edge thickness, from Pan (2009).

The last camber points of the strips are moved a small amount vertically one by one to calculate changes of the pressure difference between the cut points of each strip. Then the derivatives in the Jacobin matrix in (5.5) are calculated numerically. Fig. 5.14 shows the changes of the pressure difference between the cut points on strip1, strip 2 and strip 3 due to the movement of the last camber point on strip 1, at $J_s = 0.75$. Fig. 5.15, Fig. 5.16 and Fig. 5.17 show similar results. All these results indicate that a small movement of the last camber point of one strip could cause a linear change of Δp between the cut points of the strip itself and neighboring strips.

Following (5.5), the positions of the last camber points of all the strips are updated until the pressure equivalence condition is satisfied on all the
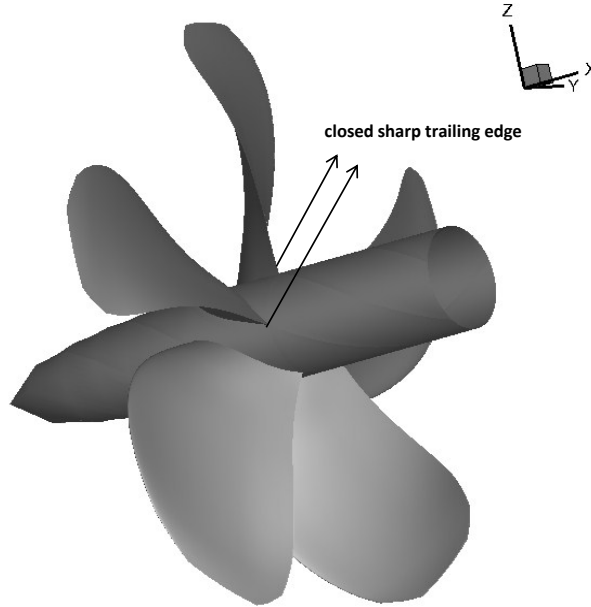
Figure 5.13: Propeller with closed sharp trailing edge modified by the present scheme.
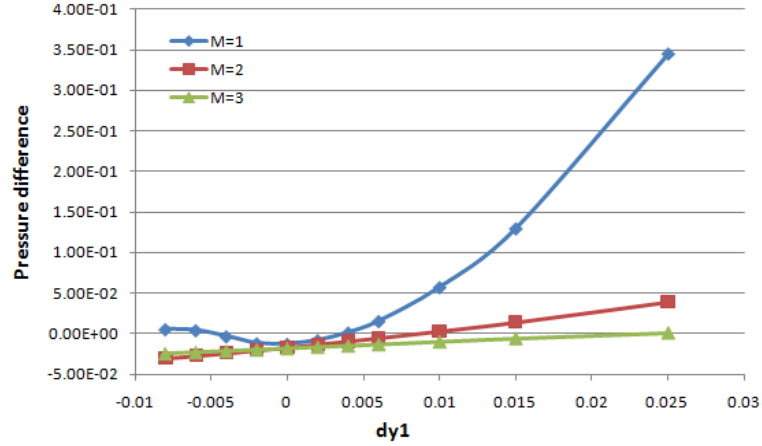
Figure 5.14: Pressure differences between the cut points of strip 1 and neighboring strips vs. the movement of the last camber point of strip 1.
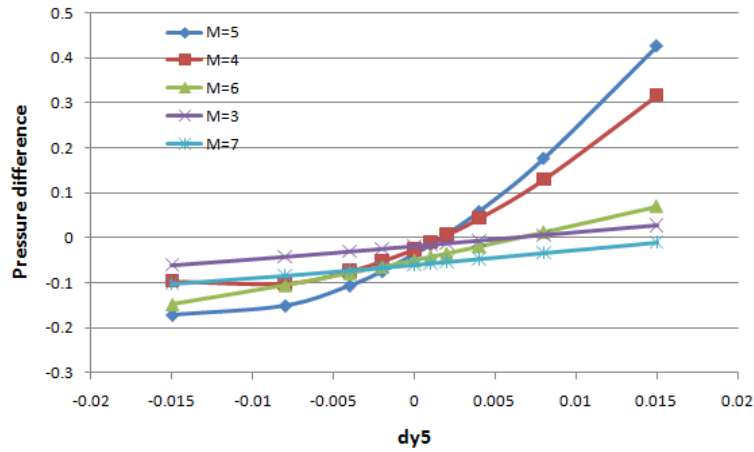
Figure 5.15: Pressure differences between the cut points of strip 5 and neighboring strips vs. the movement of the last camber point of strip 5.
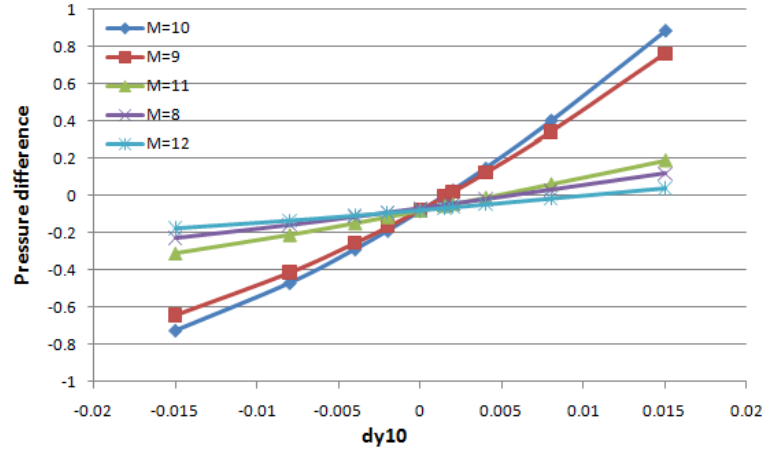
Figure 5.16: Pressure differences between the cut points of strip 10 and neighboring strips vs. the movement of the last camber point of strip 10.
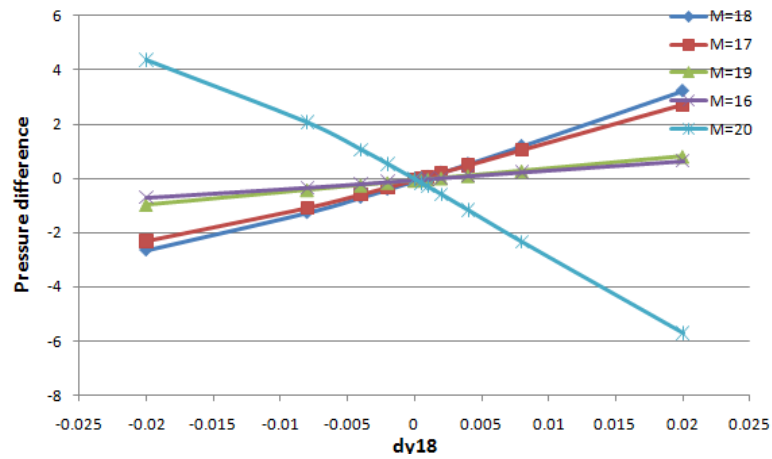
Figure 5.17: Pressure differences between the cut points of strip 18 and neighboring strips vs. the movement of the last camber point of strip 18.

strips. The pressure difference between the cut points of each strips is plotted in Fig. 5.18. The blue line represents Δp on the initial extension. The red line represents the results on the final extension (after several updates of the last camber points). The pressure equivalence condition is satisfied on most strips after four iterations. For the strips very close to the hub and the tip, however, the pressure differences between the cut points do not decrease very obviously, this is because the movements of the last camber points on these strips are restrained to avoid abrupt changed along the trailing edge curve. The circulation on the final blade geometry is plotted in Fig. 5.19. The smooth curve of the circulation indicates the final blade geometry is acceptable and ready for further studies. However, it should be noticed that the success of the 3D search scheme in this case will not necessarily guarantee the success in other cases. Because the derivatives in the Jacobin matrix calculated numerically are only accurate when the movements of the last camber points are restrained in a small amount around the initial positions. In other cases (different Js), the 3D search scheme may lead some large movements of the last camber points. The changes of the pressure differences due to the large movements will be different from the indication of the derivatives in the Jacobin matrix. Therefore, the movement of the last camber point on each strip should be restrained around the initial position, when large movements are calculated by the 3D search scheme. Another reason of restraining the movements of the last camber points is to avoid abrupt changes of the extended trailing edge and ensure that the trailing edge follows a smooth curve.

103
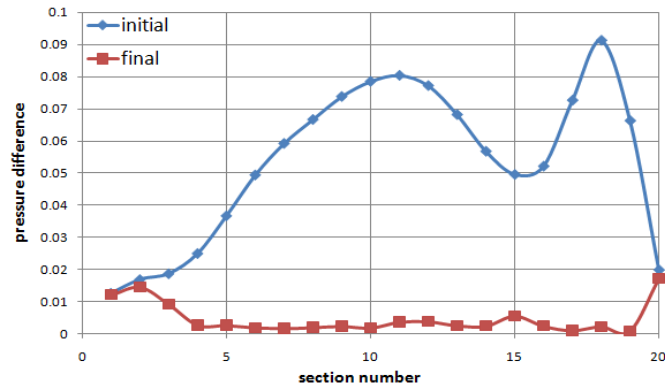
Figure 5.18: Pressure differences between the cut points on the initial and final extensions.
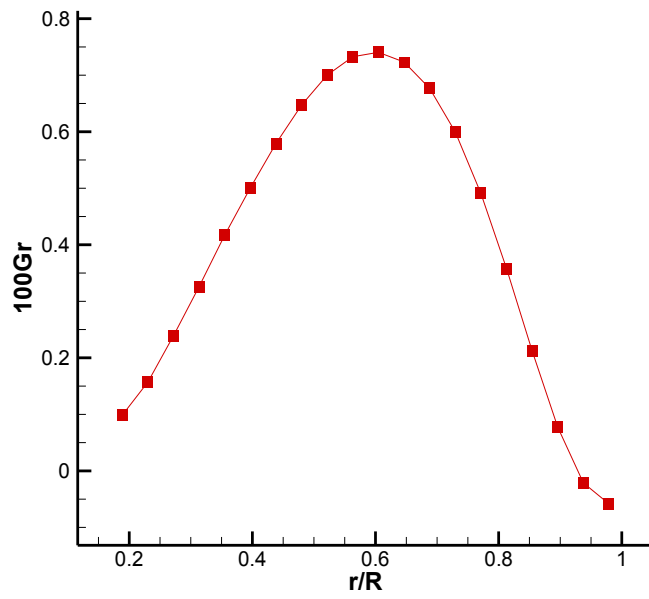
Figure 5.19: Circulation on the final blade geometry.

The thrust/torque forces predicted by the present method, Pan (2009) and experiment are plotted in Fig. 5.20 and Fig. 5.21. The results of the present method show a better correlation with experimental measurements than those in Pan (2009). In fact, the results of Pan (2009) had been improved in Pan and Kinnas (2011) by using a full wake alignment. At this stage, the combination of the improved method and the full wake alignment is not available. Thus the same wake alignment in Pan (2009) is still used to study the effects of the present method. The results by the present method are expected to be improved when further coupled with the full wake alignment used in Pan and Kinnas (2011).
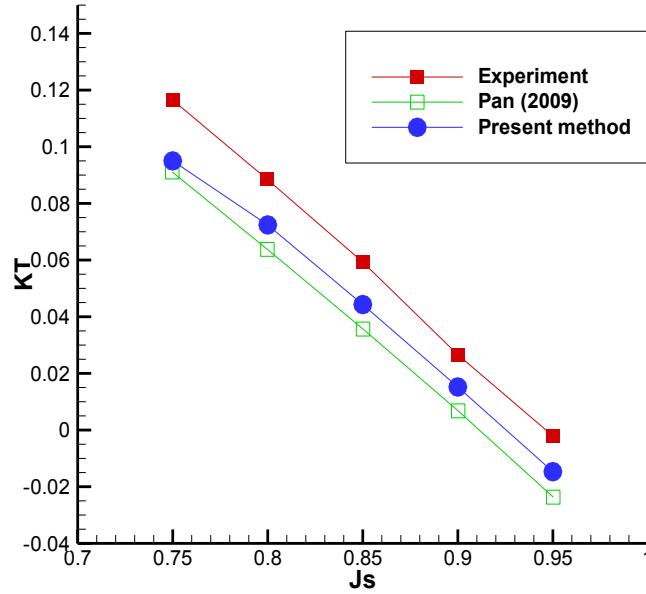
Figure 5.20: K_T of the propeller with finite thickness trailing edge.
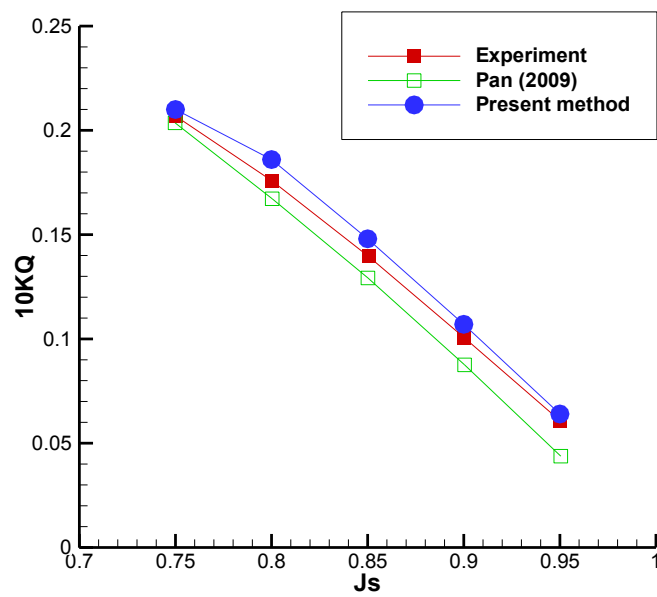
Figure 5.21: K_Q of the propeller with finite thickness trailing edge.

Chapter 6

Conclusions and Recommendations

6.1 Conclusions

In this thesis, a 3D viscous/inviscid interactive method has been developed, by coupling a 3D low-order potential based panel method and a 2D integral boundary layer analysis method, for predicting the effects of fluid viscosity on the performance of fully wetted propellers. The author follows the assumption that the effects of the boundary layer along the span direction (radially outward of propeller blades) are small compared with those along the stream wise direction (along constant radius of propeller blades). The assumption allows one to simplify the 3D boundary layer into 2D on the strips along the stream wise direction and to avoid solving the 3D integral boundary layer equations. This method has been successfully applied to propeller, duct, and hydrofoil cases and shows great correlations with experimental measurements or RANS results. One significant improvement of this method, as compared with previous work, is to further consider the viscous effects of neighboring strips and blades.

Contributions of the present work include:

- The 3D viscous/inviscid interactive method considers the 3D boundary

layer on propeller blades or hydrofoils comprehensively, but with less computation expense by applying a reasonable assumption. Previously, a complete 3D viscous/inviscid interactive method by Milewski (1997) was developed by coupling a panel method with the 3D integral boundary layer equations. Such method requires large amounts of computer resources and is difficult to be applied to complicated geometries such propeller blades. Hufford (1992, 1994) and Sun (2008) assumed that the 3D boundary layer on propeller blades could be reduced into 2D on strips along the constant radius. The author in this thesis follows their assumption but further considers the viscous effects from neighboring strips and blades by a 3D wall transpiration model. The effects of the neighboring blades turns out to be very limited, but the effects of other strips lead to obvious corrections of the pressure distributions on propeller blades.

- The present method can predict the friction on propeller blades more accurately than empirical methods. Generally, such empirical methods use empirical constants as the friction coefficients to take the effects of fluid viscosity into account. The present method provides a better way of predicting the skin friction coefficient. Through some cases in the thesis, it is proven that the predicted friction coefficients by the present method are much more reasonable than any empirical constant.

- The 3D viscous/inviscid interactive method is also applied to develop a viscous image model. Singh (2009) developed an image model to simulate

the effects of slip walls. This model was developed based on a perturbation potential based panel method and was limited only for inviscid cases. A new viscous image model is developed in this thesis by coupling the original model of Singh and the 3D viscous/inviscid interactive method. The new model is applied to cases of wing blades between two parallel slip walls, and the results show better correlation with RANS.

- The method proposed by Pan (2009,2011) for hydrofoils or propeller blases with non-zero thickness trailing edges is improved. Panel methods have some difficulties dealing with such trailing edges. This scheme extends the trailing edge with finite thickness to form a sharp one for panel methods. The geometry of the extension keeps changing until two conditions, the no-lift and the pressure equivalence condition, on the extension part are satisfied. The author in this thesis follows the basic ideal of the method of Pan, but proposes a new extension and an improved search scheme to make this method more reliable.

6.2   Recommendations

The present method produces accurate predictions of the effects of fluid viscosity on propeller flows, but further improvements could be achieved in future research.

- To improve the efficiency of calculations, the present 3D viscous/inviscid interactive method only considers the boundary layer along the stream

wise direction, but ignores the one of crossing flow. Even though this is a reasonable assumption, the boundary layer of the crossing flow may still have some influences on the final results in some cases. In one instance, for the DTMB Duct II case, the results predicted by the present method are changed if the panels on the duct are given a large pitch angle. This is because the panels with the pitch angle make the divided strips away from the steam wise direction. In other words, the boundary layer is not considered in the correct direction. In such situations, the effects of the boundary layer on the other direction cannot be negligible.

- The method proposed by Pan (2009, 2011) for 2D hydrofoils with non-zero thickness trailing edges has been improved and successfully applied to two sample cases in 2D in the thesis. However, the study of 3D cases is very limited. The search scheme for 3D blades should consider the interactions among the strips by Newton's method. The derivatives used in the scheme can only be calculated numerically. Even though the numerical derivatives of the sample case studied in this thesis seems fine, the accuracy still cannot be guaranteed. Pan (2009, 2011) had to sacrifice the efficiency of calculations and deal with the strips one by one. Therefore, more studies and research should be conducted in the future to make the method for 3D cases more reasonable and reliable. In addition, the present method should be further coupled with a full wake alignment to improve the predicted K_T and K_Q.

Appendix

Appendix 1

Evaluation of Influence Coefficients

In this appendix, the formulations of the influence coefficients for 2D and 3D panels are presented.

1.1   2D Influence Coefficients

- Dipole

$$d_{ij} = \frac{1}{2\pi} \int \frac{\partial \ln r}{\partial n} dS \qquad (1.1)$$

- Source

$$s_{ij} = \frac{1}{2\pi} \int \ln r \, dS \qquad (1.2)$$

1.2   3D Influence Coefficients

- Dipole

$$d_{ij} = -\frac{1}{4\pi} \int \frac{\partial (1/r)}{\partial n} dS \qquad (1.3)$$

- Source

$$s_{ij} = -\frac{1}{4\pi} \int \frac{1}{r} r \, dS \qquad (1.4)$$

Bibliography

[1] W. H. Brewer and S .A. Kinnas. CAV2DBL(cavitating 2-dimensional with boundary layer) user's manual(version 1.0). Technical report, Department of Ocean Engineering,MIT, May 1996.

[2] D. Catherall and K. W. Mangler. The integration of the two-dimensional laminar boundary-layer equations past the point of vanishing skin friction. *Journal of Fluid Mechanics*, vol 26:163–182, 1966.

[3] V. Chang, S. Vinayan and S. A. Kinnas. PROPCAV user's manual and documentation (version 3.0). Technical Report 10-1, Department of Civil Engineering, University of Texas at Austin, May 2010.

[4] J. Cousteix. Three dimensional and unsteady boundary layer computations. *Annual Review of Fluid Mechanics*, vol 18:173–196, 1986.

[5] J. Cousteix and R. Houdeville. Singularities in three dimensional and turbulent boundary layer calculations and separation phenomena. *AIAA J.*, vol 19(8):976–985, 1981.

[6] M. Drela. *Two-dimensional Transonic Aerodynamic Design and Analysis Using the Euler Equations.* PhD thesis, Department of Aeronautics and Astronautics, MIT, December 1985.

[7] M. Drela. XFOIL: An analysis and design system for low Reynolds number airfoils. In *Lecture Notes in Engineering (Volume 54, Low Reynolds Number Aerodynamics)*, New York, 1989. Springer-Verlag.

[8] M. Drela and M. B. Giles. Viscous-inviscid analysis of transonic and low reynolds number flows. *AIAA J.*, vol 25:1347–1355, 1987.

[9] G. Hufford. Viscous flow around marine propellers using boundary layer strip theory. Master's thesis, Massachusetts Institute of Technology, 1992.

[10] G. S. Hufford, M. Drela, and J. E. Kerwin. Viscous flow around marine propellers using boundary-layer strip theory. *Journal of Ship Research*, vol 38(1):52–62, March 1994.

[11] S. D. Jessup. *An Experimental Investigation of Viscous aspects of Propeller Blade Flow*. PhD thesis, The Catholic University of America, 1989.

[12] J. E. Kerwin and C. S. Lee. Prediction of Steady and Unsteady Marine Propeller Performance by Numerical Lifting Surface Theory . *Transactions of Society of Naval Architects & Marine Engineers*, 86.

[13] S. A. Kinnas, C. Y. Hsin, and D. P. Keenan. A potential based panel method for the unsteady flow around open and ducted propellers. In *Eighteenth Symposium on Naval Hydrodynamics (1990)*, pages 667–685, Washigton D.C., 1991. National Academy Press.

[14] S. A. Kinnas, H. S. Lee, H. Sun, and L. He. Performance prediction of single and multi-component propulsors using coupled viscous/inviscid methods. In *Tenth International Symposium on Practical Design of Ships and Other Floating Structures (PRADS)*, Houston, Texas, USA, October 2007.

[15] S. A. Kinnas, H. Sun, and H. S. Lee. Numerical analysis of flow around the cavitating cav2003 hydrofoil. In *CAV2003: Fifth International Symposium on Cavitation*, Osaka, Japan, November 1-4 2003.

[16] S. A. Kinnas and Y. Tian. Modeling of leading edge vortex and its effects on propeller performance. In *Second International Symposium on Marine Propulsors (smp11)*, 2011.

[17] X. Kinnas, S. A. Yu and Y. Tian. Prediction of propeller performance under high loading conditions with viscous/inviscid interaction and a new wake alignment model. In *29th Symposium on Naval Hydrodynamics*, August 2012.

[18] C. S. Lee. *Prediction of steady and unsteady performance of marine propellers with and without cavitation by numerical lifting surface theory.* PhD thesis, Department of Ocean Engineering, MIT, May 1979.

[19] Jin-Tae Lee. *A potential based panel method for the analysis of marine propellers in steady flow.* PhD thesis, Department of Ocean Engineering, MIT, July 1987.

[20] W. M. Milewski. *Three-dimensional viscous flow computations using the integral boundary integral equations simultaneously coupled with a low order panel method.* PhD thesis, Department of Ocean Engineering, MIT, 1997.

[21] B. H. Mughal. A calculation method for the three dimensional boundary layer equations in integral form. Master's thesis, Department of Aeronautics and Astronautics, MIT, September 1992.

[22] B. H. Mughal. *Integral Methods for Three Dimensional Boundary Layers.* PhD thesis, Department of Aeronautics and Astronautics, MIT, February 1998.

[23] B. Nishida and M. Drela. Fully simultaneous coupling for three dimensional viscous/inviscid flows. In *AIAA 13th Applied Aerodynamics Conference*, June 1995. 95-1806-CP.

[24] B. A. Nishida. *Fully Simultaneous Coupling of the Full Potential Equation and the Integral Boundary Layer Equations in Three Dimensions.* PhD thesis, Department of Aeronautics and Astronautics, MIT, February 1996.

[25] Y. Pan. A viscous/inviscid interactive approach and its application to wetted or cavitating hydrofoils and propellers with non-zero trailing edge thickness. Master's thesis, The Unversity of Texas at Austin, 2009.

[26] Y. Pan and S. A. Kinnas. A viscous/inviscid interactive approach for the prediction of performance of hydrofoils and propellers with nonzero trailing edge thickness. *Journal of Ship Reasearch*, vol 55(1):45–63, 2011.

[27] H. Schlichting. *Boundary Layer Theory*. McGraw-Hill, Inc., 1979.

[28] A. Sharma. Numerical modeling of a hydrofoil or a marine propeller undergoing unsteady motion via a panel method and rans. Master's thesis, The Unversity of Texas at Austin, 2011.

[29] H. Sun. *Performance Prediction of Cavitating Propulsors Using a Viscous/Inviscid Interaction Method*. PhD thesis, The Unversity of Texas at Austin, 2008.

[30] F. M. White. *Viscous Fluid Flow*. McGraw-Hill, Inc., 1974.

Vita

Xiangming Yu was born in Shenyang, Liaoning Province, China on 22 March 1987, the son of Xiaosheng Yu and Guixia Liu. He received the degree of Bachelor of Science in Engineering from the department of Naval Architecture and Ocean Engineering, Shanghai Jiao Tong University, in July, 2010. In the fall of 2010, he enrolled at the University of Texas at Austin for graduate studies in the Ocean Engineering Group of the Department of Civil, Architectural and Environmental Engineering.

Permanent address: Tiexi District, East Shenliao Road,
Unit 47-3, apt 241
Shenyang City, Liaoning Province 110000
People's Republic of China

This thesis was typeset with LaTeX† by the author.

---

†LaTeX is a document preparation system developed by Leslie Lamport as a special version of Donald Knuth's TeX Program.